CHEMICAL REVIEWS

pubs.acs.org/CR Review

Downloaded via WESTERN UNIV on June 2, 2022 at 17:27:14 (UTC).
See https://pubs.acs.org/sharingguidelines for options on how to legitimately share published articles.

Antiperovskite Electrolytes for Solid-State Batteries

Wei Xia,[⊥] Yang Zhao,[⊥] Feipeng Zhao,[⊥] Keegan Adair, Ruo Zhao, Shuai Li, Ruqiang Zou,* Yusheng Zhao,* and Xueliang Sun*

Cite This: *Chem. Rev.* 2022, 122, 3763−3819

Read Online

ACCESS | Metrics & More | Article Recommendations | Supporting Information

ABSTRACT: Solid-state batteries have fascinated the research community over the past decade, largely due to their improved safety properties and potential for high-energy density. Searching for fast ion conductors with sufficient electrochemical and chemical stabilities is at the heart of solid-state battery research and applications. Recently, significant progress has been made in solid-state electrolyte development. Sulfide-, oxide-, and halide-based electrolytes have been able to achieve high ionic conductivities of more than 10^{-3} S/cm at room temperature, which are comparable to liquid-based electrolytes. However, their stability toward Li metal anodes poses significant challenges for these electrolytes. The existence of non-Li cations that can be reduced by Li metal in these electrolytes hinders the application of Li anode and therefore poses an obstacle toward achieving high-energy density. The finding of antiperovskites as ionic conductors in recent years has demonstrated a new and exciting solution. These materials, mainly constructed from Li (or Na), O, and Cl (or Br), are lightweight and electrochemically stable toward metallic Li and possess promising ionic conductivity. Because of the structural flexibility and tunability, antiperovskite electrolytes are excellent candidates for solid-state battery applications, and researchers are still exploring the relationship between their structure and ion diffusion behavior. Herein, the recent progress of antiperovskites for solid-state batteries is reviewed, and the strategies to tune the ionic conductivity by structural manipulation are summarized. Major challenges and future directions are discussed to facilitate the development of antiperovskite-based solid-state batteries.

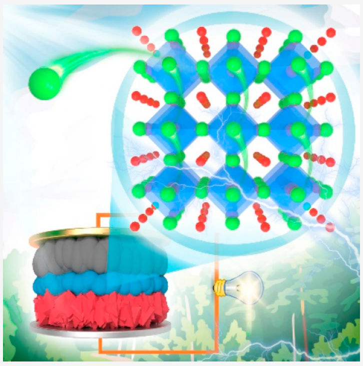

CONTENTS

Received: July 7, 2021
Published: January 11, 2022

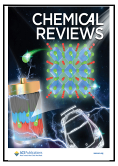

© 2022 American Chemical Society

https://doi.org/10.1021/acs.chemrev.1c00594

1. INTRODUCTION

Inorganic materials with ion conducting properties are attractive for both their unique structures and wide range of applications, including sensors, electrochromic glasses, fuel cells, supercapacitors, and batteries. The history of inorganic solid-state electrolyte (SSE) research can date back to 1830s when Michael Faraday found a conduction phenomenon in lead fluoride (PbF_2) and silver sulfide (Ag_2S). In 1914, the first superionic conductor silver iodide (AgI) was discovered with extraordinary ionic conductivity that was similar to that of the liquid phase.[1] In the 1960s, fast sodium ion transportation properties were found in β-alumina ($Na_2O{\cdot}11Al_2O_3$), which was later utilized to develop high-temperature sodium−sulfur batteries used in South Africa and Japan in 1980s. In the same period, rechargeable batteries were in demand and under extensive studies. The successful demonstration of inorganic SSEs in batteries and great potentials in energy-related applications stimulated the scientific community and triggered vast research efforts on solid-state sodium-ion conductors as well as lithium-ion conductors for rechargeable batteries.

For the previous two centuries, most batteries have been based on liquid electrolytes largely due to their high ionic conductivity and excellent wetting of electrodes. However, they are subject to corrosion, leakage, narrow electrochemical stability voltage windows and flammability. Recently, these drawbacks have become more prominent because of the increasing demand for more reliable safety and longer durability from the booming electric vehicle market and grid-scale energy storage. Replacing the liquid electrolytes with inorganic SSEs provides an exciting opportunity to overcome these problems considering the intrinsic safety and stability features related to the solid-state materials. Moreover, incorporation of inorganic SSEs in batteries also provides opportunities to unlock new battery chemistries with exceptionally high energy densities, such as lithium metal batteries (e.g., Li metal anode pared with high-voltage cathodes), lithium−air, and lithium−sulfur systems, by offering physical barriers to stop lithium dendrite propagation. Owing to these attractive properties, inorganic SSEs for batteries have emerged as a crucial research topic in both the scientific community and industrial communities, and they are highly anticipated to bring enormous changes to the way of energy utilization in the near future.

Although there are a large number of inorganic material categories, it is still challenging to find a satisfying electrolyte for solid-state batteries. The prerequisite of the electrolytes is ionic conduction. Ion conduction behavior in crystalline solids is significantly different from that in liquids where ion transport is governed by the movement of solvated ions in the solvents and is normally fast. As shown in Figure 1a, ionic diffusion in inorganic materials relies on the hopping of ions between the adjacent available sites through a higher energy barrier due to the geometry constraint and electrostatic interaction. Generally, the hoping mechanism in one ionic conductor can be established on the direct hopping or knock-off hopping,[2] which are illustrated in Figure 1b. In the first "direct hopping" mechanism, an individual ion (e.g., Li^+, Na^+) hops from one lattice site to its adjacent vacant site, while the "knock-off hopping" represents an indirect interstitial mechanism wherein an interstitial atom pushes the matrix atom toward another interstitial and realize ion conduction. These classic conduction mechanisms are based on single-ion migration, which is not sufficient to depict the ion conduction in superionic conductors. He et al. reported that the fast diffusion in superionic conductors does not occur through isolated ion hopping as is typical in solids, but instead proceeds through concerted migrations of multiple ions with lower energy barriers (Figure 1c).[3]

According to the Arrhenius model, which has been generally used to describe ionic conduction in crystalline solids, the ionic conductivity σ can be expressed as

$$\sigma = \frac{A}{T} n \exp\left(-\frac{E_A}{k_B T}\right) \tag{1}$$

where A is a pre-exponential factor, T is the temperature in Kelvin, n is the concentration of mobile carriers, E_A is the activation energy of diffusion, and k_B is the Boltzmann constant. Point defects in solids, such as Schottky and Frenkel defects (Figure 1d), are the predominant carriers for ion conduction. In this regard, most inorganic materials cannot conduct ions effectively because of the lack of available defects for ion migration or the high activation energies.

Thanks to the progress in crystal structure engineering, several inorganic compounds were developed with extrinsic structure defects and demonstrated excellent ionic conductivities. These materials mainly consist of two sublattices, a backbone composed of immobile ligands connected through polyhedra and a sublattice of mobile ions (Li^+ or Na^+). There are sulfide, oxide, halide, nitride and hydride SSEs based on the main composition of the backbone, all of which have been intensively investigated and optimized for higher ionic conductivity through composition variation. It is worth noting that studies on these SSEs with various compositions rely on the understanding of intrinsic crystal structures, which promotes the development of high-performance electrolytes through rational design instead of trial and error. It has been found that only a limited number of inorganic materials sharing particular structures are capable of conducting Li^+ or Na^+ ions, but not all of them. The most studied structures come from families such as LISICON-like (lithium superionic conductor), argyrodite, garnet, NASICON-like (sodium superionic conductor), and perovskite structures, as shown in Figure 1e.

The LISICON-like and argyrodite structures have been mainly found in sulfide- and oxide-based electrolytes, and they can offer very high ionic conductivities, particularly when sulfur is used as the main component of the backbone. The conductivities of $Li_{10}GeP_2S_{12}$ (LISICON-like) and Li_6PS_5Br (argyrodite) were found to be as high as 1.2×10^{-2} and 7×10^{-3} S/cm, respectively.[4,5] However, the introduction of sulfur in the backbone also lead to decreased stability, which is embodied as extreme sensitivity toward moisture and tendency to generate toxic hydrogen sulfide. The garnet structure mainly exists in oxide-based electrolytes and it is associated with very high stability and satisfying ionic conductivity. For example, $Li_7La_3Zr_2O_{12}$ (LLZO) and its derivatives have been found to be very stable in ambient condition and even against lithium metal, while the ionic conductivity is usually on the order of 10^{-3} to 10^{-4} S/cm.[6] Nevertheless, the conductivity in this structure is quite sensitive to grain boundaries. Careful control over the high-temperature sintering process is necessary to reduce grain boundaries and achieve high densities and conductivities. The NASICON-like and perovskite structures are less conductive than the previous examples but subject to grain boundary issues as well. The detailed structural features of these examples have been analyzed and thoroughly discussed in a number of previous works.[7−9] Despite the tremendous efforts on optimizing these electrolytes for solid-state batteries, it seems that none of them are perfect and the search for new candidates with unexplored structures are becoming more and more prominent.

Recently, a new type of structure called antiperovskite has attracted increasing attention in inorganic material research as it has demonstrated an amazing array of physical and chemical properties such as superconductivity, negative thermal expansion, luminescence and catalysis.[10] Antiperovskites have the same topology as perovskites but adopt reversed ionic arrangement, which means unique anion-centered units in antiperovskites as compared with the conventional cation-centered ones in perovskites. The importance of this arrangement has long been recognized by solid-state chemists during the study of the aforementioned properties. More recently, the structural features of antiperovskites were successfully utilized to introduce superb ionic conduction in solid compounds. Antiperovskite Li_3OA (X = Cl, Br) compounds have been designed and synthesized.[11] They displayed lithium diffusion activation energies as low as 0.2−0.3 eV, with ionic conductivities of $\sigma > 10^{-3}$ S/cm at room temperature, and even reach superionic conduction of $\sigma > 10^{-2}$ S/cm at temperatures exceeding 250 °C. In comparison, the highest lithium-ion conductivity in the perovskite structural family was in the order of 10^{-3} to 10^{-4} S/cm, with an activation energy of around 0.4 eV. The big difference is caused by the fact that the cation position in antiperovskites is completely different from that in perovskite, which provides a distinct local environment for mobile ions and thereby changes their mobility. In fact, the anion sublattice of antiperovskites is in a body-centered cubic (bcc) packed pattern that has been proposed to promote high ionic mobility in all kinds of structural families.[12]

Moreover, the new electrolytes also displayed other advantages, such as extraordinary stability toward lithium metal and relatively low melting points, which have been highly anticipated but rarely found in most conventional electrolytes. Many traditional electrolyte systems are not stable with the highly reductive lithium metal anode due to the existence of some high valence metal ions, for example, Ti^{4+} in perovskite $Li_{3x}La_{2/3-x}\square_{1/3-2x}TiO_3$ (LLTO, where $\square$ represents a vacancy) and Ge^{4+} in $Li_{10}GeP_2S_{12}$. These cations are a key component of the cation-centered polyhedral units that constitute the backbone of the electrolyte. However, they can be reduced by lithium metal, thus deteriorating the interface between the electrolyte and electrode. In comparison, Li_3OA electrolyte contains only Li^+ cations and O^{2-} and A^- anions that are both in their lowest valence state, affording the stability toward lithium metal. On the other hand, the melting points of Li_3OA electrolytes are below 350 °C. The extraordinarily low temperature will enable straightforward fabrication of dense, large-area thin films, a critical process in the preparation of compact layers for large size batteries. Other electrolytes have to be molded through hot pressing or high-temperature sintering in order to achieve reasonable densities, and it will become more challenging if large-area films are needed.

The discovery of the Li_3OA electrolytes has opened a new avenue to the development of high-performance SSEs for solid-state batteries. Encouraged by this success, many research efforts have been devoted to the antiperovskite structure electrolytes and significant progress has been made. The ionic conductivity of antiperovskite system at room temperature has been boosted to 2.5×10^{-2} S/cm for Li-based antiperovskites and 4.4×10^{-3} S/cm for Na-based antiperovskites,[13,14] with some electrolytes having been demonstrated in full cells.[15,16] Considering that the antiperovskite structure can be readily manipulated via chemical, structural and electronic routes to optimize the physicochemical properties, a giant leap toward practical solid-state batteries based on antiperovskite electrolytes can be anticipated. However, research on antiperovskite electrolyte is just in the initial stage and there are some obstacles that may delay the progress, including the unawareness of the structural variations, little attention paid to grain boundary effects, and limited understanding of the interface stability in full cell systems with antiperovskite electrolytes. Thus, a thorough discussion on antiperovskite electrolytes from basic structure and synthesis to final performance in devices based on past structure study and recent electrolyte progress is very necessary for researchers.

In this review, we aim at filling this void by presenting a systematic introduction of antiperovskite electrolytes and summarizing the recent breakthroughs in material preparation, understanding of ion conduction mechanisms, and structure manipulation for enhanced performance in solid-state batteries. In the following sections, we start from introducing the general structural features of the antiperovskites. We then discuss the ion diffusion mechanisms based on the results from both simulation and experimental characterization and extend to structure manipulation for enhanced conduction. We also discuss several basic preparties of antiperovskite electrolytes, including phase formation stability, electrochemical stability, air stability, as well as mechanical property. Next, we discuss the interface issues and applications in battery devices. We then summarize and discuss all the reported and potential methods for antiperovskite electrolytes synthesis and cell preparation. We conclude with an overview of the challenges of antiperovskite electrolytes and perspectives for further investigations and practical applications.

2. STRUCTURAL FEATURES OF ANTIPEROVSKITES

Antiperovskites, which are derived from perovskites, are perhaps the most adaptable and well-studied crystal structure. A standard perovskite (aristotypic perovskite) has the general ABX_3 stoichiometry with cubic structure and $Pm\bar{3}m$ space group. A, B, and X sites are at the corners, body-centers and face-centers of the cube, respectively, where X is an anion and A and B are cations with different sizes (A being larger than B). Each B cation is coordinated by six X anions, forming a cation-centered BX_6 octahedron. The perovskite framework is composed of the BX_6 octahedra under a corner-sharing connection pattern, while A cation fills the dodecahedra cavity with a coordination number of 12. Antiperovskites have the perovskite topology and same ABX_3 stoichiometry, but with an electronically inverted BX_6

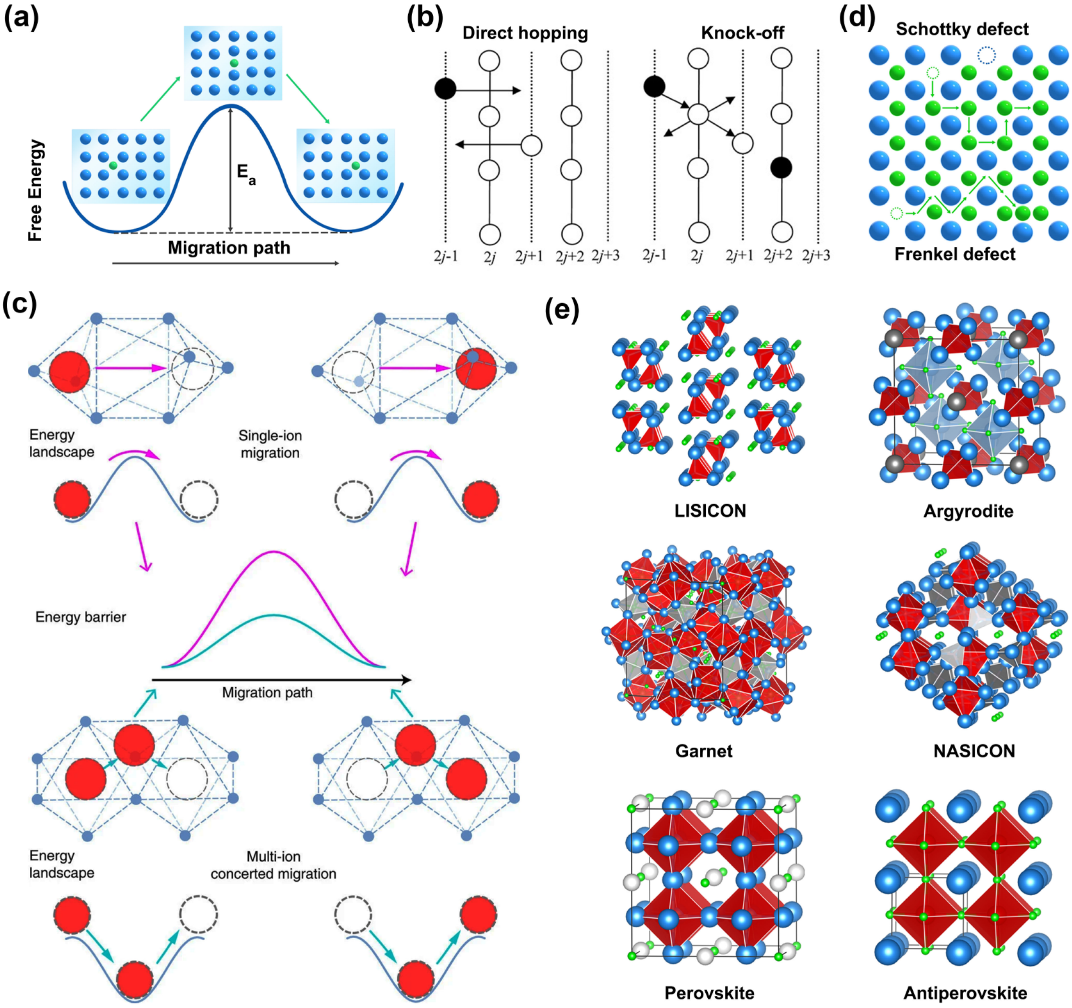

Figure 1. (a) Schematic illustration of ion diffusion in SSEs. (b) Schematic illustration of the direct hop mechanism and knock-off mechanisms. Reproduced with permission from ref 2. Copyright 2012 American Chemical Society. (c) Schematic illustration of single-ion migration and multi-ion concerted migrations. Reproduced with permission from ref 3. Copyright 2017 Springer Nature Limited under the Creative Commons Attribution 4.0 International License (http://creativecommons.org/licenses/by/4.0/). (d) Schematic illustration of Schottky defect and Frenkel defect in a crystal lattice. Schottky defect forms when ions with opposite charges leave their lattice sites so as to maintain an overall electroneutrality. Frenkel defect happens when one atom or smaller ion leaves its lattice site and lodges in a nearby position, thus becoming an interstitial and creating a vacancy. (e) Typical structural families of inorganic electrolyte (lithium atoms are marked by green spheres).

building unit where the anion is at the octahedral center (B-site) and cation is at the octahedral vertices (X-site). In a standard ionic antiperovskite (Figure 2a), for example, Li_3OBr and Na_3OCl, X is a monovalent cation (e.g., alkali metal), B is a divalent anion (e.g., chalcogen), and A is a monovalent anion (e.g., halogen). Given the rule of "cation-first" in inorganic nomenclature, antiperovskite structure is more often described as X_3BA. In addition, there is another important branch of compounds possessing antiperovskite structure, where X is a transition-metal element or rare-earth element, B is boron, carbon or nitrogen, and A is from the main family elements or lanthanides. For example, the electrocatalyst $Co_3InC_{0.7}N_{0.3}$,[17] the giant magneto resistance material Cu_3PdN,[18] and the superconductor Ni_3MgC[19] are metallic compounds of such antiperovskite structure. The discussion here is focused on the ionic antiperovskite structure, which has the potential to generate ionic conduction.

In fact, most perovskite and antiperovskite compounds do not adopt the standard cubic symmetry or the ABX_3 stoichiometry. More often than not, they are in the form of distorted structures or nonstoichiometry whether they are intentionally designed or not, which can be attributed to their intrinsic structural flexibility. There are several important derivatives from standard perovskite and antiperovskite, which we would like to classify as distorted structures, deficient structures, ordered/disordered structures, etc. The applications of perovskite and antiperovskite compounds have been remarkably broadened just because of the existence of these derived structures as their thermal, mechanic, electric, and magnetic responses all correlate with the changes in the atomic structure. In this section, we will discuss the opportunities in giving general descriptors correlated with the antiperovskite structures including the standard cubic one and the derivatives and summarize the structural features of the typical derivatives.

2.1. Geometric Descriptors

The formation of an antiperovskite structure can be predicted geometrically using the regularity discovered in perovskites. In an ideal cubic unit cell of perovskites, the cell axis a is a function of the ionic radii as described by equation:

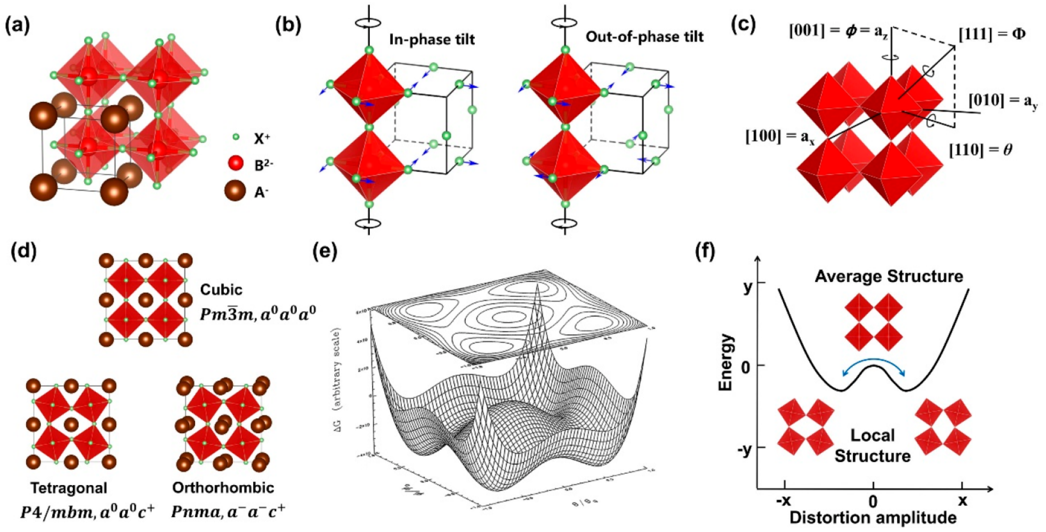

Figure 2. (a) Octahedral framework model of cubic X_3BA antiperovskite. (b) Schematic illustration of the in-phase and out-of-phase tilting modes. (c) BX_6 octahedron tilting directions relative to the pseudocubic cell axes. Tilt axes in Glazer notation are displayed as a_x, a_y, and a_z. Also shown are the two independent tilts θ about [110] and ϕ about [001] as applied by Wolf and Bukowinski,[36] and the one tilt Φ about the 3-fold axes [111] as demonstrated by O'Keeffe and Hyde.[37] θ, ϕ, and Φ can be related by vector operation. (d) Illustration of the cubic ($Pm\bar{3}m$), tetragonal ($P4/mbm$), and orthorhombic ($Pnma$) structures with Glazer notation. (e) Free energy of the perovskite structure as a function of normalized tilts $\theta/\theta0$ and ϕ/ϕ_0 plotted in a three-dimensional (3-D) space. Reproduced with permission from ref 38. Copyright 1998 Academic Press. (f) A 2-D form of (e). It displays the energy minimum in the double-well potential.

$$a = \sqrt{2}(R_A + R_X) = 2(R_B + R_X) \qquad (2)$$

where R_A, R_B, and R_X represent the ionic radii of A, B, and X ions, respectively, with values generally obtained from the Shanon and Prrewitt (SP) approach,[20,21] as shown in Table 1. If there exist a mismatch in the ionic radii, for example, a decreased size of the A ions, the BX_6 octahedra will tilt in order to fill space. As a result, the original cubic cell will be distorted, producing a lower crystallographic symmetry. The ratio of the two expressions in eq 2, named Goldschmidt tolerance factor t,[22] is then used to evaluate the structural symmetry, or to predict the existence of new perovskite structure compounds, as described in equation:

$$t = \frac{R_A + R_X}{\sqrt{2}(R_B + R_X)} \qquad (3)$$

Table 1. Effective Radii of Some Common Cations and Anions Used for Perovskite/Antiperovskite Materials

cation	ionic radius (pm)	ref	anion	ionic radius (pm)	ref
Li^+	76	21	F^-	133	21
Na^+	102	21	Cl^-	181	21
K^+	138	21	Br^-	196	21
Ag^+	115	21	I^-	220	21
Be^{2+}	45	21	O^{2-}	140	21
Mg^{2+}	72	21	S^{2-}	184	21
Ca^{2+}	100	21	Se^{2-}	198	21
Sr^{2+}	118	21	Te^{2-}	221	21
Ba^{2+}	135	21	$[HCOO]^-$	136	23
Al^{3+}	54	21	$[BH_4]^-$	203	24
Ga^{3+}	62	21	$[AlH_4]$-	266	24
In^{3+}	94	21	$[BF_4]^-$	243	24
Ti^{4+}	61	21	$[BCl_4]$-	329	25
$[NH_4]^+$	146	23	$[OH]^-$	140	26
$[H_3NOH]^+$	216	23	$[CH_3]^-$	260	26
$[CH_3NH_3]^+$	217	23	$[NH_2]^-$	171	26
$[H_3N\text{-}NH_2]^+$	217	23	$[SCN]^-$	250	27
$[(CH_2)_3NH_2]^+$	250	23	$[ClO]^-$	170	27
$[NH_2(CH)NH_2]^+$	253	23	$[SO_4]^{2-}$	276	28
$[C_3N_2H_5]^+$	258	23	$[SeO_4]^{2-}$	297	28

The basic cubic perovskite structure has $t \approx 1$, such as $SrTiO_3$ ($t = 1.009$, calculated with the Shannon ionic radii). However, most antiperovskite and perovskite materials adopt lower-symmetry structures (or hettotypes). Statistical analyses indicate that the t values of cubic perovskite mostly drop in the range of 0.9−1.0, while t values in the range of 0.8~0.9 correspond to tetragonal or orthorhombic perovskite structures, and lower t values give other structures with even lower crystallographic symmetry. On the other hand, if the t value is larger than 1 due to an oversized A or an under-sized B the cubic lattice will be destroyed and converted to hexagonal lattice (e.g., $BaNiO_3$ with $t = 1.13$). The BX_6 octahedra in this case are face shared, in contrast to the classical corner-sharing pattern for perovskites. In fact, there has been controversy related to the classification of compounds with the face-sharing or edge-sharing octahedral network.[29] This paper will focus on the classical pattern of corner-sharing octahedra. Goldschmidt tolerance factor t has been extensively used to predict the formability of potential perovskite and antiperovskite structures. However, it should be noted that it is a necessary but not sufficient condition. There are some inorganic compounds that do not possess perovskite structure but still have t values in the favorable range of 0.8−1.0, such as Al_2O_3−B_2O_3, Li_2O−As_2O_5, and Cu_2O−P_2O_5 systems.[30] The Goldschmidt method is mainly focused on the effect of A-site ions on the stability of whole structures, which ignores the formability of BX_6 octahedra. In fact, an undersized B ion cannot afford intimate contact between the ion and the six X ions around it, lowering the coordination number and ultimately decreasing the stability of BX_6 octahedra. Octahedral factor μ was thus introduced as a complement to the Goldschmidt tolerance factor,[30] as described in equation:

$$\mu = \frac{R_B}{R_X} \tag{4}$$

A reasonable μ value has been commonly proposed to be larger than 0.414 (or $\sqrt{2} - 1$); however, there is no defined upper limit of μ, with samples of perovskite structures possessing μ = 0.89.[31] A two-dimensional (2-D) structural map has been proposed based on the tolerance factor t and the octahedral factor μ (known as the t-μ map),[30,32] providing a reliable prediction on the formation of ABX_3 perovskite structures. More recently, a new tolerance factor τ was also developed in an attempt to provide higher accuracy in predicting the stability of the perovskite structure,[33] which has the form:

$$\tau = \frac{R_X}{R_B} - n_A\left[n_A - \frac{R_A/R_B}{\ln(R_A/R_B)}\right] \tag{5}$$

where n_A is the oxidation state of A cations. The formability of a perovskite structure increases as the τ value decreases, with a maximum value of 4.18. It might be feasible to use the aforementioned structural descriptors as a reference to guide the selection of chemical composition for antiperovskite electrolytes. However, it should be noted that they are only a rough estimate, and the practicality and accuracy have not been systematically verified yet.

2.2. Distorted Structure

Structure distortion is the most common phenomenon in antiperovskite and perovskites. Even the perovskite prototype $CaTiO_3$ mineral (t = 0.973) displays a certain degree of distortion from the ideal cubic symmetry. Distortion appears to be driven not only by internal factors such as changes in composition, but also in response to external stimulus such as changes in temperature and pressure. According to the above discussion, the cubic antiperovskite will collapse and form a distorted structure if the dodecahedra cavity cannot be filled by a small cation on the A site. For example, the cubic antiperovskite electrolyte Li_3OBr approaches a more distorted structure when more Br^- anions are successively substituted by the smaller Cl^- anions, which is accompanied by a decreased tolerance factor t from 0.91 for Li_3OBr to 0.85 for the chlorine-counterpart Li_3OCl. Temperature-related structure distortion can be well-demonstrated by the lithium-halide-based quaternary compounds, $LiBr{\cdot}H_2O$ and $Li_2(OH)Cl$. Both of these possess cubic antiperovskite structure with $Pm\bar{3}m$ space group at slightly elevated temperatures (above 33 and 35 °C, respectively), but adopt low-symmetry orthorhombic structure below the critical temperatures (with a space group of $Cmcm$ and $Pmc2_1$, respectively). As a result, they showed a significant drop in ionic conductivity even with minor temperature changes near the critical point. Pressure triggered lattice distortion is often discussed in geosciences and takes place under extreme conditions.[34] However, pressure plays a more complicated role as compared with temperature in regulating structure distortion. Distortion from the cubic symmetry may increase, decrease or even cross over with increasing pressure, as displayed by $GdFeO_3$-type perovskites.[35]

It is worth noting that the influences of composition, temperature and pressure on structure distortion are interrelated. Modification of the chemical composition could in turn affect the temperature- or pressure-driven lattice distortion, which benefits the maintenance of extraordinary physiochemical properties that previously displayed at strict conditions to milder conditions. For example, the orthorhombic-to-cubic transition at 35 °C in the aforementioned $Li_2(OH)Cl$ antiperovskite electrolyte can be completely suppressed by lithium doping and replaced by a tetragonal-to-cubic transition at −60 °C, providing sufficient temperature range to maintain the highly conducting cubic phase with higher ionic conductivity.[39] Considering the potential existence of superionic conducting phases with even higher symmetry than $Pm\bar{3}m$ in the mixed-halogen antiperovskite electrolyte $Li_3OCl_{0.5}Br_{0.5}$ at elevated temperatures (10^{-1} S/cm and 10^{0} S/cm 248 and 266 °C, respectively), retaining the same crystal lattice at room temperature would be highly desirable. To achieve this goal, a deep understanding of the nature of the lattice distortion process and phase transition is necessary.

Lattice distortion can be attributed to three mechanisms: octahedral deformation, dynamic A- or B-site off-centering, and octahedral tilting. The first mechanism, octahedral deformation, is the result of Jahn-Tell distortion of cations which possess partially filled d shells (e.g., Cu^{2+}, Mn^{3+}).[40] The second mechanism is also related with electronic instabilities of metal cations. The long-pair cations on the A sites (e.g., Pb^{2+}, Bi^{3+}) or high-valent d^0 cations on the B sites (e.g., Ti^{4+}, Nb^{5+}) tend to shift out of the coordination center under the second-order Jahn−Teller effect. The third mechanism is responsible for most distorted cases. It occurs as a result of tilts of rigid BX_6 octahedra to accommodate A ions if they are too small for the 12-fold sites within the original octahedral network. In these cases, the A-X bond lengths will be adjusted, changing the A-site coordination from the original 12 to a minimum 8 depending on the tilting pattern, while the first coordination sphere around the B-site ion will remain unchanged in order to achieve the lowest energy mode.[41] Octahedral tilting can be also explained by the vibrational instability of the crystal lattice. It is known that crystalline lattice vibrates under finite temperatures (denoted as phonon). Some lattice vibrations are stable, but some vibrations along particular directions are not, for example the Brillouin zone-boundary phonon modes M_3 and R_{25}. These specific phonon modes undergo critical softening and condensation (or freezing-in) processes as pressure or temperature changes, which has been recognized as the driving force for octahedral tilting.[42] As shown in Figure 2b, the M_3 soft mode corresponds to the in-phase tilt, where rotations of the adjacent octahedra proceed in the same sense. R_{25} corresponds to the out-of-phase tilt, where rotations of the adjacent octahedra are in the opposite sense. Combination of the in-phase and out-of-phase tilts thus leads to the formation of distinct space groups.

Glazer has developed a simple classification system and related these combinations to the unit cell geometries in perovskites.[43,44] In Glazer notation, octahedral tilting is viewed as a combination of component tilts around three orthogonal Cartesian axes that are coincident with the axes of the cubic unit cell in aristotype ([100], [010], and [001] in Figure 2c). The tilted structure is described as a*b*c*, in which a, b and c represent unequal angles of tilt around the [100], [010], and [001] directions, respectively. Letters may appear repeatedly in the case of equal tilts around the different axes. The superscript * adopts +, −, or 0 to indicate the in-phase and out-of-phase tilts or no tilt, respectively. For example, the notation of $a^-a^-c^+$ for the orthorhombic structure represents out-of-phase titles along the [100] and [010] directions with same tilt angles and in-phase tilt along the [001] direction (Figure 2d). A total of 23 tilt systems were identified in all possible combinations of titling in Glazer notation, and 15 of them were confirmed via group-theoretical analysis later.[45] Other notations based on two tilts θ

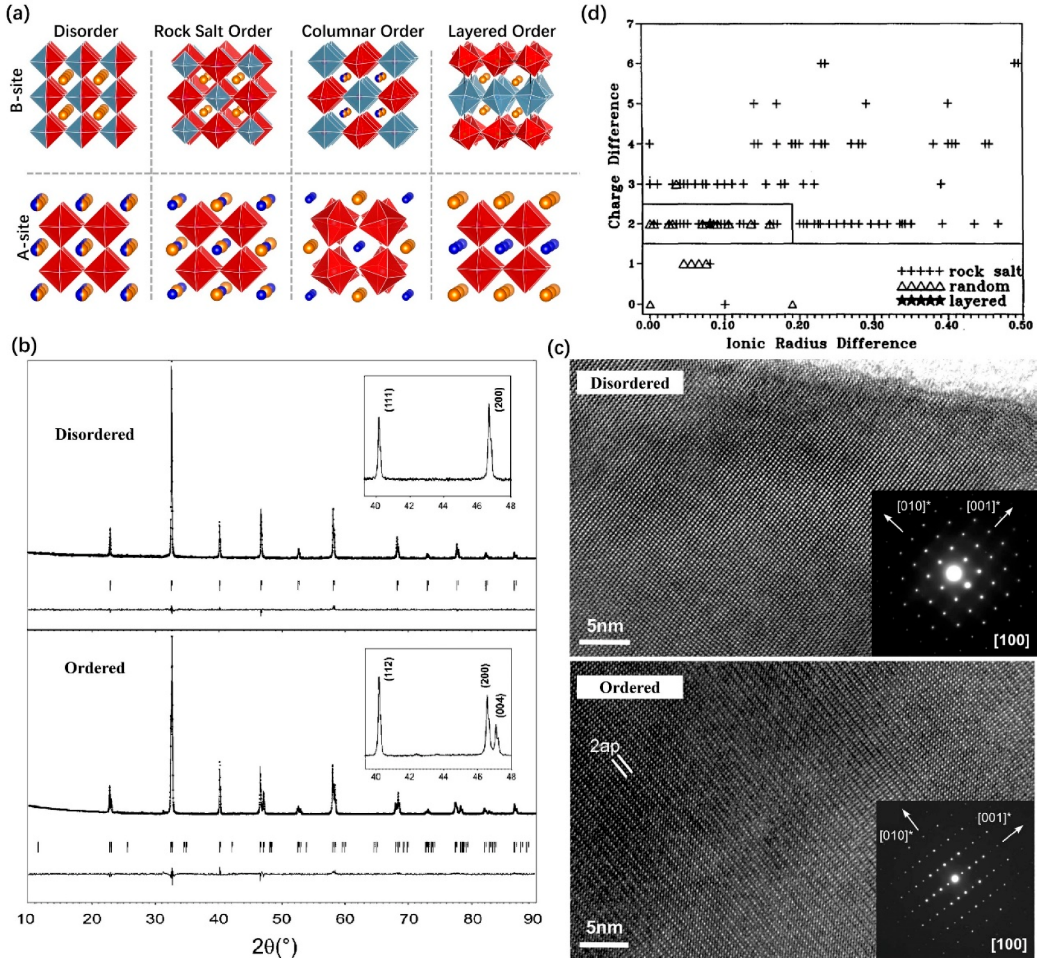

Figure 3. (a) A- and B-site ordering schemes in perovskites and antiperovskites. (b) Rietveld refinement curves of the XRD data for the disordered and ordered $LaBaCo_2O_6$ perovskite. The inset shows a magnified area where a small change in the peak width is observed. (c) High-resolution electron microscope images and corresponding selected area electron diffraction patterns along the [100] direction for the disordered and ordered layered $LaBaCo_2O_6$ perovskite. The superstructure of the ordered $LaBaCo_2O_6$ (1:1 ordered stacking of LaO and BaO layers) is clearly identified by the doubling of the cell parameter along the [001]* direction with respect to the simple perovskite cell of the disordered $LaBaCo_2O_6$. Reproduced with permission from ref 58. Copyright 2008 American Chemical Society. (d) Charge difference versus ionic radius difference for $A_2B'B''X_6$ perovskites. Reproduced with permission from ref 59. Copyright 1994 Elsevier Ltd.

and ϕ[36] or only one tilt system Φ[37] were also developed to describe distortion. Figure 2e shows the free energy of perovskite structure as a function of θ and ϕ, which clearly reflects a minimum energy well change from the multiminimum well in the orthorhombically distorted phase to the singe-minimum well in the cubic phase at the transition temperature, and explain the softening phenomena accounting for octahedral tilting.[38] The octahedral tilting theories are of great significance for researchers, through which the possible sequences or routes of the successive Ph. Transit from the ideal cubic phase to other low-symmetry phases can be revealed clearly, thus helping to predict new antiperovskite/perovskite structures or to understand the new properties triggered by minor changes in composition, temperature or pressure. Detailed discussion on the octahedral tilting patterns and corresponding connections to order parameters can be found elsewhere.[42]

2.3. Mixed Sublattice and Ordering

Antiperovskite and perovskite compounds have extraordinary structural flexibility with regard to anionic and cationic replacements and tolerance to ionic defects, which has been used with much success to build new materials or to optimize physiochemical properties of parent materials based on rational design. In this part, a summary of the structural features of the antiperovskite/perovskite derivatives with mixed ions on the crystallographic sites will be presented. The presence of mixed ions can be found on the A, B, or X site with a disordered arrangement, and in varying proportion.[11,46−48] For example, antiperovskite electrolytes $Li_3OCl_{1-x}Br_x$ and $Na_3OBr_{1-x}I_x$ possess a disordered A sublattice composed of halide ions.[11,49] These halide ions are randomly distributed on the A sites under a statistical occupation. Therefore, structures with these disordered sublattices are also known as solid-solution structures.

The sublattice arrangement also proceeds in a more interesting pattern, the ordered-pattern, characterizing perovskites and antiperovskites. This ordering behavior occurs mainly on A or B sites, which has been investigated experimentally and theoretically, and a detailed description on this topic can be found elsewhere.[40] The unit cell of the corresponding structures will be enlarged as a result of sublattice ordering, leading to simple $A'A''B_2X_6$ or $A_2B'B''X_6$ "double perovskite/antiperovskite", or complex $A'A''B'B''X_6$ "quadruple perovskite/antiperovskite" if ordering occurs on both sites. The ordered arrangement has three different styles, as shown in Figure 3a. In the first style, the A or B sublattice is alternatively occupied by the two different ions in all three dimensions, forming a pattern that is similar to cation and anion arrangements in a rock salt structure, for instance the $NaBaLiNiF_6$ and the mineral elpasolite K_2NaAlF_6.[50,51] In some cases (e.g., $BaLaMn_2O_6$ and La_2CuSnO_6),[52,53] the different ions in A or B sublattice alternate in only one direction, which allows the formation of the layered order. Ordering may proceed in the third style, a columnar arrangement, where the two ions alternate in two directions (e.g., $CaFeTi_2O_6$ and $NdSrMn_2O_6$).[54,55] The above three ordering styles can be described in another way by using the alternating direction, which results in the <111>, <100>, and <110> ordering corresponding to rock salt, layered and columnar ordering, respectively. It is worth noting that the sublattice arrangement will become more complicated if chemical species is considered in addition to the chemical order. In addition, the above discussion is just based on the precondition that the ratio of the two different ions is 1:1; in fact, other ratios including 1:2 and 1:3 are also possible.[56] The variety of A (or B) sublattice would be remarkably widened by combining the chemical order and species. X-site ordering occurs mostly when accompanied by A-site (or B-site) ordering and vacancies on X sites. "Pure" X-site ordering has been rarely reported, with $SrMO_2N$ (M = Nb, Ta) compounds being one of the limited examples. These compounds have demonstrated an interesting partial oxide-nitride order in the X sublattice, where oxide and nitride are arranged in a $1O/2(O_{0.5}N_{0.5})$ order.[57]

Similar to the structure distortion, the subtle structural difference caused by sublattice ordering in perovskite or antiperovskite cannot be determined conclusively through powder X-ray diffraction alone in some cases (Figure 3b). Other characterization techniques, such as high-resolution electron microscope and corresponding selected area electron diffraction pattern studies, are suggested to reveal the difference, as shown in Figure 3c. Very often in previous perovskite and antiperovskite research, sublattice ordering was not identified. However, it may have profound influence on materials' physiochemical properties. This can be well demonstrated by the representative case of disorder−order phenomena in $LaBaMnO_6$ perovskite. By controlling the oxygen pressure, $LaBaMnO_6$ perovskite with disordered or ordered La^{3+} and Ba^{2+} were synthesized and displayed distinctly different colossal magnetoresistance properties.[52] The Curie temperature was only 270 K for the disordered phase, but it increased to 335 K for the ordered phase.

The driving force for the sublattice ordering in perovskite and antiperovskite structures is a highly interesting topic, however, it is not fully understood. Generally, thermodynamic competition between different structural arrangements is dominated by entropy under the synthesis conditions for most inorganic compounds, therefore statistically disordered arrangement is preferred. To overcome this preference and turn to ordered arrangement, a strong enthalpic motivation must be provided. Large differences in charge, ionic radius or coordination preference between the ions have been recognized as such motivations after intensive research efforts. Sublattices composed of these ions are prone to ordering, which provides lower lattice strain and better local charge neutrality.[60] Because of the unique structural flexibilities, perovskite and antiperovskite structures are able to accommodate distinct ions in the same sublattice, thus leading to the observed ordering phenomena. The minimum differences that are required for ordering have not been described quantitatively from the structural point of view, as they may vary from each other in different chemical systems; however, research based on statistical investigation of a large number of $A'A''B'B''X_6$ perovskites or perovskites may provide a reasonable estimation. As shown in Figure 3d, a plot of B-site charge difference versus ionic radius difference was constructed and clearly showed the tendency of ordering in perovskites when the charge difference was larger than two, and disordering when the charge difference was less than two. Both ordered and disordered arrangement were identified when the charge difference was two, while the ordered structures dominated when ionic radius difference was larger than 0.2 Å.[59] Nevertheless, this ordering behavior based on charge difference in perovskite may be less common in antiperovskite systems as the A and B sites in antiperovskites are primarily occupied by anions, which have fewer potential reduction states as compared with cations and therefore result in relatively small charge difference. The reported Li_6OSI_2 and Na_6SOI_2 electrolytes are rare cases of antiperovskite with ordered sublattices.[26,61] According to the reports, the B sublattice is composed of alternating O^{2-} and S^{2-} anions in a rock salt arrangement. The ordering phenomena in these cases might arise from the radius difference (0.4 Å) as there in no difference in charge. Therefore, more double antiperovskite structures with ordered anion sublattice could be prepared by employing this strategy and introduce some new properties. However, structure determination based on single crystal diffraction, synchrotron X-ray diffraction, neutron diffraction or electron microscopy may be needed to distinguish the subtle structural changes. As mentioned above, simply matching the powder diffraction patterns from normal laboratory X-ray machines with those of already-known structures is unreliable.

2.4. Vacancy and Grain Boundary

Crystallographic defects are the most common phenomena in crystalline materials, including metals and inorganic compounds. There are four basic types of defects depending on the dimensions, which are point defects, linear defects, planar defects and bulk defects. Point defects correspond to irregular places that have a missing or extra atom (or molecule hereinafter). They include lattice vacancies (unoccupied lattice sites in an otherwise prefect crystal), self-interstitials (original atoms in space between regular atoms on lattice sites), impurity interstitials (foreign atoms in space between regular atoms on lattice sites), antisite substitutions (original atoms occupying the wrong lattice sites), and impurity substitutions (foreign atoms on lattice sites). Linear defects, also known as dislocations, describe a group of neighboring atoms that are not in their regular positions. Planar defects are interfaces between two homogeneous regions within a material, such as grain boundaries (interfaces between two grains of different orientations) and stacking faults (deviation of the lattice stacking sequence). Bulk defects are 3-D defects, such as voids (clusters of atoms missing from the lattice) and precipitates (clusters of atoms forming a different phase).

Among these defects, lattice vacancies are particularly common in perovskites/antiperovskites. In fact, perovskites and antiperovskites are known for their capability of accommodating a high-concentration of vacancies in the crystal lattice while maintaining the overall structural stability. The A-, B- or X-sites in these structures can be partially or even fully vacant. Partial atom replacement is often identified in ionic perovskites/antiperovskites as well as other inorganic com-

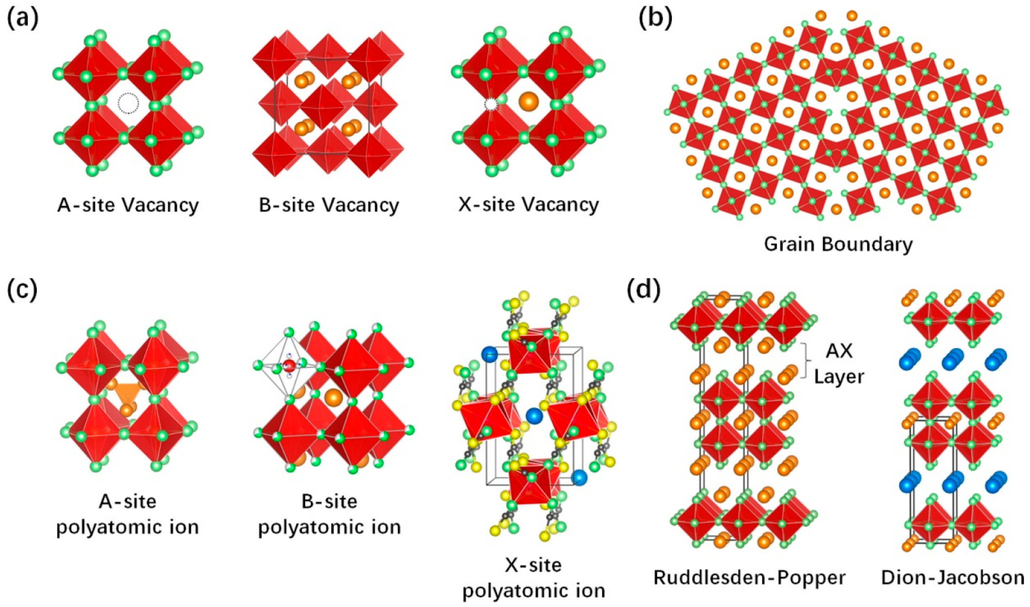

Figure 4. Schematic illustration of several typical derivative structures from the cubic ABX_3 aristotype. (a) Vacant structures (X-site ions are omitted in the middle image to better display the B-site vacancy). (b) Grain boundary structure. (c) Derivatives with polyatomic units. (d) Layered structures.

pounds, and usually give rise to nonstoichiometric compounds in which the chemical formulas depart from the integral ratio of A:B:X= 1:1:3. The nature of these deficient structures can be understood from a perspective of aliovalent substitution where host atoms are replaced by foreign atoms with distinct valence states. For example, Ca^{2+} (ionic radius = 99 pm) substitutes for Na^{+} (ionic radius = 102 pm) in antiperovskite Na_3OCl. Ca^{2+} cation should fit well on a Na-site forming a $Ca_{Na}^{\bullet}$ defect (according to the Kröger-Vink notation[62]); however, to maintain electrical neutrality, a second Na^{+} should be stripped from the lattice, resulting in a Na-site vacancy, V'_{Na}. The deficient structures are also caused by simply removing ions from the crystallographic sites. For example, Li^{+} cations in antiperovskite Li_3OCl may be depleted under some circumstances (e.g., high-temperature sintering), leaving V'_{Li} defects. The negatively charged defects are compensated by positive chlorine vacancies ($V_{Cl}^{\bullet}$). These pairs of vacancies are the Schottky defects shown in Figure 1d. Occasionally, the deficient structures are caused by misplacing one of the host ions in crystal lattice. It usually occurs in ionic compounds with small cations and large, highly polarized anions. The small cations will be probably accommodated in the interstices of the host lattice instead of the original crystallographic sites if the cavity is large enough, leading to the Frenkel defect in Figure 1d. In perovskite/antiperovskites, this defect structure can be engineered by a precise control on the size of dodecahedra cavity through octahedra unit selection or octahedra distortion. The high defect tolerance in perovskite/antiperovskites can be better demonstrated by compounds with highly vacant or even fully vacant A-, B-, or X-site, as shown in Figure 4a. For example, fluoride perovskites $\square AlF_3$ and $\square FeF_3$, and hydroxide perovskites $\square In(OH)_3$ and $\square Sc(OH)_3$ have completely empty A-sites. Many halide perovskites possess half vacant B-sites structures with the general formula of $A_2B\square X_6$, such as in $Cs_2Sn\square I_6$, and $Cs_2Ti\square Br_6$.[63] Antiperovskite compounds $Hg_3\square_3Q_2I_2$ (Q = S, Se, and Te) and $Fe_2\square OSe$ display highly vacant X-sites.[64,65] It is noteworthy that the B-site vacancies would interrupt the extended connectivity between the BX_6 octahedra in some cases, leading to the so-called "zero-dimensional (0-D)" perovskite/antiperovskite derivatives. Misunderstanding of these structures may occur by treating them as electronically isolated structures based on the structural dimensionality. In fact, these structures, though not connected geometrically, can maintain the close-packed network of X ions as in the stoichiometric ABX_3 that affords orbital overlap with neighboring octahedra.[63] These vacancy structures and their arrangement (e.g., ordered vacancy) in crystal lattice have been intensively studied as they may have significant influence on material properties. The early work on these aspects was reviewed by Mitchell et al.[41]

Compared with the most popular vacancy-type defect in crystalline materials, grain boundaries (Figure 4b) have drawn much less attention despite their wide existence, probably due to the difficulties in controlling grain boundary formation and understanding the complex relationship between the structure and overall performance. Nevertheless, this type of defect cannot be ignored particularly in perovskites/antiperovskites research, as they have demonstrated profound influence on the properties, which may be positive or negative. Generally, deformation movement through a solid tends to stop at a grain boundary; therefore, the existence of reasonable high-density grain boundaries contributes to good mechanical properties. Crystalline inorganics with fine grains are usually much stronger than those with coarse grains. However, grain boundaries are sometime harmful to material properties that are depended on carrier motion as it may stop at grain boundaries. For example, the grain boundaries in perovskite solar cells often cause nonradiative recombination losses, resulting in the decreased output.[66,67] Another typical example is their impact on ion mobility in SSEs, which is the topic of this paper. The ionic motion along and across the interface is usually hampered due to the introduction of undesirable interfacial structures or chemical disorder.[68] Although there exist enormous challenges, delving into the characteristics of grain boundaries is meaningful, and can help to guide future antiperovskite electrolyte designs that minimize or even utilize the influence of such defects.

2.5. Polyatomic Units and Dynamic Rotation

The crystallographic sites of most inorganic compounds are occupied by elementary ions, which is not the only case in perovskite and antiperovskite materials. As described above, these materials usually possess large dodecahedra cavities and outstanding framework flexibility, enabling a group of ions or molecules to be accommodated inside the dodecahedra cavities, which we named as polyatomic unit structures (including polyanions and polycations) (Figure 4c). These structures have been extensively reported in organic–inorganic hybrid perovskite materials for solar cells, where the A-sites are occupied by organic molecules, for example $CH_3NH_3^+$ and $CH(NH_2)_2^+$ in methylammonium lead iodide ($[CH_3NH_3]PbI_3$) and formamidinium lead iodide ($[CH(NH_2)_2]PbI_3$), respectively.[69,70] Inorganic polyatomic units have also been observed in ionic perovskites and antiperovskites, such as Tl_4^{4+}, NO_2^-, SO_4^{2-}, $ZnBr_4^{2-}$, and FeS_4^{5-} inorganic groups in perovskite $[Tl_4]SnTe_3$,[71] antiperovskite Na_3ONO_2,[72] $K_3[SO_4]F$,[73] $Cs_3Br[ZnBr_4]$,[74] and $Ba_3Br[FeS_4]$,[75] respectively. Though less reported, it is also possible to form perovskites/antiperovskites with polyatomic units on the B-sites. Typical examples are the antiperovskite $Li_2(OH)Br$ and $Li_2(OH)Cl$ compounds, in which B-sites are OH^- anions. Polyatomic units like CN^-, SCN^-, and $HCOO^-$ have also been successfully introduced on the X-sites as elongated ligands,[76] which allows the lattice to be extended. The introduction of the polyatomic units can enlarge the cell volume, and in the meantime enrich the local chemical environment, leading to a vast increase in complexity and potentially introducing new properties. For example, an enhanced stability may be achieved due to the additional supramolecular interactions through hydrogen bonds, Coulomb interactions, or van der Waals interactions.

From a structural standpoint, the formation of perovskites/antiperovskites with polyatomic ions or molecules on crystallographic sites can be evaluated by the corresponding tolerance factors. However, the effective ionic radii must be established first, which remains challenging. As described above, the ionic radii of elementary ions can be readily obtained through the Shanon and Prrewitt (SP) approach.[20,21] For the nonspherically symmetric units, the bond lengths vary due to the supramolecular interactions (e.g., hydrogen-boding interactions in organic $CH_3NH_3^+$ cation), making it difficult to define the ionic radius. Even for the highly symmetrical units (e.g., NH_4^+), radius changes significantly as their counterbalancing ions. Therefore, the effective ionic radii of these polyatomic units have not be determined conclusively yet. With the assumption of polyatomic units' free rotation about their centers of mass, Kieslich et al. suggested a set of effective ionic radii for organic units (as shown in Table 1).[23] The ionic radius of inorganic units (MY_n) was defined as the sum of the bond length of M-Y and the ionic radius of Y.[24] Although these ionic radii are not exact, they can be employed to estimate the tolerance factor and thus evaluate the formability of a new structure before synthesis.

The introduction of the polyatomic unit structures triggers an interesting dynamic disorder phenomenon. Unlike the elementary ions, the polyatomic units possess intrinsic geometries with internal degrees of freedom.[77] They are usually rotationally mobile at temperatures above certain critical point. Similar to the octahedral tilting described in Section 2.2, the dynamic disorder associated with polyatomic unit rotation occurs when the potential energy surface has a multiminimum well at the corresponding temperature (Figure 2e), and the structure is fluctuating between these local minima. The residence time of polyatomic units in various preferred orientations is extremely short, which has been proposed to be in the pico-second time scale according to multiple methodologies, such as quasi-elastic neutron scattering,[78] solid-state nuclear magnetic resonance,[79] dielectric relaxation,[80] and molecular dynamics simulation studies.[81] Therefore, it manifests as an averaged structure with a relatively high degree of symmetry. However, the rotation of polyatomic units is restricted or even becomes "frozen out" as temperature decreases, usually accompanied by a structural distortion and decrease in the overall structural symmetry. For example, the temperature-dependent average structures of $CH_3NH_3PbI_3$ perovskite have been studied by powder neutron diffraction.[82] Structure refinement results revealed that the $CH_3NH_3^+$ cations were orientationally disordered (3-D disorder) in the cubic phase above 327 K and adopted four possible orientations along <100> and equivalent directions (2-D disorder) in the tetragonal phase at 180 K, and were eventually aligned and directed into the square face of the unit cell (fully ordered) in the orthorhombic phase at 100 K. Considering that the simultaneous octahedra framework distortion was quite weak, the behavior of the polyatomic units might trigger the responds of overall structures, namely the continuous second-order phase transition started from 327 K and the first order transition at 165 K as revealed by temperature-dependent diffraction data. Certainly, the properties of perovskites/antiperovskites will be affected as a result of the dynamic disorder in polyatomic units. However, it changes case by case; detailed influence on ionic conduction will be discussed later.

2.6. Layered Structures

As mentioned above, the extended connectivity between the BX_6 octahedra a the major characteristic or requirement for perovskite/antiperovskite structures, although structural deviations may occur, for example when structure vacancies exist. Here, another case with repeated broken BX_3 backbones will be introduced, which is the layered derivatives. Ruddlesden–Popper (RP) phases are a typical example of such layered structures.[83] In the RP phases, which have a general $A_{n+1}B_nX_{3n+1}$ (or $(AX)(ABX_3)_n$) formula, the 2-D ABX_3 slabs composed of n layers of corn-connected octahedra are separated by one AX-rock salt layer, and are offset by half a unit cell (1/2, 1/2) transition from each other, as shown in Figure 4d. RP phases have been reported in oxide perovskites (e.g., Sr_2RuO_4 (n = 1), $Sr_3Ru_2O_7$ (n = 2), and $Sr_4Ru_3O_{10}$ (n = 3)) and halide perovskites (e.g., $Cs_2PbI_2Cl_2$ (n = 1) and $Cs_2SnI_2Cl_2$ (n = 1)).[84,85] RP phases have also been found in antiperovskite compounds, for example $Li_7O_2Br_3$ and Na_4OI_2, which have been studied as ionic conductors.[86,87] Dion-Jacobson phases, with a general formula of $A'[A_{n-1}B_nX_{3n+1}]$, possess a similar layered structure. In this structure, the ABX_3 slabs are separated by a large A′ ion layer while the displacement of ABX_3 slabs is either nothing (Figure 4d), or (1/2, 0) depending on the type of A′ ions.[88] The formation of this structure can be treated as a result of the steric demand from the large A′ ion (elementary ion or polyatomic ion) that cannot be accommodated in the BX_3 cage. The 3-D BX_3 network is thus broken along the stacking direction and keeps the continuous octahedra connection along the perpendicular plane.

2.7. Differences between Antiperovskite and Perovskite

In the preceding sections, we have summarized some key structural features that are shared by antiperovskite and perovskite. At the end of this part, we emphasize the structure

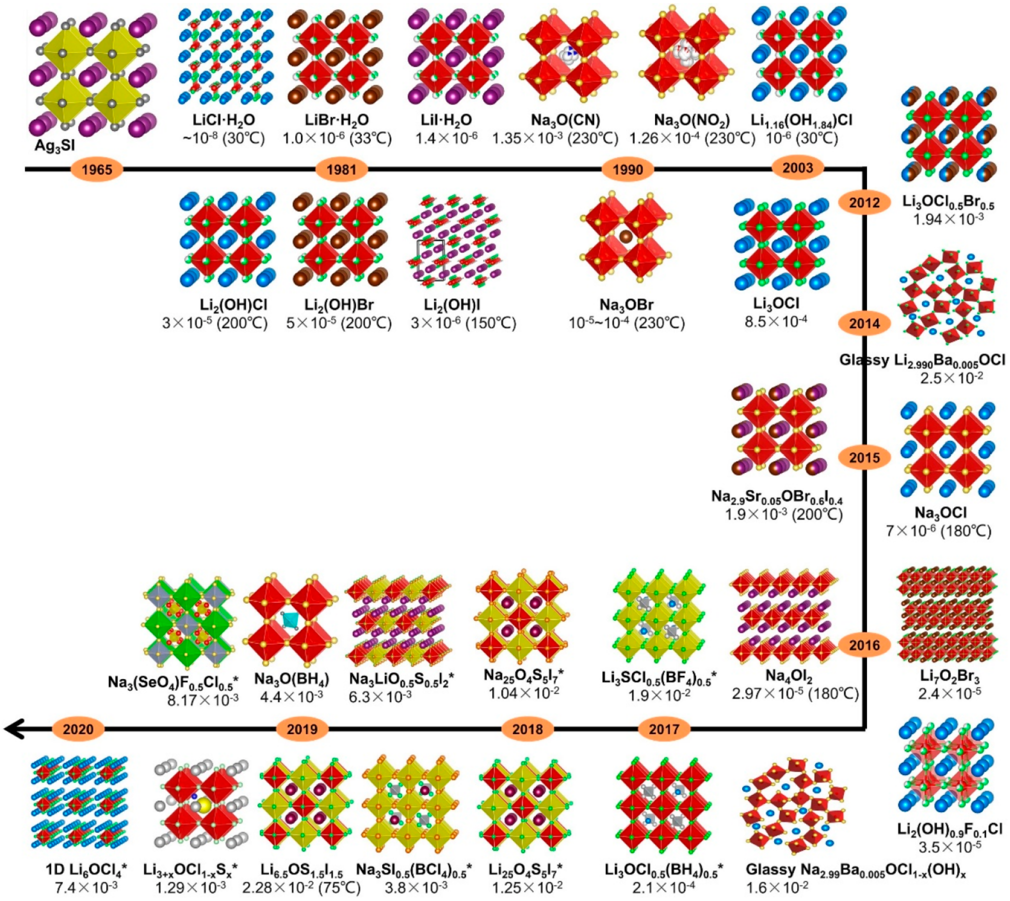

Figure 5. Development of Li^+/Na^+ conducing antiperovskite electrolytes versus year. The room-temperature (unless otherwise noted) ionic conductivities are listed (unit: S/cm). * represents results from simulation. Ag^+ conducting Ag_3SI antiperovskite is listed to show the origin of ionic conducting antiperovskite study.

differences between antiperovskite and perovskite, particularly the advantages of antiperovskite over perovskite structures for SSE applications. On the one hand, the electronic structure of the perovskites and antiperovskites are related to the different ions. X-site anions and B-site cations in normal perovskite structures dominate the contributions at the valence band (VB) region and conduction band (CB) edges, respectively. However, the contributions are inverted in antiperovskite structures with X-site cation contribution in the CB region and B/A-site anion contribution in the VB region, therefore leading to the inverted band structure.[89] This change may introduce significantly different physical properties, such as electrical conductivity, optical absorption/emission and magnetism, since they are determined by the characteristics of electronic structures.

On the other hand, from the viewpoint of structure design, a divalent anion is generally larger than a monovalent anion from the same period (e.g., $O^{2-} > F^-$) and should be more suitable for the A-site in ionic antiperovskites. However, a competing situation may arise considering that the B-site can offer a closer proximity to cations and thus be favorable for the divalent anion because of the stronger Coulombic attraction. Therefore, an inverse anion arrangement on A- and B-sites in addition to the normal pattern can be anticipated in antiperovskite systems. In fact, a number of natural-occurring and synthetic antiperovskite compounds have been identified with such inverse structure, such as Na_3FSO_4, K_3FSO_4, $Na_6FCl(SO_4)_2$, and Na_2CaFPO_4 minerals,[90] and synthetic $Ba_3Br(FeS_4)$[75] and Cs_3ZnBr_5.[74] In contrast to antiperovskites, ionic perovskites show much less cases with the inverse structure as the effects from both sides contribute to the same, regular ion arrangement on A- and B-sites (cation arrangement in this case). Cations with higher charge may enter the A-site of a perovskite when it is significantly larger than the other type of cation (other geometric descriptors, like tolerance factor, should also be considered), but it was only observed in very limited cases such as $BaLiF_3$.[91] The additional ion arrangement choice in antiperovskite structure is a potential advantage in designing new electrolyte materials by providing more opportunities to modify both A-site and B-site so as to improve the ionic conductivity or moisture stability, which will be discussed later.

Moreover, Li^+ (or Na^+) cations in perovskite structures are located in either A-sites or B-sites, for example A-site Li^+ in LLTO and B-site Li^+ in $BaLiF_3$. The concentration of Li^+ in perovskite structures is usually restricted to a maximum 20 at% as in $BaLiF_3$, where Li^+ cations are not mobile in this case.[91] The Li^+ concentration is even lower in the Li-conducting LLTO perovskite as a large portion of A-sites are occupied by La^{3+} cations to maintain its overall structural stability. In contrast to perovskites, the X_3BA antiperovskite structure can provide an extraordinarily high Li^+ concentration (e.g., 60 at% of Li in the prototypical antiperovskite Li_3OCl).[11] This unique structural property may promote a large concentration of vacancies through appropriate defect engineering, and potentially contribute an unusual ionic conductivity as a result. In addition, the high-Li content in antiperovskite also helps to alleviate the

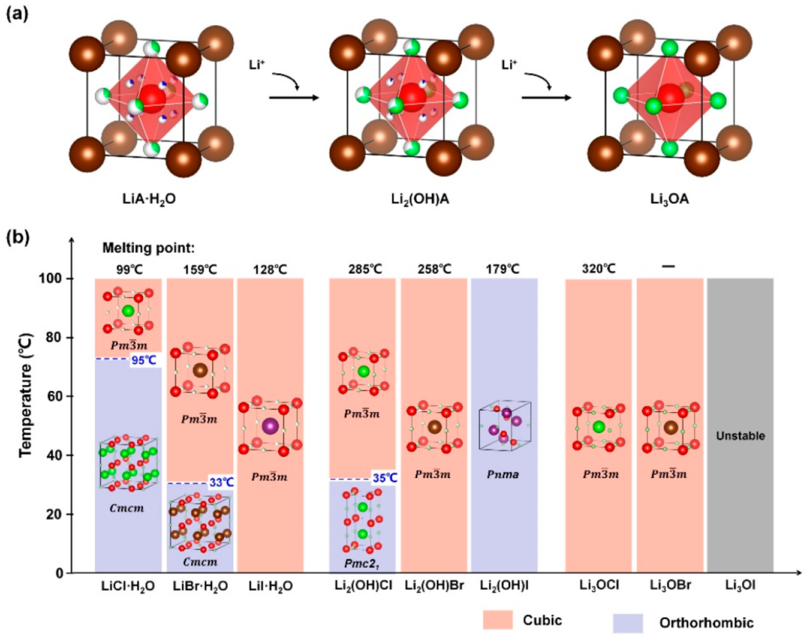

Figure 6. (a) Schematic illustration of the connection among the LiA·H_2O, $Li_2(OH)A$, and Li_3OA series electrolytes. The brown, red, green, and blue spheres represent halide (A^-), oxygen (O^{2-}), lithium (Li^+) and proton (H^+) ions, respectively. The incomplete green and blue spheres in the simplified LiA·H_2O and $Li_2(OH)A$ structure models represent partial occupation. The OH groups in LiA·H_2O and $Li_2(OH)A$ are in rotational disorder as will be discussed in detail in Section 5.1. (b) Schematic illustration of LiCl·H_2O, LiBr·H_2O, LiI·H_2O, $Li_2(OH)Cl$, $Li_2(OH)Br$, $Li_2(OH)Cl$, Li_3OCl, Li_3OBr, and Li_3OI crystal structures at various temperatures.

reduction and density problems caused by the existence of the high-valency metals in conventional perovskite electrolytes.

Last but not least, the generally lower charges of A, B, and X ions in antiperovskites lead to the lower crystal lattice energy as compared with that of perovskites. The charge states of A^-, B^-, and X^- ions in typical antiperovskites are −1, −2, and +1, respectively, which, however, correspond to +2, +4, and −2 in typical perovskites (i.e., oxide perovskites; halide perovskites are not included here due to the lack of Li^+/Na^+ conducting phase). According to the Kapustinskii equation that has been developed by Kapusinskii and generalized by Glasser, the lattice energy of crystalline antiperovskite is approximately four times smaller than that in perovskite.[92] Therefore, antiperovskites usually have much lower melting points (e.g., 320 °C for Li_3OCl and 2000 °C for $CaTiO_3$). As mentioned above, this extraordinarily low melting points in antiperovskite electrolytes will provide a direct route to prepare large-area, dense electrolyte films for practical large-size solid-state batteries. Similarly, the vacancy formation energy is also lower in antiperovskite structures compared with that in perovskite (e.g., 0.93 for the Schottky vacancy $V_{\mathrm{Li}}' - V_{\mathrm{Cl}}^{\bullet}$ in antiperovskite Li_3OCl[93] in contrast with the value of 2−3 eV in $CaTiO_3$[94]), suggesting that it is easier to form Schottky vacancy in antiperovskite structures which contribute to a potentially higher ionic conductivity in antiperovskite structures.

3. ION-CONDUCTING ANTIPEROVSKITE STRUCTURES: HISTORY AND STATUS

The development of Li/Na conducting antiperovskite structures is reviewed in this section. As shown in Figure 5, the investigation of ionic conducting X_3BA antiperovskites can date back to as early as 1960s when Reuter et al. reported the Ag_3SI compound as an Ag^+ conductor.[95−97] It was not until 1990s that the first Na^+ conducting antiperovskite structure with the standard X_3BA stoichiometry was reported by Müller et al.[98] The obtained Na_3OBr was investigated as a high-temperature Na^+ conductor, which gave an ionic conductivity in the order of 10^{-5} to 10^{-4} S/cm at a high temperature of 230 °C. In 2012, the first Li^+ conducting X_3BA-type antiperovskite (i.e., Li_3OCl) was designed and synthesized by Zhao et al.,[11] and employed as a room-temperature Li^+ conductor due to the excellent Li^+ conduction at ambient condition. The proposal of the new electrolyte was based on a long-year research experience on $NaMgF_3$ mineral, which has been also known for the superionic conductivity (of F^- anion) at elevated temperatures. Therefore, the "electronically-inverted" antiperovskite Li_3OCl (or $ClOLi_3$) was designed considering that it might allow Li^+ superionic conduction by mimicking F^- conduction in $NaMgF_3$. The obtained Li_3OCl and a modified form of $Li_3OCl_{0.5}Br_{0.5}$ showed ionic conductivities of 0.85×10^3 and 1.94×10^3 S/cm, respectively, and reached superionic conducting of $\sigma > 10^{-2}$ S/cm as temperature exceeds 250 °C. The successful demonstration of Li_3OA electrolyte as room-temperature ionic conductors verified the effectiveness and practicability of X_3BA antiperovskite structure for ionic conduction, which have stimulated extensive research efforts with much success on this topic.

Before the first report of classic Li_3OA antiperovskites, a series of Li_3OA analogues had been studied as Li^+ conductors, which were the $Li_{3\text{-}n}(OH_n)A$ (n < 3; A = Cl, Br, I) compounds. Lithium halide hydrates (LiA·H_2O, or $Li(OH_2)A$) are a representative of the $Li_{3\text{-}n}(OH_n)A$ series. As shown in Figure 6a, LiA·H_2O compounds possess a nearly identical structure to the standard Li_3OA antiperovskite, with just minor change on Li occupation and additional hydrogen bonded to oxygen. In the LiA·H_2O only one-third of the 3d positions (corresponding to the A-sites in standard X_3BA antiperovskite) are occupied by Li^+, while the positions are fully occupied in Li_3OA. Therefore, the cubic LiA·H_2O can be viewed as a protonated Li_3OA antiperovskite, and a Li-conducting property can be anticipated in view of the 67% of

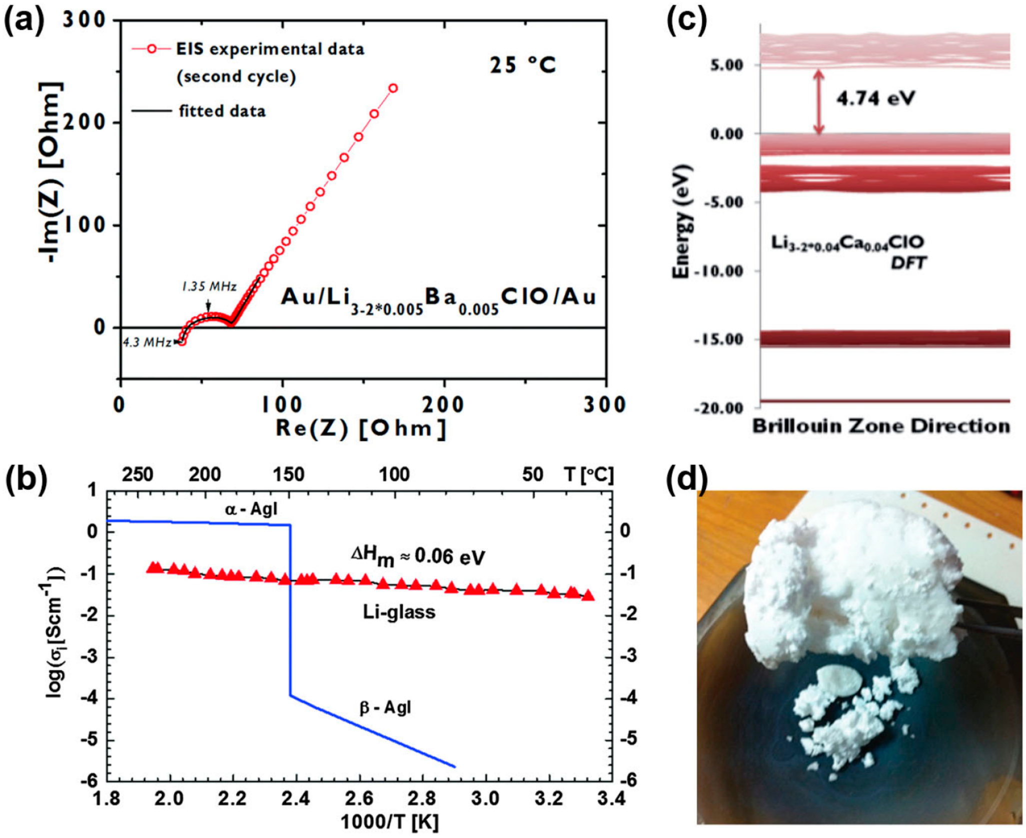

Figure 7. (a) Nyquist impedance and corresponding fitting curve for the glassy $Li_{2.99}Ba_{0.005}OCl$ at 25 °C. The surface area and thickness of the sample are 1.76 cm^2 and 0.2 cm, respectively. (b) Arrhenius plot of the ionic conductivity of the glass electrolyte in comparison with that of AgI. (c) Calculated electronic band structure for the glassy $Li_{2.92}Ca_{0.04}OCl$ electrolyte. (d) Photograph of the as-prepared glass electrolyte. (a) and (c) are reproduced with permission from ref 13. Copyright 2014 The Royal Society of Chemistry. (b) and (d) are reproduced with permission from ref 106. Copyright 2016 The Royal Society of Chemistry.

structural Li vacancies. The diffusion behavior of Li^+ in $LiA{\cdot}H_2O$ was observed with the cubic $LiI{\cdot}H_2O$ in 1965 based on the nuclear magnetic resonance (NMR) resonance of lithium. It was found that Li^+ diffused among the face-center positions with an activation energy of 13.5 kcal/mol.[99] More than 15 years later, the ionic conductivity of $LiI{\cdot}H_2O$ was given quantitatively through impedance measurement, showing a value of 1.4×10^{-6} S/cm at room temperature and 1.1×10^{-3} S/cm at 100 °C (in deuterated sample).[100,101] It is interesting that the higher conducting cubic phase is not retained in $LiCl{\cdot}H_2O$ and $LiBr{\cdot}H_2O$ at room temperature; instead, it is replaced by a low-conducing orthorhombic phase, resulting in poor ionic conductivities (in the order of 10^{-8} S/cm[39]). However, the ionic conductivity of $LiBr{\cdot}H_2O$ would suddenly increase to 2 orders of magnitude higher when temperature exceeds 33 °C because of the first order transition from orthorhombic symmetry to cubic symmetry.[102] Although great efforts been devoted to improving the ionic conductivity of these antiperovskite structures, for example the addition of inorganic particles (e.g., Al_2O_3, SiO_2),[103] the challenge of generally low conductivities at room temperature still exist. Moreover, these compounds have been identified as unstable in contact with lithium metal,[102] which further hinders their application in solid-state lithium metal batteries. Therefore, less attention has been paid to the antiperovskite $LiA{\cdot}H_2O$ electrolytes.

Lithium halide hydroxides, $Li_2(OH)A$, are another representative of $Li_{3-n}(OH_n)A$ antiperovskite series, which have been synthesized from the LiOH-LiA binary molten salts and studied as SSEs during the same period of time as $LiA{\cdot}H_2O$ development. Two thirds of the Li positions in $Li_2(OH)A$ are occupied, leading to a higher Li concentration than that in $LiA{\cdot}H_2O$, while 33% of structural Li vacancies are maintained in $Li_2(OH)A$. It is interesting that the first-order phase transition observed in $LiA{\cdot}H_2O$ also exists in $Li_2(OH)A$ series (Figure 6b). However, the transition proceeds at a much lower temperature in $Li_2(OH)A$, for example, at only 35 °C for $Li_2(OH)Cl$ (95 °C for the $LiCl{\cdot}H_2O$ counterpart). The critical phase transition temperature has not been reported in $Li_2(OH)Br$, probably due to the extremely low value as the cubic phase still exist in $Li_2(OH)Br$ even down to −50 °C. $Li_2(OH)I$, on the contrary, has a high transition temperature and shows only orthorhombic symmetry over the temperature range of interest. Therefore, only $Li_2(OH)Br$ antiperovskite possesses the high conducting cubic phase at room temperature and shows the highest ionic conductivity in $Li_2(OH)A$ (10^{-6} S/cm).[104] $Li_2(OH)Cl$ can give a notably high ionic conductivity of 10^{-4} S/cm at 50 °C (cubic phase), but is as low as $<10^{-8}$ S/cm at room temperature (orthorhombic phase).[39] It is noteworthy that an intermediate tetragonal phase might exist between the cubic high-temperature phase and orthorhombic low-temperature phase;[105] however, the lattice parameters of the tetragonal phase (a = 3.91 Å, b = 3.91 Å, c = 3.92 Å) are very close to that of the cubic phase where a, b, and c are equal. This phase is not discussed here for clarity.

Given the high ionic conductivity displayed by the cubic $Li_2(OH)Cl$ antiperovskites above the transition temperatures, it has become a research focus to suppress the phase transition into noncubic phases so as to maintain the high conductivity at low temperatures. The generally lower phase transition temperature in $Li_2(OH)A$ compared to that in the $LiA{\cdot}H_2O$ series indicates the influence from proton content and suggests the need for a modification route based on deprotonation or lithiation. Metallic Li and butyllithium are common deprotonation reagents. By using these reagents, a series of antiperovskite compounds with noninteger H numbers in the chemical formula have been prepared, including $Li_{2.17}(OH_{0.83})Cl$, $Li_{1.16}(OH_{1.84})Cl$ and $Li_{1.04}(OH_{1.96})Br$. These deprotonated sample demonstrated significantly decreased critical phase transition temperatures compared to the corresponding starting antiperovskites with integer H numbers. For example, the critical temperature for cubic to the noncubic phase transition in $Li_2(OH)Cl$ is decreased from 35 °C to −60 °C for the deprotonated form of $Li_{2.17}(OH_{0.83})Cl$.[39] B-site substitution (i.e., to remove O and H together) provides another option to suppress the phase transition in $Li_2(OH)A$ series, which is easier to perform than the chemical deprotonation route and thus beneficial for large-scale production. By partially replacing the OH^- with F^- ions, the orthorhombic $Li_2(OH)Cl$ was successfully transformed into a room-temperature cubic phase which could provide a faster ionic conduction.[104] It should be noted that these deprotonation processes are accompanied by reduced Li vacancies. A balance must be found in order to maximize the ionic conductivity at room temperature, which could be an interesting topic for future antiperovskite electrolyte research.

Conclusively, $Li_2(OH)A$ electrolytes are of considerable research interest nowadays due to their easy synthesis, reasonable ionic conductivities as well as the low electronic conductivities (2 orders of magnitude lower than the $LiA{\cdot}H_2O$ counterpart). Moreover, $Li_2(OH)A$ antiperovskites have intrinsic Li vacancies that do not exist in perfect Li_3OA antiperovskites. The ionic conductivity of the $Li_2(OH)A$ series has been increased to 3.5×10^{-5} S/cm at 25 °C and 1.9×10^{-3} S/cm at 100 °C with the development of $Li_2(OH)_{0.9}F_{0.1}Cl$.[104] Although there is still a gap between the present conductivity and the requirement for solid-state battery application, it is believed that $Li_2(OH)A$ antiperovskite electrolytes with faster ionic conduction will be synthesized via structure engineering and composition optimization, as the intrinsic structural features are beneficial for doing so while the present attempts are far less than that for conventional electrolytes investigation.

It should be noted that the perfect X_3BA antiperovskite structures might be recognized as a disadvantage for ionic conduction as they do not have intrinsic defects that are the charge carriers in ionic conduction. This point has been demonstrated by Zhao et al. in their original work in 2012 as the Li_3OCl product was actually prepared as a LiCl-depleted form. They also proposed several methods for defect engineering in antiperovskite electrolytes, such as mixing, doping and depletion.[11] Braga et al. later reported a series of divalent-cation-doped Li_3OCl antiperovskites ($Li_{3-2x}M_xOCl$, M = Mg, Ca, Sr or Ba), which, if prepared in a glassy form, could afford a record-breaking ionic conductivity at that time (2.5×10^{-2} S/cm at 25 °C and 2.4×10^{-1} S/cm at 100 °C for $Li_{2.99}Ba_{0.005}OCl$ sample) (Figure 7a).[13,106] It was suggested that the open structure of glassy sample facilitated ionic hopping and contributed to the high conductivity. It is a remarkable fact that the glassy samples could be prepared into dense films without grain boundaries and pores. This might also contribute to the high conductivity of the electrolyte films. It was also suggested that the divalent cation doping could create vacancies and lower the activation energy for Li^+ diffusion. These modifications lead to the much lower activation energy of the glassy samples (e.g., 0.06 eV of $Li_{2.99}Ba_{0.005}OCl$ compared with 0.49 eV of Li_3OCl, Figure 7b). Moreover, the calculated electronic band structure of the glassy sample showed a large band gap of 4.74 eV (Figure 7c), indicating a wide range of electrochemical stability. The electronic conductivity of the glassy sample reached 1.05×10^{-8} S/cm, which is lower than that of the representative LLZO electrolyte (5.5×10^{-8} S/cm). The lower electronic conductivity is highly desired and believed to be beneficial for dendrite-free Li plating.[107] Following the idea of glassy electrolyte, Braga et al. prepared a series of doped Li- and Na-based glassy analogues and employed them in Li−Li symmetric cells and full cells with both demonstrating amazing performances.[16,106,108]

The research on Li/Na antiperovskite electrolytes has also been extended to structural modification other than composition manipulation, which is marked by the development of layered antiperovskite electrolytes, such as $Li_7O_2Br_3$ and Na_4OI_2.[86,87] These phases correspond to the RP phases (general formula $A_{n+1}B_nX_{3n+1}$) showed in Figure 4d. The structure of $Li_7O_2Br_3$ can be understood by stacking two layers of corn-connected Li_3OCl slabs and one layer of LiCl in succession.[109] The existence of the layered $Li_7O_2Br_3$ phase in a major Li_3OBr phase was found beneficial for ionic conduction. With more layered phases formed in the Li_3OBr, the composite was identified with higher conductivity and lower activation energy. The maximum weight percentage of $Li_7O_2Br_3$ phase in the composite was achieved at 44%, which corresponded to a room-temperature ionic conductivity of 2.4×10^{-5} S/cm and activation energy of 0.4 eV. The conductivity was more than 20 times higher than that of Li_3OBr alone (10^{-6} S/cm), while the activation energy was reduced by close to half (0.7 eV for Li_3OBr).[86] The mechanism for the enhanced ionic conduction was attributed to Li_2O depletion in layered structure. The RP phase antiperovskite structure $A_{n+1}B_nX_{3n+1}$ is usually treated as an AX-doped structure from cubic antiperovskite ABX_3. However, Zhu et al. suggested another description, a BX_2-depleted structure from the ABX_3, that is, depleting one Li_2O layer in every three Li_6O octahedral layers.[86] From this viewpoint, the layered antiperovskite structure is a deficient Li_3OBr structure with sufficient Li and O deficiencies, which may explain the higher ionic conduction compared with the “defect-free” Li_3OBr. It will be more interesting if pure phase layered structure is prepared, which, however, has not been reported. Very recently, Lu et al. also suggested the low-dimensional antiperovskite structures for ionic conduction from a viewpoint of simulation.[110] They constructed a series of Li−O−Cl antiperovskite models with various dimensions including 3-D X_3BA, 2-D X_4BA_2, one-dimensional (1-D) Li_6BA_4 and 0-D X_5BA_3 (X = Li, Na, K, Rb; B = O, S, Se, Te; and A = F, Cl, Br, I), and studied the Li diffusion within these models via first-principles computations. They revealed a trend of lower Li migration barriers as the dimensionality decreases, which was attributed to the smaller bottlenecks and the softening of octahedral rotation modes in antiperovskite structures with lower dimensions. Among these models, the 1-D Li_6OCl_4 and Li_6OBr_4 were predicted to have an Li ionic conductivity above 10^{-3} S/cm and meanwhile possess small energy above the hull (i.e., small decomposition energy to form stable phases). The computed ionic conductivity and activation energy of the 1-D Li_6OCl_4 even reached 7.4×10^{-3} S/cm and 0.172 eV,

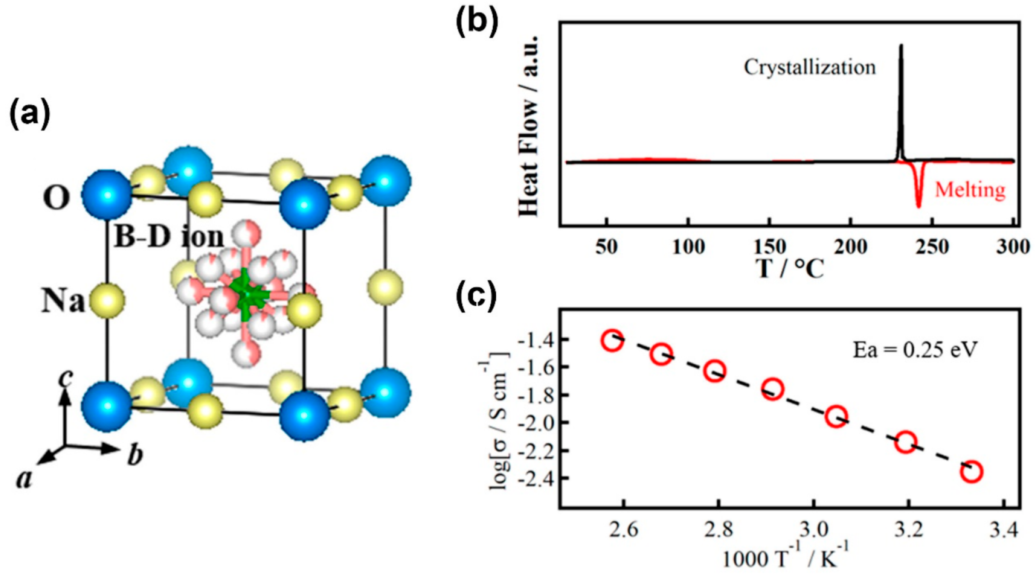

Figure 8. (a) Schematic illustration of $Na_3O(BH_4)$ structure. (b) DSC curse for $Na_3O(BH_4)$. (c) Temperature dependence of the conductivity of $Na_3O(BH_4)$. Reproduced with permission from ref 14. Copyright 2019 American Chemical Society.

respectively.[110] The corresponding band gap was calculated to be as high as 4.3 eV, indicating an intrinsic electrical insulation and a potential wide electrochemical stability window. The investigation of diverse low-dimension antiperovskite structures provides a new direction for optimizing antiperovskite electrolytes, which will be very interesting from a structural point of view. Meanwhile, the properties demonstrated by these new structures are quite attractive for a practical application in full cells. However, these structures, even if theoretically available, are highly likely in metastable phases due to the relatively weak intramolecular bonding, like the case in synthetic $Li_7O_2Br_3$. It can be predicted that corresponding material synthesis will be very challenging. We surmise that possible solutions may lie in the kinetic control (e.g., by quenching) or stabilization from element doping, which will be discussed later.

Structure modification of Li/Na antiperovskite electrolytes has also been performed with the introduction of large polyatomic units to replace the single ions on crystallographic sites. In 2017, Fang et al., based on a computational simulation, proposed a new Li antiperovskite structure composed of BH_4^- polyatomic ions on the A-sites (i.e., $Li_3O(BH_4)$). BH_4^- is composed of four hydrogen atoms and one boron center tetrahedrally bonded by the hydrogen atoms, and has a very similar ionic radius to Br^- (see Table 1). In fact, BH_4^- is one of the well-known "superhalogens", which have been suggested to replace the halogen ions due to the similar chemistry but stronger electron affinity compared with halogens.[111,112] BH_4^- and some other superhalogens have been used to reduce the halogen content in perovskites for high-stability solar cells.[77,113] The introduction of BH_4^- polyatomic ions into Li_3OA antiperovskite electrolytes turned out to be effective in triggering highly desirable properties, including a higher thermodynamic stability, a wider electrochemical stability window and enhanced mechanical properties and a lighter weight in $Li_3O(BH_4)$, while maintaining the high ionic conductivity (1.0×10^{-4} S/cm at room temperature, close to the 1.2×10^{-4} S/cm for simulated Li_3OCl) and low activation energy (0.301 eV, almost identical to the 0.303 eV for Li_3OCl). The room temperature ionic conductivity was improved to 2.1×10^{-4} S/cm when chemical disorder was further introduced into $Li_3O(BH_4)$ by mixing BH_4^- with Cl^-. Later, Fang et al. extended their investigation to a set of A-site cluster ions, including BH_4^-, AlH_4^-, BF_4^-, and BCl_4^-, and revealed several superionic conducting phases with possible higher stability.[24,25] The simulated ionic conductivity of $Li_3S(BF_4)$ reached 1.4×10^{-3} S/cm at room temperature with an activation energy of 0.210 eV. The band gap was also increased to 8.5 eV, compared with the 7.0 eV Li_3OBH_4 and 5.0 eV of Li_3OCl, suggesting a potential wider electrochemical stability window in $Li_3S(BF_4)$. The ionic conduction property was further improved in the $Li_3S(BF_4)_{0.5}Cl_{0.5}$ model, showing an ionic conductivity as high as 1.9×10^{-2} S/cm and an activation energy as low as 0.176 eV. Considering that the absolute conductivity values are usually underestimated in theoretical investigation by, for example, the fixed volume in the MD simulations of these cases, the actual ionic conductivity might be higher, for example above 10^{-1} S/cm for $Li_3S(BF_4)_{0.5}Cl_{0.5}$ as suggested by Fang et al.[24] All the above polyatomic ions were anions with charge number negative one and were designed to partially or fully replace the A-site halogen ions in standard X_3BA antiperovskite electrolytes. Note that this is not necessarily the only choice. In fact, the $Li_2(OH)A$ series mentioned previously could be treated as modified antiperovskite structures from Li_3OA with OH^- group substitutions on the B-sites. Moreover, the original B-site oxygen anions in X_3BA structures could also be replaced by polyatomic ions with charge number negative two, for example, SO_4^{2-} and SeO_4^{2-}.[28] In this case, the large polyatomic ions would move to A-sites while the original halogen ions enter B-sites, leading to the inverse antiperovskite structures. The formulated $Na_3(SeO_4)F_{0.5}Cl_{0.5}$ antiperovskite structure demonstrated a high Na^+ conductivity of 8.167×10^{-3} S/cm at room temperature and low activation energy of 0.137 eV. Furthermore, it showed a consider stability in air and a wide electrochemical stability window (up to 4.215 V versus Na^+/Na).

These simulation results are quite exciting; however, they need to be verified from experiments. Such attempts have been made in 2019 by Sun et al.[14] who reported the influence of introducing BH_4^- and BF_4^- polyatomic ions into X_3BA-type antiperovskite structures from experimental investigation. They failed in synthesizing Li-based antiperovskite with the target

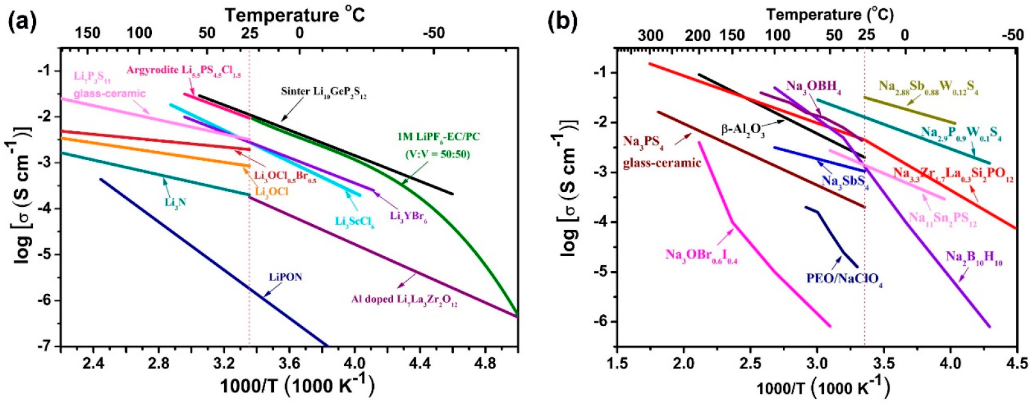

Figure 9. Arrhenius conductivity plots for some representative (a) Li and (b) Na ionic conductors.

polyatomic ions, but successfully prepared a Na-based counterpart, $Na_3O(BH_4)$ (Figure 8a), from the solid-state reaction of Na_2O and $NaBH_4$ mixtures. This new material was identified with antiperovskite structure and exhibited a high ionic conductivity of 4.4×10^{-3} S/cm at room temperature and low activation energy of 0.25 eV, making it among the most promising low-temperature Na^+ conductors. Moreover, it is interesting that the expected phase transition associated with rotation order at low temperatures was also not reflected from both DSC and conductivity tests on $Na_3O(BH_4)$ (Figure 8b,c), which has been usually observed in structures with polyatomic units, such as in $Li_2(OH)Cl$.[39] The synthesis of highly conducting $Na_3O(BH_4)$ might be an important progress in the development of Na^+ antiperovskite electrolytes even though the first polyatomic ion structure has already been reported in $Na_3O(NO_2)$ and $Na_3O(CN)$ electrolytes nearly 30 years ago.[98,114] Before the report of $Na_3O(BH_4)$, ionic conductivities at the close level for crystalline antiperovskite electrolytes were only obtained at very high temperatures (Figure 5). However, the air stability and electrochemical stability window were not reported in this paper, which, we believe, will be a very interesting and important point in future electrolyte research.

Double antiperovskite is another common structural modification to standard X_3BA antiperovskite, as discussed in Section 2.3. Recently, this modification has also been introduced to the development of new antiperovskite electrolytes for enhanced ionic transport. In 2018, Wang et al. formulated a new double antiperovskite structure Li_6OSI_2 based on first-principles simulation.[26] In this structure, the B sublattice is alternatively occupied by O and S (probably in the rock salt pattern shown in Figure 3a, not described in the original work), leading to a face-centered cubic unit cell with $Fm\overline{3}m$ space group instead of the primitive cubic structure with $Pm\overline{3}m$ space group. The simulated Li_6OSI_2 structure was found to be thermodynamically stable, in contrast to the metastable Li_3OCl. It is known that S^{2-} has lower affinity to Li^+ as compared with O^{2-}, and generally contributes to faster Li motion in S-based electrolytes than O-based electrolytes. The simulated Li_6OSI_2 structure also demonstrated lower activation energy for Li^+ diffusion compared with the Li_3OCl counterpart (0.26 and 0.303 eV for Li_6OSI_2 and Li_3OCl, respectively). The activation energy was further decreased to 0.18 eV in an off-stoichiometric form of Li_6OSI_2 (i.e., $Li_{25}O_4S_5I_7$), accompanied with a high ionic conductivity of 1.25×10^{-2} S/cm at room temperature. Na^+ conducting double antiperovskite analogues have also been simulated,[28,61] with the highest room temperature ionic conductivity achieved in a $Li_{25}O_4S_5I_7$ phase (1.04×10^{-2} S/cm). These simulations theoretically demonstrated the effect of S-introduced chemical ordering on improving ionic conduction, which was further verified from experiment results later. In 2019, Xu et al. reported an off-stoichiometric double antiperovskite $Li_{6.5}OS_{1.5}I_{1.5}$ phase that was synthesized from a mixture of Li_2S, Li_2O and LiI.[115] The as-prepared crystalline $Li_{6.5}OS_{1.5}I_{1.5}$ sample exhibited a nearly 2 orders of magnitude enhancement in ionic conductivity as compared with the synthesized Li_3OCl (2.28×10^{-2} and 3.66×10^{-4} S/cm at 75 °C for $Li_{6.5}OS_{1.5}I_{1.5}$ and Li_3OCl, respectively). The activation energy was significantly decreased to 0.48 eV (0.874 eV of Li_3OCl).[115] It is worth noting that the measured ionic conductivity of Li_3OCl in this work was much lower than the value obtained by Zhao et al.,[11] probably due to the influence of severe grain boundary resistance to ionic conduction, which will be discussed in detail.

With the development of these new antiperovskite structures, the Li/Na ionic conductivities of antiperovskite electrolytes have been significantly increased. As shown in Figure 9, some of them give ionic conductivities that are among the best reported data for all kinds of inorganic electrolytes and are comparable to or even superior to that of the liquid electrolytes. It is also noted that the prototype antiperovskite electrolytes Li_3OX show extremely wide band gaps (~6.0 eV) that can be comparable to that of lithium phosphorus oxynitride (LiPON) electrolytes (see Table S1 in the Supporting Information). The wide band gaps were associated with negligible electronic conductivities, which has been regarded as an essential property for SSEs to provide effective ion transport and improve the electrochemical performance by suppressing Li dendrites and interfacial reactions. The high ionic conductivities and low electronic conductivities make antiperovskite electrolytes particularly attractive to the research communities, not to mention other properties, such as the excellent stability toward lithium metal anode, mild synthesis condition, and relatively low prices of the raw materials.

4. SYNTHESIS APPROACHES FOR ANTIPEROVSKITE ELECTROLYTES

Sintering at elevated temperatures and high-energy ball milling are the most frequently used methods for synthesizing inorganic SSEs. These methods are also applicable for most antiperovskite electrolytes. Nevertheless, some conducting phases of antiperovskites are metastable and can be hardly prepared with sufficient purity through the conventional solid-state reactions. Some new methods, such as gas-phase synthesis or high-pressure synthesis, are introduced to prepare desirable new antiperovskite phases. Because of the high reactivity of antiperovskite electrolytes in moist air, the above reactions are performed under inert atmospheres. Recently, a liquid-phase synthesis strategy has raised broad interest due to the mild reaction condition and the simplicity brought for electrode manufacturing. The possibility of liquid-phase synthesis of antiperovskite electrolytes is also discussed.

4.1. Sintering

Typically, antiperovskite electrolytes are prepared by sintering appropriate mixtures of Li (or Na) salts at elevated temperatures (mostly in the range of 300−400 °C). The applied temperatures are significantly lower than that in traditional oxide electrolytes synthesis, which is a potential advantage for antiperovskite electrolytes from the viewpoint of mass production. The prototypical $Li_2(OH)A$ (A = Cl or Br) series electrolytes can be readily prepared from the mixture of dry LiOH and LiA, with a reaction time of less than one hour.[105,116,117] On the other hand, the proton-free counterpart Li_3OA can be hardly prepared without impurity from the mixture of Li_2O and LiA at these temperatures, which is associated with the metastable nature of the Li_3OA structure. It has also been predicted from calculations that the metastable Li_3OA can be stabilized by entropy.[118,119] Annealing the Li_2O and LiA mixtures at higher temperatures for a prolonged period of time can increase the phase purity. However, most of the mixtures still remain unreacted even though they are heated at 500−600 °C.[104] This is largely caused by the sluggish diffusion through the product phase that separate the reactants. The as-formed molten Li_3OA is likely to form a coating layer on the surface of solid Li_2O (melting point 1438 °C[120]), thus separating Li_2O from LiA (melting point: LiCl-610 °C; LiBr-550 °C[121]). The extraordinary reactivity between LiOH and LiA in preparing $Li_2(OH)A$ electrolytes is attributed to the formation of the interesting eutectic systems at low temperatures. For example, the mixture of LiOH and LiBr under a molar ratio of 1:1 melts at only 284 °C, which is significantly lower than the melting point of the constituent salts (477 and 550 °C for LiOH and LiBr, respectively),[122] as shown in Figure 10. Therefore, a homogeneous mixture of the reactants at the molecular level can be provided in this case, which promotes faster reaction kinetics. Moreover, the subsequent cooling process is also important, which affects the phase purity or texture of the final product. A fast cooling rate may help to alleviate the decomposition of metastable phases and are therefore often suggested in the high-temperature synthesis route.[11,117]

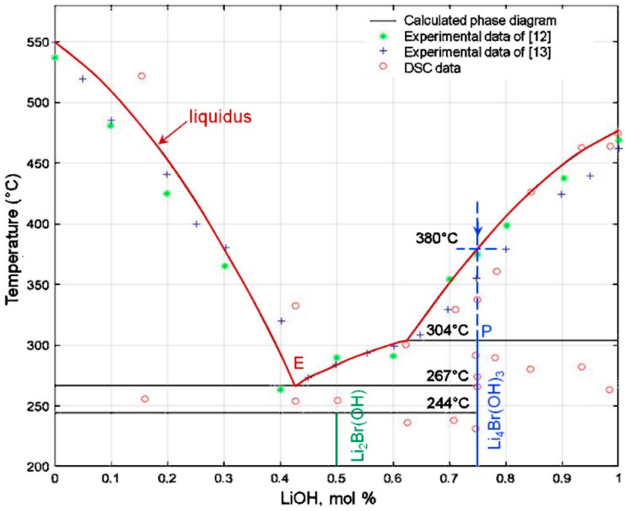

Figure 10. Molten LiOH-LiBr binary system phase diagram. Reproduced with permission from ref 122. Copyright 2019 Elsevier Ltd.

Given the challenge in preparing Li_3OA from dry Li_2O and LiA, an indirect route based on a $Li_2(OH)A$ intermediate might be an alternative method for synthesizing Li_3OA. It has been demonstrated that continuous heating at 330−360 °C and pumping the LiOH-LiCl melt under high vacuum might remove protons (in the form of H_2O) from the system and drive the chemical equilibrium toward the formation of Li_3OCl.[11] However, the removal of H from $Li_2(OH)A$ structures involves the cleavage of covalent O−H bonds that are not easy to break. The reaction conditions including high vacuum and long-time heating adopted in this work are energy- and time-consuming, while the H content in the final product was not given. Alternatively, soft chemical deprotonation might be a more efficient method to remove H from $Li_2(OH)A$. The highly reductive lithium metal is a common deprotonation reagent that readily reacts with $Li_2(OH)A$ through eq 6.[39,123] H atoms can escape from the molten system in the form of hydrogen gas. LiH compound with negatively charged H^- can break the O−H bond more effectively and has been suggested to replace lithium metal in $Li_2(OH)A$ deprotonation via eq 7:[124]

$$Li_2(OH)A + xLi \rightarrow Li_{2+x}(OH_{1-x})A + \frac{x}{2}H_2\uparrow \tag{6}$$

$$Li_2(OH)A + xLiH \rightarrow Li_{2+x}(OH_{1-x})A + xH_2\uparrow \tag{7}$$

$$Li_2(OH)A + xC_4H_9Li \rightarrow Li_{2+x}(OH_{1-x})A + xC_4H_{10}\uparrow \tag{8}$$

To accelerate the conversion process, the reaction involving Li metal or LiH is conducted above the melting point of $Li_2(OH)A$. Butyllithium (*n*-BuLi, C_4H_9Li) is another common deprotonation reagent and could provide wet chemical deprotonation at room temperature. For example, $Li_{2.4}(OH_{0.6})Cl$ and $Li_{1.16}(OH_{1.84})Cl$ were prepared from a suspension of $Li_2(OH)Cl$ and $LiCl{\cdot}H_2O$, respectively, by adding *n*-BuLi in hexane.[39,105] After stirring the reaction solution at room temperature for a period of time, the deprotonated sample was obtained after filtering and drying under mild vacuum. The side product of the reaction is *n*-butane gas (eq 8), which escapes from the system. It is noteworthy that the degree of deprotonation through any of the three routes is associated not only with the ratio of the reactants, but also with the reaction conditions, such as temperature, time and pressure. A thermodynamic limitation may also exist in these reactions. Therefore, the addition of excess deprotonation reagent alone does not guarantee complete removal of proton from $Li_2(OH)$-A, as has been observed in several cases.[105,124] An in-depth investigation on the H-content in the product is desirable.

4.2. Ball-Milling

High-energy ball-milling synthesis has been widely employed as an important complement to the high-temperature sintering route for the synthesis of inorganic SSEs. It induces chemical reactions through the application of mechanical force in the form of collisions between the milling balls and reactants. The merit of this mechanochemical process is that it can overcome the diffusion limitation in solid-state reaction without the need for bulk solvent or high temperature. The reaction process in ball-milling synthesis can be understood as the following steps:[125] when the powder reactants are locally compressed between the milling balls, they undergo plastic deformation, and get flattened, cold-welded, fractured, and rewelded repeatedly. The original crystallographic bonds in the reactants break as a result of the continued mechanical deformation, producing new high-energy surfaces that enable easy welding of neighboring particles and promote the formation of new fine powders. Meanwhile, a variety of defect structures, such as vacancies, interstitials, dislocations, grain boundaries and stacking faults, are also likely to increase in quantity and will affect the ionic conduction in a positive manner, or a negative manner, depending on the type of the electrolytes. The potential reaction during the milling process has been found to be dependent on two aspects.[125] One is the material function, such as the thermodynamic feasibility with negative change in Gibbs free energy change ($\triangle G < 0$), and the structures of the reactants and products, which belong to the intrinsic properties of the materials. The other is the machine function, such as the ball-milling time and intensity. This determines the energy that can be delivered to the reactants and therefore is critical for managing the reaction pathways as well as the yield. Detailed descriptions of the variables of machine function can be found elsewhere.[126,127]

As discussed above, Li_3OX antiperovskite electrolytes can be hardly synthesized from direct sintering Li_2O and LiA mixtures even at relatively high temperatures due to the diffusion limit. This drawback can be mitigated by the high-energy ball-milling treatment. During this process microsize Li_2O and LiA reactants are completely pulverize after the high-energy ball-milling, producing well-mixed powders, which are normally nanosized. Therefore, the contact areas between the reactants are significantly enhanced, which can effectively accelerate the conversion reaction to crystalline Li_3OA in the subsequent annealing treatment. It has been shown that ball-milling of Li_2O and LiBr for 2 h before annealing (ca. 500 °C) allows for the production of pure phase Li_3OBr in a single pass,[124] in sharp contrast to the existence of large amount of unreacted Li_2O and LiBr in the product from sintering alone.[104] In addition to the increased contact area, prenucleation clusters of the final product are also likely to emerge in the ball-milled sample, as has been found in some other inorganic electrolyte systems, such as Li_6PS_5Br sulfide electrolyte and Li_3ErCl_6 halide electrolyte where crystalline samples can be obtained within only 1 min of annealing after ball-milling treatment.[128,129] The proton-rich antiperovskite $Li_2(OH)A$, on the other hand, can be directly synthesized with high purity via ball-milling.[104,130] The lattice constant of the ball-mill synthesized $Li_2(OH)Br$ is 4.046 Å, which matches well with the reported value of 4.046 Å for the annealed sample.[39] The ionic conductivity (ca. 1.1×10^{-6} S/cm at 25 °C) and activation energy (ca. 0.54 eV) of the product are almost identical to that of the sample prepared from sintering alone.[130]

The above similarities between the ball-milled and sintered samples are interesting given the huge difference in the particle size. The ball-milled samples, usually in nanosize, are supposed to have a higher density of grain boundary and therefore a larger grain boundary resistance compared with the microsize sintered product. However, other defect structures, such as Li vacancies or interstitials, may be also produced with increased density in the ball-milled samples, which probably offset the influence from grain boundary to the total ionic conductivity. Very recently, Yamamoto et al. reported an unusual metastable cubic phase of $Li_2(OH)Cl$ antiperovskite ($Pm\overline{3}m$) at room temperature from ball-mill synthesis.[131] It is known that the cubic phase of $Li_2(OH)A$ antiperovskites usually promote faster Li^+/Na^+ motion than other phases with lower symmetry, which is associated with the OH orientational disorder in cubic phase as discussed in Section 5.1. However, the desirable cubic phase normally exists above 35 °C and becomes thermodynamically stable orthorhombic phase ($Pmc2_1$) below 35 °C (Figure 6b). The cubic $Li_2(OH)Cl$ sample was prepared by ball-milling a mixture of LiOH and LiCl at 700 rpm for 72 h, and it gave an ionic conductivity of 2.6×10^{-6} S/cm at room temperature. After heat treatment at 200 °C, the metastable cubic phase decreased in the sample at room temperature, replacing by the dominant orthorhombic phase. As a result, the ionic conductivity decreased by more than 1 order of magnitude (to only 1.4×10^{-7} S/cm). The formation of the metastable cubic phase from ball-milling at the lower temperature than that occurs in common sintering process could be explained by the low crystallinity that would consequently affect the phase behavior.[131] As has been observed elsewhere, materials with nanosized crystallites (<100 nm) possess large surface energy and usually display different phase behaviors from the bulk samples.[132,133] The development of metastable $Li_2(OH)Cl$ by ball-milling directly demonstrates the difference between the ball-milled and sintered samples, and shows the potential of producing unusual or metastable phases by the ball-mill approach. Further investigations on the local structure of the ball-milled antiperovskite samples as well as the structural evolution process are of fundamental importance for the development of new antiperovskite electrolytes from this method.

4.3. Gas-Phase Deposition

Gas-phase synthesis has been widely employed in preparing inorganic SSE membranes for thin-film batteries.[134,135] This method involves the formation of vapor phase of reactants and subsequent nucleation and growth of product on substrates. Homogeneous mixing of the reactants at atomic or molecular level can be achieved in this method, therefore providing an opportunity to break the diffusion limitation in conventional solid-state reactions. Pulsed laser deposition (PLD) is one of the gas-phase deposition techniques, in which the target is ablated by a pulsed laser, forming a plasma containing the target atoms. The advantage of this technique is that the highly focused laser can effectively deliver energy to a localized area and ensure the evaporation of target materials even with a very low vapor pressure, such as some metal oxides. The as-formed plasma is highly energetic (typically 10−100 eV[136]) and is likely to undergo rearrangement on the surface of the substrate. Therefore, it permits chemical reactions between the reactants in addition to the well-known physical transfer process.

By using this method, an antiperovskite electrolyte film with a thickness of 2 μm was prepared from a preformed bulk "Li_3OCl" target (with some hydroxyl radicals).[137] The as-deposited crystalline film gave an ionic conductivity of 8.9×10^{-6} S/cm at room temperature, which was higher than that of the bulk target (5.8×10^{-7} S/cm). The corresponding activation energy was 0.36 eV, which is much lower than the value of 0.59 eV for the bulk target. In another attempt by the same group, a mixture of Li_2O and LiCl raw materials (1:1 molar ratio) was directly used as the target for PLD,[138] making the overall production process more efficient. High-quality Li_3OCl films were readily deposited on different substrates (e.g., Li-coated silicon and stainless steel) using the composite target. The X-ray diffraction (XRD) pattern confirmed the complete conversion from Li_2O and LiCl mixtures to pure phase antiperovskite Li_3OCl, in sharp contrast to the poor conversion in conventional solid-state reaction. Moreover, the ionic conductivity of the as-formed Li_3OCl film was measured to be 2.0×10^{-4} S/cm at room temperature, which is substantially higher than that of the aforementioned film deposited from bulk "Li_3OCl" target (8.9×10^{-6} S/cm). The Li diffusion activation energy of the new film is 0.35 eV, which is almost identical to the value of 0.36 eV reported for the film deposited from the bulk "Li_3OCl" target. It was found that the Li_3OCl film deposited from the raw material mixture possesses larger grain size and higher crystallinity.[138] This may explain the higher ionic conductivity in this sample as the large grain size would reduce the grain boundary resistance which dominates the overall resistance in antiperovskite electrolytes. Conclusively, PLD permits the formation of energetic plasma of the reactant atoms and could facilitate rapid chemical reactions at relatively low temperatures during deposition, therefore affording high-quality antiperovskite electrolyte films on a number of substrates. A modification to the target material is also likely to affect the grain boundary structure and then the ionic conductivity of the deposited films. Other deposition techniques, such as magnetron sputtering (MS), atomic layer deposition (ALD), and vacuum evaporation,[135] can also be useful in the fabrication of antiperovskite electrolyte films.

4.4. High-Pressure Synthesis

Pressure is a fundamental variable that would change the thermodynamic stability of materials, kinetics of chemical reaction, phase transition, and temperature. It is possible to obtain new phases that are at the stability boundary and are quenchable in metastable form to ambient pressure. Moreover, pressure allows direct and precise tuning of the interatomic distance that controls the electronic structure and determines materials properties. It offers a more efficient and cleaner route to optimize materials properties than chemical tuning and temperature tuning.[139] Therefore, the employment of high pressure, usually in the range from a few GPa (1 GPa = 10^4 bar) to hundreds of GPa, in solid-state materials synthesis and characterization has emerged as a useful route both for new material development and for understanding existing ones. The core parameter in this synthetic route is the extraordinarily high pressure, which is generated mostly with the static compression technique by using mechanical devices, such as a diamond anvil cell (DAC), piston cylinder cell (PCC), Bridgman anvil cell, Belt high-pressure device and multianvil cell. These devices allow different upper-limit pressures and sample volumes. More details can be found elsewhere.[140,141]

High-pressure synthesis has been tested as part of the efforts to explore the synthetic routes for metastable antiperovskite phases. For example, Li_3OCl and Li_3OBr phases have been reported as the major products from compressing mixtures of Li_2O and LiCl or LiBr under a cubic anvil apparatus.[142] Specifically, the starting materials were loaded in a cylindrical container of hexagonal boron nitride (BN) with NaCl powder as internal pressure standard. Pressure was transmitted through the medium made of amorphous boron and epoxy resin mixtures, while the temperature was controlled through amorphous carbon as a heating element. It was demonstrated that Li_3OCl was synthesized at a high pressure of 0.5 GPa and a slightly elevated temperature of 152 °C. The temperature is significantly lower than that the simulated critical temperature of 207 °C needed to stabilize the metastable Li_3OCl phase,[119] and even lower than that used for high-temperature synthesis of $Li_2(OH)Cl$ (i.e., 300−400 °C), verifying the contribution of high-pressure to the thermodynamic stability of material and the kinetics of chemical reaction. Li_3OBr was prepared at a harsher condition (3.0 GPa and 186 °C), but the temperature is still at a relatively low level. Investigations on the reaction process by in situ and real-time synchrotron radiation X-ray diffraction (SR-XRD) brought insight into the high-pressure synthesis, which reveals a dehydration mechanism for the formation of Li_3OA compounds under pressure. It was shown that the starting materials (Li_2O and LiCl/LiBr) readily react with atmospheric moisture and produced $Li_3(OH)_2Cl$ and $Li_5(OH)_4Br$ hydrates first. The intermediates would then form the target Li_3OCl and Li_3OBr through the following dehydration reactions at high pressure:[142]

$$Li_3(OH)_2Cl = Li_3OCl + H_2O \tag{9}$$

$$Li_5(OH)_4Br = Li_3OBr + 2LiOH + H_2O \tag{10}$$

The as-formed phases can be quenched to ambient condition for further application. Recently, a new series of hydride-based antiperovskites M_3HCh (M = Li, Na; Ch = S, Se, Te) electrolytes with soft and interexchange anionic sublattices were synthesized via high-pressure solid-state reactions.[143] The starting materials of MH and M_2Ch were mixed, pelletized and inserted into a boron nitride (BN) container. The assemble was loaded into a graphite tube heater and enclosed in a pyrophyllite cube serving as a pressure medium. The device was then pressed at 5 GPa, heated to 700 °C, and kept for 2 h, following by cooling down to room temperature in 5 min and then pressure release. Attempt to synthesize the metastable compounds at ambient pressure (700 °C for 12 h) from the same starting materials was unsuccessful.[143] Therefore, high-pressure tuning provides a valuable tool in the search for new phases that cannot be accessed at ambient conditions. Using a similar method, a new antispinel Li_3OBr phase (space group $Fd\bar{3}m$) was observed as a result of phase transition from antiperovskite Li_3OBr under lower pressures (below 2 GPa) and temperatures below 330 °C.[144] Note that defect-free antiperovskite Li_3OBr is not an ionic conductor; the new phase is there quite interesting due to the existence of intrinsic high-concentration octahedral vacancies that are potentially involved in Li transport and may promote a promising mobility (1.36×10^{-4} S/cm based on simulation).[145] It is unclear whether this phase is quenchable or not due to the lack of experimental evidence, but the enhanced properties exhibited by the high-pressure phase may be reproduced at ambient pressure through chemical tuning. A feasible way is to dope smaller atoms into the host lattice so as to introduce chemical pressure that can mimic the effect of physical pressure.[139]

4.5. Liquid-Phase Synthesis

Liquid-phase synthesis of SSEs has attracted growing interest as it provides a mild reaction condition for producing electrolyte materials. It is generally performed by mixing the starting materials with an appropriate organic solvent in a sealed container at room temperature, followed by removing solvents at a slightly elevated temperature (usually below 300 °C). Similar to the production process of commercial cathode precursors, SSE synthesis from liquid phase can be performed batch by batch, or continuously by pumping in starting

https://doi.org/10.1021/acs.chemrev.1c00594
Chem. Rev. 2022, 122, 3763−3819

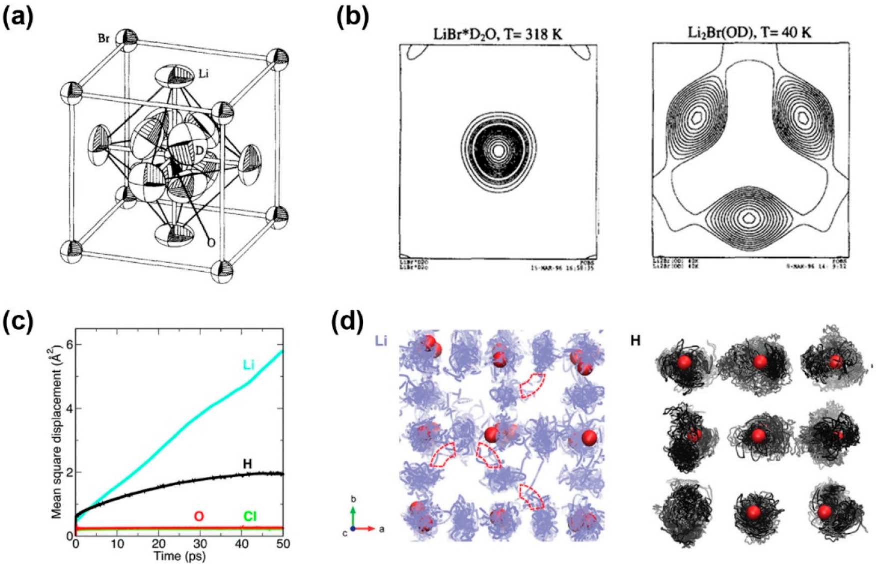

Figure 11. (a) $LiBr\cdot D_2O$ structure at $T = 330$ K based on neutron diffraction. It shows the nonspherical deuteron distribution toward the octahedral faces of Li_6 octahedra. (b) Fourier cut parallel to the octahedral face of a surrounding Li_6 octahedron in cubic $LiBr\cdot D_2O$ and Li_2ODBr. Deuteron distribution in Li_2ODBr is different from that in $LiBr\cdot D_2O$, which points to the edges of the Li_6 octahedron. Reproduced with permission from ref 157. Copyright 1997 Elsevier B.V. (c) Simulated mean square displacement (MSD) plots for Li, H, O and Cl elements in $Li_2(OH)Cl$ at 800 k. (d) Diffusion density maps for Li and H in $Li_2(OH)Cl$ at 800 k. Oxygen positions are represented by red spheres. Chlorine ions are not displayed for clarity. Li-ion hopping is highlighted by red dash line. Reproduced with permission from ref 158. Copyright 2018 The Royal Society of Chemistry.

materials, offering an opportunity for scale-up synthesis. Moreover, liquid-phase synthesis is beneficial for the processing of low-resistive, large-area electrode and electrolyte layers, which has long been a practical challenge for fabricating bulk solid-state batteries. By mixing electrolyte precursor solution with electrode materials, it can form a uniform layer of electrolyte precipitate on the surface of electrode particles, thus creating low-resistive interfaces between the electrode materials and electrolytes in the as-formed electrode layers after a coating and a drying process. Micron-thick electrolyte layers can be directly deposited on the electrodes from the liquid phase, helping to decrease the internal resistance and enhance the energy density simultaneously. It is remarkable that the electrode and electrolyte layer formation processes are compatible with existing battery production lines and processes, which will bring much simplicity and significantly reduce the cost in fabricating practical bulk-type solid-state batteries. Recently, liquid-phase synthesis has been intensively investigated in the study of sulfide-based electrolytes and solid-state batteries, and has demonstrated promising results with respect to the access to a wide range of phases and the high ionic conductivities displayed by these materials.[146−148] Because of the lower temperatures required in the liquid-phase approach compared to that needed for sintering, thermodynamically metastable phases can be readily prepared without the additional fast-cooling step, for instance the metastable β-Li_3PS_4 and $Li_7P_3S_{11}$.[149,150] Moreover, many of the products from liquid-phase approach have displayed comparable ionic conductivities with those synthesized from conventional high-temperature sintering or high-energy ball-milling. The ionic conductivity of the liquid-phase synthesized $Li_7P_3S_{11}$ have reached as high as 1.5×10^{-3} S/cm at room temperature.[151,152]

Despite the fact that some antiperovskite electrolytes can be readily prepared from the low-temperature molten salt systems or ball milling, liquid-phase synthesis of antiperovskite electrolytes is a worthwhile endeavor helping to provide another direction for material scale-up and electrode processing and to introduce potentially different properties. Xu et al. reported the synthesis of Li_6OSI_2 electrolyte using 1,2-dimethoxyethane (DME) as the solvent.[115] Continuous stirring of LiI, Li_2O and Li_2S in DME for a week produced a colorless precursor, followed by filtering and drying in vacuum at 60 °C for 24 h. The precursor was subsequently annealed at 230 °C for 10 h, resulting in the formation of amorphous Li_6OSI_2 electrolyte. This electrolyte displayed an ionic conductivity of 6.15×10^{-3} S/cm at 85 °C, which is close to that of the crystalline antiperovskite Li_6OSI_2 sample synthesized by ball milling (8.82×10^{-3} S/cm). This liquid-phase synthesis approach adopted in this work corresponds to the suspension approach which represents one of the two main groups in liquid-phase synthesis of SSEs. The key in this approach is to form reactant dispersion in organic solvents. DME is a frequently used solvent. Other solvents such as tetrahydrofuran (THF), acetonitrile (ACN), ethyl acetate (EA), dimethyl carbonate (DMC), and ethyl propionate (EP) have also been used for sulfide electrolyte synthesis,[146] and might be useful for tuning the textures and conductivities of antiperovskite electrolytes.

5. IONIC CONDUCTION MECHANISMS AND DEVELOPMENT STRATEGIES FOR ANTIPEROVSKITE ELECTROLYTES

5.1. Ion Dynamics in Antiperovskite Structures

Lithium (or sodium) single-ion conduction is critical for eliminating concentration gradients and the consequent polarization encountered in current liquid electrolyte-based batteries. Most inorganic SSEs have a lithium (or sodium) transference number of close to unity. However, those comprising of small anions or cations besides the alkali ions may give lower transference numbers because of the long-range diffusion of non-Li^+ (Na^+) ions. $Li_2(OH)A$ and $LiA\cdot H_2O$ antiperovskite series possess a large proportion of lattice protons (H^+) in the overall formula; the lattice protons are possible to diffuse within the crystal structure through the Grotthuss (proton hopping) or vehicle (self-diffusion of proton species) mechanisms,[153,154] as has been observed in other inorganic compounds such as $Al(OH)_3$, $Ca(OH)_2$, $Mg(OH)_2$, and many metal−organic frameworks as an important family of inorganic−organic hybrid materials.[155,156] The long-range proton or anion (e.g., O^{2-}, Cl^-) diffusion, if exists in the Li/Na antiperovskite electrolytes, will decrease the effective charge carrier number and probably initiate side reactions with the electrochemically active electrode materials in addition to the aforementioned polarization issue. Therefore, it is necessary to elucidate the mobile species before discussing the ionic conduction mechanisms in antiperovskite electrolytes for Li/Na solid-state battery application.

The mobility of Li^+ (or Na^+) ions in antiperovskite structures has long been recognized. In 1968, Chihara et al. reported the Li^+ diffusion among the face-center positions in $LiI{\cdot}H_2O$ based on the results of X-ray diffraction and ^{7}Li NMR measurements.[99] Proton motion was also detected in $LiI{\cdot}H_2O$ antiperovskite, which manifests as rapid water molecule reorientation at the body-center lattice position under an extremely high rate (>1 MHz). The rotational motion was observed in the high-temperature phase; however, it becomes frozen at low temperature by taking one of 12 equiv orientations. It is interesting that Li^+ diffusion motion was also found to be frozen over the same temperature range as occurs in water rotation,[99] indicating a potential cooperative motion of Li and H. Neutron diffraction results further explain the dynamical orientational disorder of OH^- and H_2O molecules in the H-rich antiperovskites. Deuterated samples, $Li_2(OD)A$ (A = Cl, Br) and $LiBr{\cdot}D_2O$, were prepared for this investigation and displayed a nonspherical deuteron (D) distribution in their high temperature disordered phases (Figure 11a). Specifically, D distribution in $Li_2(OD)Cl$ and $LiBr{\cdot}D_2O$ can be described with split models in which D atoms are oriented toward the octahedral face of the Li_6O octahedra, while the D distribution in disordered phase of $Li_2(OD)Br$ is slightly different and points to the edges of Li_6O octahedra (Figure 11b).[157]

The investigations based on NMR or neutron diffraction suggest that both Li and H are disordered in the HT modifications,[99,157,159] which helps to explain the higher conductivity displayed by the cubic phases. As summarized in Section 3, although lithium halide hydrates and hydroxides have a significant amount of intrinsic Li vacancies, they display little ionic conduction in the noncubic phases with an ionic conductivity lower than that of the proton-free counterparts,[39,102] whereas the high-temperature cubic phases can provide a much higher conductivity. The remarkable difference arises from the orientational disorder of OH^- groups in cubic modifications as they participate in gating Li^+ motion to the neighboring vacant site through the triangular bottleneck (e.g., Cl−O−Cl triangle in Figure 13a). H^+ ions are bonded to the O^{2-} and will hinder Li^+ motion by the coulomb repulsion and steric hindrance once H rotation is frozen.[104,160] OH^- group rotation in high-temperature cubic phases could create accessible Li defects, therefore facilitating Li diffusion.

Although the rotational dynamics of proton has been verified in the H-rich antiperovskites, this does not exclude the possibility of long-range proton motion. The lithium transference number, t_{Li}, in $LiBr{\cdot}H_2O$ antiperovskite has been investigated by constructing a $Li_xTiS_2/LiBr{\cdot}H_2O/Li_xTiS_2$ cell and comparing the transported Li amount in the cell with the total charge passed, which gave a value of 0.9. This high lithium transference number suggests that Li^+ is the dominant mobile species in $LiBr{\cdot}H_2O$ antiperovskite electrolyte.[161] In 2017, a study based on Born−Oppenheimer Molecular Dynamics (BOMD) simulations confirmed the lack of long-range H, O or Cl diffusion in $Li_2(OH)Cl$ for the first time and suggested a nearly 100% contribution from Li diffusion to the total ionic conductivity.[105] This conclusion was further confirmed recently based on a combination of computational simulation and experimental investigation.[158] Ab initio molecular dynamics (AIMD) simulation and solid-state ^{1}H, ^{2}H, and ^{7}Li NMR spectroscopy were employed to track lithium ions and protons motion in $Li_2(OH)Cl$. The mean square displacements (MSD) of all the elements in $Li_2(OH)Cl$ from AIMD simulations shows a linear increase of the Li MSD with time (Figure 11c), indicating a long-range Li-ion motion. In contrast, proton signal reaches a maximum value before the end of the simulation time, demonstrating a localized proton motion that can be ascribed to OH^- group rotation. O and Cl ions are static in the investigated time range. The inhibited long-range proton transport can be attributed to the long interatomic distances between adjacent oxygen ions as the calculated proton MSD is less than 2 Å^2, while the reported O−O distance is 3.91 Å in $Li_2(OH)Cl$.[158] This distance between two neighboring H is too large to form an effective hydrogen-bonding network that is necessary to promote proton conduction (Figure 11d). Considering these multiple aspects, it is safe to exclude the long-range proton motion in the crystalline $Li_2(OH)A$ series.

It should be noted that the mobility of the ions in SSEs is strongly dependent on the local structure. Disruption of the ordered structure in the crystalline antiperovskite electrolytes through amorphization has demonstrated a significant enhancement to the mobility of alkali ions,[13,16] which would be highly desirable if ionic conduction alone is considered. However, the enhancement has been attributed to the expanded volume of the overall phases; this solution might change the mobility of other ions in the material as well. It has been shown that both Li^+ and Cl^- are mobile in the amorphous (or glassy) Li_3OCl model developed from a melt-quench procedure.[162] The conductivity of Li^+ and Cl^- in Li_3OCl glass was found to be 1.19 and 0.23 mS/cm at 27 °C, respectively, while O^{2-} ions displayed negligible mobility. This corresponds to a Li^+ transference number of about 0.83, which, although is relatively high as compared with that of liquid electrolytes, is significantly lower than that of crystalline antiperovskite electrolytes (close to unity).

Conclusively, crystalline antiperovskite electrolytes are single-ion conductors, but some modifications to the original structure (e.g., amorphization) might change the mobility of the ions that are supposed to be "immobile" in the original structure. The multi-ion conduction in electrolytes, if exists, will be detrimental to the full cells implanting these electrolytes by causing concentration polarization, continuous side reaction with the electrode materials or self-decomposition. Further investigation, particularly based on experimental characterizations, is significant for clarifying this point.

5.2. Li^+/Na^+ Conduction Mechanism

Ideal antiperovskites with perfect crystal structures are not ionically conducting. The considerable Li^+/Na^+ conductivities in the aforementioned antiperovskites originate from the existence of high defect concentrations in crystal structures. Vacancies and interstitials have long been recognized as two main types of charge carriers in traditional inorganic electrolytes, which is also applied to the new antiperovskite electrolytes. The mechanisms of Li^+/Na^+ transport in antiperovskite structures via either vacancies or interstitial have been investigated. From a

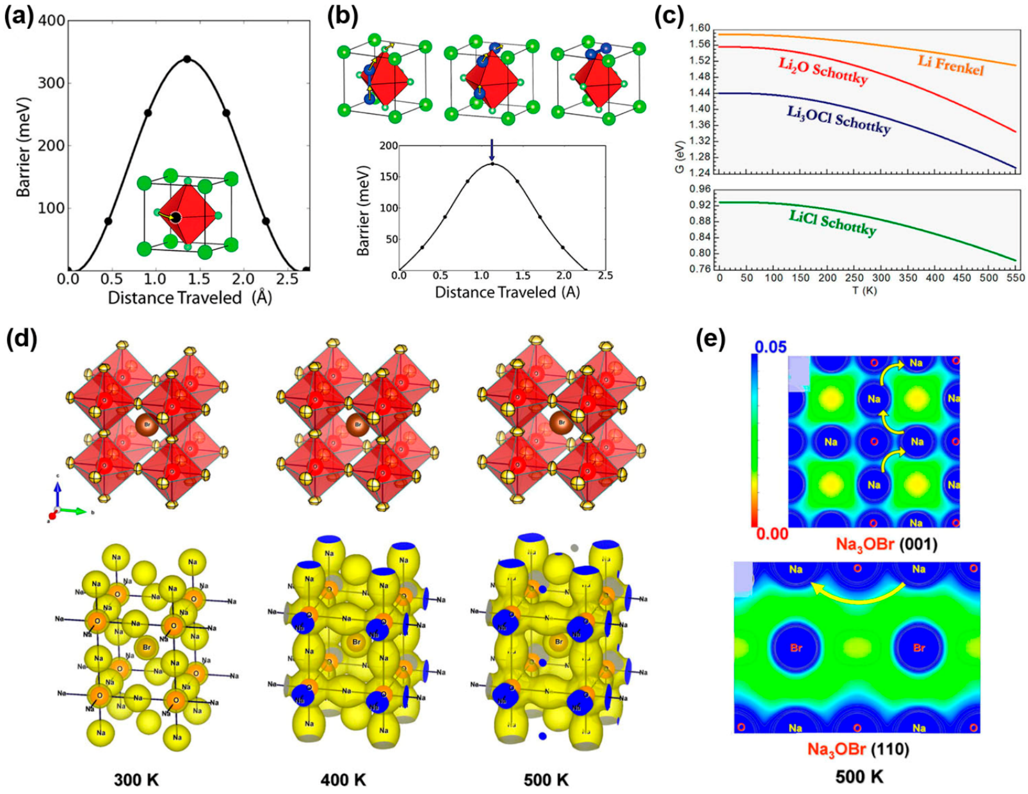

Figure 12. (a) High-barrier Li vacancy migration pathway. (b) Low-barrier Li interstitial migration pathway. Reproduced with permission from ref 163. Copyright 2013 American Chemical Society. (c) Calculated temperature dependence of Gibbs energy (per point defect) in four types of neutral defects containing Li. Reproduced with permission from ref 93. Copyright 2014 American Chemical Society. (d) Upper panel shows the Na_3OBr crystal structures at 300, 400, and 500 K. The thermal ellipsoids are drawn with 80% probability; lower panel shows the nuclear density distributions of Na atoms in Na_3OBr at 300, 400, and 500 K from MEM analysis at the iso-surface level of 0.03 fm/Å^3. (e) 2-D version of the nuclear density distributions of Na_3OBr at 500 K. The yellow arrows indicate the preferable Na^+ transport pathways. Reproduced with permission from ref 87. Copyright 2016 American Chemical Society.

geometrical point of view, vacancy-mediated ion transport would take two independent paths due to the high structural symmetry of X_3BA antiperovskites. One is along the edge of the X_6B octahedra (Figure 12a) and the other is between the vertices of neighboring octahedra. The former path has been identified to be higher probability because of the lower energy barrier.[118] According to AIMD simulations, the Li migration barrier along the edge path was found to be 0.367 eV in Li_3OCl, in contrast to 1.021 eV of the interoctahedra hops. The value is very close to that obtained from Monte Carlo simulations, which is 0.340 eV.[163] However, the calculated energy barrier for vacancy-mediated diffusion pathway is still very high and beyond the experimental result of 0.26 eV for Li_3OCl. A much lower energy barrier has been found with the interstitial migration path in antiperovskite structures. Instead of being individual units like vacancies, the mobile interstitial Li^+ ions have been suggested to adopt a dumbbell configuration with Li^+ ions from the nearest octahedron vertex, while the center of the dumbbell locates at the vertex.[93,163] In the process of Li^+ diffusion, one of the Li^+ in dumbbell pair (or split interstitial) would move to the corresponding vertex of the octahedron while the other Li^+ would then shift to the neighboring Li site and push the original Li^+ on this site off its position by electrostatic repulsion, forming a new dumbbell pair centered at the new vertex (Figure 12b). Therefore, the migration of the interstitial dumbbell involves a coordinated three-atom move, which can be depicted by the multi-ion concerted migration in Figure 1c. The energy barrier of this diffusion path in Li_3OCl has been calculated to be 0.170 eV, nearly half of that in the vacancy hop mechanism,[163] suggesting a potential faster ionic conduction in antiperovskites with reasonably high concentrations of interstitial defects.

Although the simulations have suggested a lower energy barrier in interstitial-mediated ionic diffusion, it does not necessarily mean that the interstitial mechanism is responsible for the observed ionic conduction in antiperovskite electrolytes. It is known that ionic conductivity is directly proportional to not only the carrier mobility but also the carrier concentration. Therefore, it is also necessary to consider the formability of vacancy and interstitial defects in antiperovskite structures. Thermally excited Frenkel defects and Schottky defects (as illustrated in Figure 1d) are the major sources of vacancies and interstitials in pristine Li_3OCl antiperovskite for example, as described as follows:

(a) Li^+ Frenkel:

$$\mathrm{Li}_{\mathrm{Li}}^{\times} \rightarrow V_{\mathrm{Li}}' + \mathrm{Li}_{\mathrm{i}}^{\bullet} \tag{11}$$

(b) LiCl partial Schottky:

$$\mathrm{Li}_{\mathrm{Li}}^{\times} + \mathrm{Cl}_{\mathrm{Cl}}^{\times} \rightarrow V_{\mathrm{Li}}' + V_{\mathrm{Cl}}^{\bullet} + \mathrm{LiCl} \tag{12}$$

(c) Li_2O partial Schottky:

$$2\mathrm{Li}_{\mathrm{Li}}^{\times} + \mathrm{O}_{\mathrm{O}}^{\times} \rightarrow 2V_{\mathrm{Li}}' + V_{\mathrm{O}}^{\bullet\bullet} + \mathrm{Li}_2\mathrm{O} \tag{13}$$

(d) Full Schottky:

$$3\mathrm{Li}_{\mathrm{Li}}^{\times} + \mathrm{O}_{\mathrm{O}}^{\times} + \mathrm{Cl}_{\mathrm{Cl}}^{\times} \rightarrow 3V_{\mathrm{Li}}' + V_{\mathrm{O}}^{\bullet\bullet} + V_{\mathrm{Cl}}^{\bullet} + \mathrm{Li}_3\mathrm{OCl} \tag{14}$$

where defects and perfect sites are noted according to the Kröger-Vink notation.[62] $Li_{Li}^{\times}$ represents a Li^+ ion on the Li crystallographic site, with the superscript × indicating an overall electric neutrality of this site. V_{Li}' represents a vacancy on the Li crystallographic site, which a prime (′) showing the overall one negative charge. $Li_i^{\bullet}$ is an interstitial Li^+ with one positive charge marked by a dot (•). $V_O^{\bullet\bullet}$ is a vacancy on the O crystallographic site with two positive charges. LiCl, Li_2O, and Li_3OCl represent surface molecules on Li_3OCl antiperovskite crystal.

Among these potential defects, Frenkel pairs have been identified with a generally high formation energy. For example, by employing density functional theory (DFT) simulations, Emly et al. gave an estimated formation energy of 1.94 eV for the Frenkel defects in a 6 × 6 × 6 Li_3OCl antiperovskite supercell model.[163] The value was too high and suggested a low degree of formation of thermally generated interstitials in the crystalline structure. This result was further verified by Mouta et al., who calculated the temperature-dependent Gibbs free energies of formation of the four potential Li-containing defects in Li_3OCl antiperovskite.[93] According to their calculation, all the defects demonstrated decreased formation Gibbs energy as temperature increased, while the Li^+ Frenkel defect showed the highest formation energy in the investigated temperature range (0−550 k) and an overall low decreasing rate (Figure 12c), showing that the Li^+ Frenkel defect is less likely to form through thermal excitation alone. In contrast, Schottky defects, particularly the LiCl Schottky, presented lower formation energies, indicating a potentially higher concentration of Schottky defects in Li_3OCl antiperovskite. The calculated concentration of Li^+ vacancies (the ratio of vacancy number to Li_3OCl number in a unit formula) created by LiCl Schottky defect reached 1×10^{-7} before the melting point (277 °C), while the concentration of interstitials associated with Frenkel defects was lower than 1×10^{-13} at the same temperature.[93] Therefore, Li^+ vacancies associated with LiCl Schottky defects have been recognized as the actual charge carriers in most reports despite the higher activation energy than that of Li^+ interstitials. However, the assumption might be challenged by the potential existence of other defects, for example Li^+ interstitials from O misplacement on Cl sites, which formed as follows:

(e) Li_2O solution:

$$Li_2O + Cl_{Cl}^{\times} \rightarrow Li_i^{\bullet} + O_{Cl}' + LiCl \tag{15}$$

In the reports by Emly and Lu et al., this type of Li^+ interstitials was considered in addition to the interstitials from thermal excitation of Frenkel pairs.[163,164] Theoretical simulations in these reports showed that these interstitials were also energetically favorable in antiperovskite with substitutional O on Cl sites, as the formation energy was between that of Li_2O Schottky and Li Frenkel pair. Recently, Mouta et al. revealed a high-concentration Li^+ interstitials in LiCl-deficient Li_3OCl antiperovskite structure as a result of introducing O on the Cl sublattice,[165] contrary to the general idea of dominant Li^+ vacancies in LiCl-deficient Li_3OCl. The number of Li^+ interstitials was calculated to be 200 times larger than the number of Li^+ vacancies in LiCl-deficient Li_3OCl even at LiCl deficiency degree as low as 1%. The ratio of Li^+ interstitials and vacancies numbers reached an astonishing value of 1000 at 20% LiCl deficiency. Therefore, interstitials were recommended as the main charge carrier responsible for the superionic conduction in Li_3OCl and other antiperovskites electrolytes.

It seems that there exists considerable controversy on the major charge carrier in simulated antiperovskite structures. The inconsistence can be understood because different defect configurations were adopted in the simulation investigations. For example, Li vacancies or interstitials were treated as separated charge carriers in some calculations regarding the activation energy; however, they are more likely to be surrounded by the corresponding charge compensating defects, which may exert considerable attraction toward to the mobile species and therefore reduce the mobility. By considering the defect pair interaction (eq 16), Lu et al. reexamined the activation energies ($E_{activation}$) of Frenkel pairs ($V_{Li}'{-}Li_i^{\bullet}$), LiCl Schottky pairs ($V_{Li}'{-}V_{Cl}^{\bullet}$), Li_2O Schottky pairs ($V_{Li}'{-}V_O^{\bullet\bullet}$) and interstitials associated with O misplacement on Cl-sites ($Li_i^{\bullet}{-}O_{Cl}'$), and revealed different situations as shown in Table 2:

$$E_{activation} = E_{barrier} + E_{binding} \tag{16}$$

Table 2. Various Defect Formation Energies, Li Defect Migration Energy Barriers, Binding Energies, and Activation Energies

defect pair	$V_{Li}' - Li_i^{\bullet}$	$V_{Li}' - V_{Cl}^{\bullet}$	$V_{Li}' - V_O^{\bullet\bullet}$	$Li_i^{\bullet} - O_{Cl}'$	ref
formation energy (eV)	2.02	1.41	1.60	1.67	164
migration barrier (eV)	0.170	0.310	0.310	0.147	118, 163
binding energy (eV)		0.145	0.736	0.642	164
activation energy (eV)		0.455	1.046	0.789	164

where $E_{barrier}$ and $E_{binding}$ represent the Li^+ migration energy barrier in the absence of charge compensating defects and the defect binding energy, respectively.

It can be found from Table 2 that although Li^+ interstitials from $Li_i^{\bullet}{-}O_{Cl}'$ pairs have a lower migration energy barrier compared with Li^+ vacancies, the attractive interaction between the defect pairs is quite strong, which eventually leads to a higher overall activation energy. In comparison, Li^+ vacancies from LiCl Schottky pairs possess much lower binding energy with its charge compensating defects and demonstrate the lowest activation energy. From this aspect, vacancy-mediated charge carrier diffusion might be a dominant mechanism responsible for the ionic conduction in antiperovskite electrolytes. The differences in simulated results, on the other hand, have demonstrated the possibility of tuning ionic conduction through minor modifications to the local defect structures in antiperovskite electrolytes. Therefore, the practical ionic conduction mechanism in antiperovskite structures should be analyzed case by case, which would be best complemented by experimental characterizations.

Neutron diffraction has provided an efficient tool to give the atomic positions of all the constitutional elements of electrolytes, including the light O and Li elements that have posed significant challenges for X-ray diffraction characterizations. By conducting temperature-dependent neutron diffraction combined with the maximum entropy method (MEM) analysis, the 3-D Li^+ conduction pathways in the representative $Li_{9.54}Si_{1.74}P_{1.44}S_{11.7}Cl_{0.3}$ electrolyte have been identified, which has helped us to understand the superionic conduction mechanism in the structure.[166] The ionic transport pathways in antiperovskite electrolytes have also been given by employing the same method,[87] as shown in Figure 12d and e. The anisotropic thermal vibration of Na atoms and the nuclei density distributions from MEM analysis indicated a 3-D Na^+ conduction in the Na_3OBr antiperovskite structure, which occurred along the edges of Na_6O octahedra and through the O anions. This work also showed that the nuclear density distributions of Na and Br ions were not overlapped, indicating that Br ions might not be involved in Na^+ transport in Na_3OBr. It is worth noting that ∼1% Na^+ vacancies were identified in Na_3OBr and attributed to the Na_2O Schottky defects, which, however, is different from either XA (i.e., LiCl and NaCl for Li_3OCl and Na_3OCl antiperovskites, respectively) Schottky defects or interstitials as the dominant charge carrier in theoretical investigations. This inconsistency may arise from the environmental complexity during material synthesis. Thermal excitation is the main trigger for defect formation in simulated pristine electrolytes. However, a number of factors, such as deviations from stoichiometry, synthesis approach, temperature, and duration time, might affect the defect formation. The observed Na_2O Schottky defects with much higher concentration than simulations probably result from one or more of the factors, which, if handled well, can be utilized to manipulate defects and promote desirable ionic conduction.

5.3. Modification Strategies for Enhanced Conductivity

On the basis of the experimental and theoretical progress made in antiperovskite electrolytes research and the general ionic conduction mechanisms discussed above, we summarize the existing and potential strategies that can be utilized to promote high ionic conductivities in antiperovskite electrolytes, in hope of providing a useful and general guidance to realize the full potential of antiperovskite structures as a promising platform for advanced SSE research and all-solid-state battery application. The strategies are given below.

5.3.1. Charge Carrier Concentration Optimization. Defects are a prerequisite for ionic conduction in crystalline inorganic electrolytes and the conductivity is proportional to the concentrations of mobile defects. However, pristine antiperovskites are void of defects and often manifested as poor ionic conductors. Although thermal excitation can promote the formation of intrinsic vacancies and interstitials, the corresponding concentrations are generally low at room temperature ($<10^{-15}$) due to the relatively high formation energies.[93,164] Therefore, in order to obtain a high ionic conduction from antiperovskite structures, charge carriers should be introduced deliberately through defect engineering in addition to the thermal effect. Substitution of an aliovalent cation for Li^+/Na^+ is perhaps the most direct route, which has been employed with much success to increase ionic conductions in many other electrolyte systems. Aliovalent substitution has also been performed in constructing advanced antiperovskite electrolytes, with typical divalent cation dopants including Mg^{2+}, Ca^{2+}, Sr^{2+}, and Ba^{2+} or trivalent Al^{3+}. For example, the ionic conductivity of a Na-based antiperovskite electrolyte, $Na_3OBr_{0.6}I_{0.4}$, was enhanced experimentally by a factor of nearly two through a minimum Sr^{2+} doping (∼1.67%) on the Na-sites.[49] Zhang et al. claimed that by doping the same amount of Ca^{2+} into Li_3OCl, the ionic conductivity became more than 1 order of magnitude higher than that of the undoped Li_3OCl.[142] The observed conductivity enhancements by doping are related to the increased vacancy concentrations as introducing one divalent cation on the Na/Li sublattice will create one vacant site in order to maintain charge neutrality. As a result, the mobile vacancy number increases. It has been calculated that the concentration of free vacancies in doped $Li_{2.99}M_{0.005}OCl$ (M = Mg, Ca, or Ba) reached $\sim10^{-7}$ at room temperature just by ∼0.167% dopants of divalent cations,[167] which is much higher than 10^{-15} for thermal excitation alone. Therefore, aliovalent substitution provides an efficient route to introduce vacancies and to increase ionic conductivity.

Vacancy structure can also be introduced by partial depletion in X_3BA antiperovskites through the mechanism described by eqs 12 and 13. As suggested by Zhao et al., XA depletion could effectively introduce empty dodecahedral A-sites and Li vacancies at the octahedral vertices and produce lattice defects for enhanced ionic conduction.[11] They synthesized a series of antiperovskite samples from Li_3OCl with various degrees of Li vacancies through the control of reactants, including $Li_{2.95}OCl_{0.95}$, $Li_{2.90}OCl_{0.90}$, $Li_{2.85}OCl_{0.85}$, and $Li_{2.80}OCl_{0.80}$. They also pointed out the possibility of unintentionally introduced LiCl Schottky defects during the melting synthesis process. The volatile Cl element might have escaped from the crystal lattice in a considerable amount, and the corresponding amount of Li might be reduced concurrently. Following this idea, those synthesized from high-temperature sintering processes were most likely XA deficient structures and probably contained considerable defects. On the other hand, there are few reports on vacancies caused by X_2B depletion in synthetic antiperovskites, probably due to the low mobility that is associated with the strong attractive interaction between V'_{Li} and $V_O^{\bullet\bullet}$ pairs for example.[164] Moreover, the coordinated O atoms are less volatile than Cl. The layered antiperovskites $Li_7O_2Br_3$ (or LiBr-$2Li_3OBr$) and Na_4OI_2 (or NaI−Na_3OI) are the only cases whose structures are close to Li_2O- (or Na_2O-) deficient antiperovskites.[86,87] However, the concentration of X_2B depletion is fixed in these two examples, which is different from the tunable XA depletion in standard XA-deficient antiperovskites.

In addition, increasing interstitial concentration might be another option considering the moderate activation/formation energies of those caused by divalent anion occupation on B-sites (Table 2). Moreover, the extremely low migration energy barrier (0.147 eV) for the interstitials holds the promise of providing faster ionic diffusion kinetics. The high activation energy in the aforementioned Li^+ interstitials is mainly attributed to the high binding energy associated with the strong defect interaction between the $Li_i^\bullet$ and O'_{Cl} pairs. The $Li_i^\bullet$ has been found trapped by the O'_{Cl} defect in an O cube assembled by the substitutional O and eight surrounding O, leading to the formation of an O−Li dimer structure. The O−Li bond in the O−Li dimer has been calculated with even higher covalent nature than the O−Li bonds in a perfect Li_3OCl lattice.[164] Therefore, a lower overall activation energy may be expected if the defect interaction is reduced. This idea can be fulfilled by substituting the charge-compensating O'_{Cl} defect with a "weaker" defect. S'_{Cl} defect might be a promising candidate since S^{2-} has a lower electronegativity compared with O^{2-}, which can contribute to a lower binding energy. Nevertheless, it is worth noting that divalent anions do not necessarily replace the monovalent anions on the A-sites, since S, for example, is actually in the same valence state as O and S substitution of O on B-site has been predicted in Li_3OI.[26] S-substitution on Cl-site must be profitable from the structure stability standpoint before the practical existence, which might be the fact. Actually, S^{2-} are more suitable for the divalent substitutional anions on Cl-site than O^{2-} anions considering the closer ionic radii between S^{2-} and Cl^- (S^{2-}, 184 pm; Cl^-, 181 pm; O^{2-}, 140 pm from Table 1), while charge neutrality can be fulfilled by introducing Li interstitials. The feasibility or preference of S substitution of Cl in Li_3OCl has been confirmed recently from formation energy calculation, which has displayed a low formation energy.[168] Following this idea, it might be also possible to introduce $Li_i^{\bullet}-Se'_{Br}$ pairs in Li_3OBr antiperovskite electrolyte (the ionic radii of Se^{2-} and Br^- are 198 and 196 pm, respectively). The benefit of introducing S to Cl site has been demonstrated by Li et al., who confirmed from simulations that a large amount of Li^+ interstitials were produced under the process and exhibited lower diffusion activation energy than those from $Li_i^{\bullet}-O'_{Cl}$ and $V'_{Li}-V_{Cl}^{\bullet}$ pairs.[168] The synthesis of related structures will thus be of considerable interests considering the above benefits but has yet to be done.

5.3.2. Enlarged Bottleneck and Free Transport Volume.

Charge carrier motion in ionic conductors is restricted by the diffusion bottleneck and free transport volume. The former one is in the form of a triangular bottleneck gate in antiperovskite structures, as shown in Figure 13a. The triangle is composed of one O^{2-} and two nearest Cl^- for example. Li^+ transport from one site to another available site must go through the triangular bottleneck, which can be described by the energy barrier indicated in Figure 1a and c. Therefore, a larger bottleneck space is likely to promote faster ionic conduction. This can be fulfilled by a direct modification to the Li_3O backbone of the antiperovskite structures, for example S substitution on the O-sites, which has been known for its effectiveness and practicability in increasing cell volume and free diffusion space in conventional oxide- and sulfide-based electrolytes. The charge density distributions for the midpath sections along the edge pathway in vacancy-dominant Li_3OCl and Li_3SI antiperovskite electrolytes were simulated and clearly displayed the influence of S substitution on the diffusion bottleneck,[26] as shown in Figure 13b and c. It demonstrates a considerable size difference between the Cl−O−Cl and I−S−I triangular bottlenecks, with S substitution leading to the larger bottlenecks. Moreover, an overlap in the charge densities of Li^+ cations and O^{2-} anions was identified in Li_3OCl sample, indicating that Li^+ migration is strongly affected by O^{2-} anions. In contrast, Li_3OI sample showed little charge overlap in Li^+ and S^{2-} ions, showing that Li^+ motion is less affected by S^{2-} due to the larger bottleneck. Similar charge density distributions were also obtained in the interstitial-dominant Li_3OCl and Li_3SI structures (Figure 13d,e). Generally larger triangular bottlenecks were found in these two samples due to the excessive Li^+ in lattice. The enlarged lengths in Li−I and Li−S further weakened the interactions between them and made it easier for Li^+ diffusion in the Li_3SI, which was confirmed from the diffusion barrier.[26]

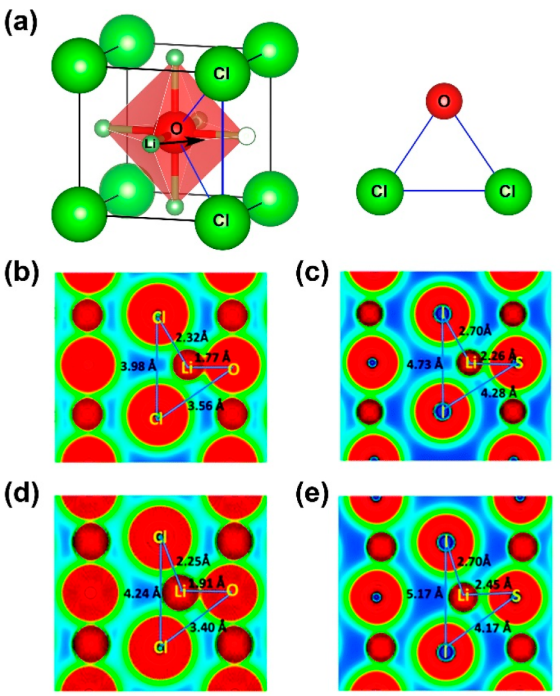

Figure 13. (a) Triangular bottleneck gate in Li_3OCl antiperovskite structure. Charge density distributions for the midpath sections along the edge-pathway in vacancy-dominant (b) Li_3OCl and (c) Li_3SI, and interstitial channel in interstitial-dominant (d) Li_3OCl and (e) Li_3SI. Reproduced with permission from ref 26. Copyright 2018 The Royal Society of Chemistry.

The free transport volume in antiperovskite structures can also be modified through the choice of anions on A-sites considering the structure feature of antiperovskites that are composed of the octahedra backbone and A cations filling the dodecahedra cavity. The free spaces in antiperovskite structures also depend on the size of the fillers once the rigid backbones are fixed. A large anion filler will leave a small free space in the framework. Therefore, a small anion is preferred for A-sites from this consideration, which is different from the choice for B-site anions. However, the practical situation regarding A-site anion choice is more complex, which must consider the overall structure stability of target antiperovskite. As discussed in Section 2.2, the cubic antiperovskite structure will collapse or distorted if the A anions are too small to fill the cavity, also leaving little free space for ion migration. The dilemma might be solved by introducing mixed A sublattice. Partial substitution of the small A anions by larger anions is likely to provide a stabilized structure while maintaining the free space. It has been confirmed by Zhao et al., who found the highest ionic conductivity in the mixed-halide phase $Li_3OCl_{0.5}Br_{0.5}$ in Li_3OA series (A = Cl, Br) instead of in the Li_3OBr and Li_3OCl end-members.[11] Wang et al. also showed the benefit of cation mixing in antiperovskite electrolytes with the Na_3OBr and $Na_3OBr_{0.6}I_{0.4}$ samples. The mixed-cation sample displayed a much lower activation energy than the single-cation sample (0.63 and 0.76 eV for $Na_3OBr_{0.6}I_{0.4}$ and Na_3OBr, respectively).

5.3.3. Introducing New Diffusion Pathway.

The mobilities of charge carriers in antiperovskite electrolytes are largely dependent on the diffusion pathways. Although the existing pathways offer reasonable mobilities while modifications from doping or depletion can further improve ionic conduction, the pathways in pristine antiperovskite structures are restricted to the aforementioned cases, which limits the space for ion transport optimization. It is thus highly interesting to explore the possibility of introducing new diffusion pathways into antiperovskites or their derivatives in order to provide lower energy barriers. Recent progress showed that it could be fulfilled by structural modifications to the pristine antiperovskites, for example the introduction of polyatomic anions and the low-dimension antiperovskite structures.

The polyatomic anions are not new in SSEs. Nearly a century ago, Benrath and Drekopf found an abrupt ionic conductivity increase in lithium sulfate (Li_2SO_4) that possesses tetrahedral SO_4^{2-} anion, which coincided with a monoclinic-to-cubic phase transition at 580 °C.[169] The connection between the increased conductivity and the rotation of the SO_4^{2-} anion was not clear until 1972 when the transport model in α-Li_2SO_4 was

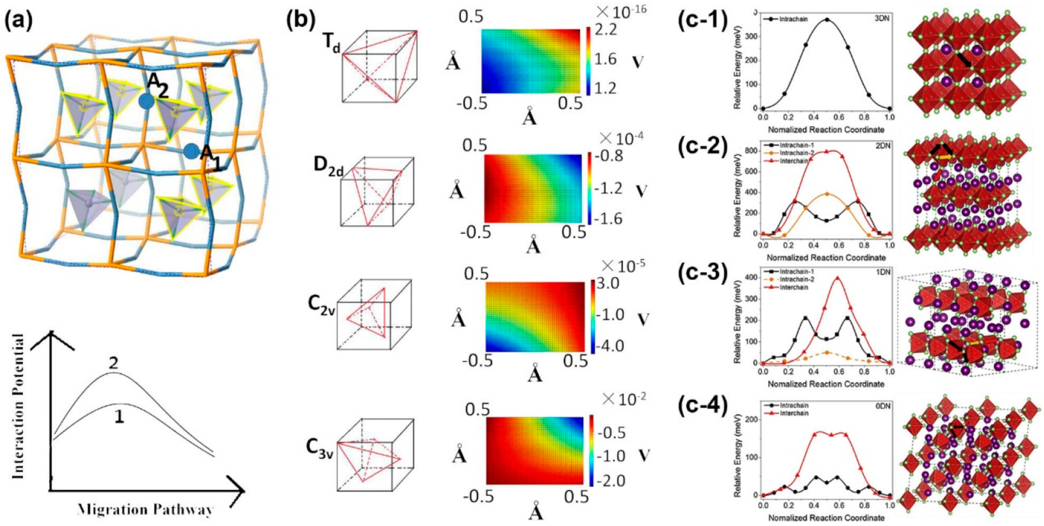

Figure 14. (a) Li_3SBF_4 structure model. The four coordinating BF_4^- anions of A_1-site Li^+ and A_2-site Li^+ are highlighted in yellow. Curve 1 and 2 display two possible potential profiles along the migration pathway caused by BF_4^- rotation. (b) BF_4^- configurations (left panel) with the T_d, D_{2d}, C_{2v} and C_{3v} symmetries. Calculated potential surfaces (right panel) in an area of 1.0 × 1.0 Å^2 around a Li^+ site for different orientational symmetries of the BF_4^- anion. The effect of BF_4^- rotation on the potential surface is shown by the different color. Reproduced with permission from ref 24. Copyright 2017 National Academy of Sciences. (c-1−c-4) Li^+ diffusion pathways (right panel) and corresponding diffusion barriers (left panel) in simulated 3-D Li_3OCl, 2-D Li_4OCl_2, 1-D Li_6OCl_4, and 0-D Li_5OCl_3 antiperovskite structures. Reproduced with permission from ref 110. Copyright 2020 Elsevier B.V.

revealed.[170] Afterward, a similar anion-rotation-promoted diffusion was studied in a number of compounds, such as the lithium sulfate derivatives $LiNaSO_4$ and $LiAgSO_4$,[171] and the air-stable anhydrous Na_3PO_4.[172] Recently, enhanced conductivities were identified in Li, Na, Ca, and Mg borohydrides containing BH_4^-, $B_6H_6^{2-}$, $B_{10}H_{10}^{2-}$, or $B_{12}H_{12}^{2-}$ complex anions and attributed to the anion rotation.[173] More recently, the superior conductivity in prototype glassy $75Li_2S$-$25P_2S_5$ electrolytes was also found to be related to the anion rotation.[174] The contribution of rotational movement of the polyatomic anion to cation conduction has been concluded as a general "paddle-wheel mechanism", where the polyatomic anion "kicks" surrounding cations through its rotation and accelerate cation motion.[175] Polyatomic anions have been deliberately introduced into antiperovskite electrolyte system since 1990 with the report of $Na_3O(NO_2)$ and $Na_3O(CN)$.[98] An enhancement of the ionic conductivity was observed with the introduction of the polyatomic anions. However, the underlying mechanisms for this phenomenon are not fully understood as the improvement in antiperovskite electrolyte system may not follow the "paddle-wheel mechanism". Recently, Fang et al. revealed a new low-energy migration pathway in antiperovskite structures as the result of polyatomic anion rotation.[24,176] It has been shown that the reorientation motion of the polyatomic anions, BF_4^- and BH_4^-, tends to generate a shifting potential surface throughout the Li_3SBF_4 (or Li_3SBH_4) crystal, which facilitates Li^+ diffusion. In Li_3SBF_4 antiperovskite electrolyte, for example, each Li^+ cation is coordinated by four BF_4^- anions (Figure 14a). The interaction potential created by each of the BF_4^- anions on the Li^+ cation can be quantified through the multipole expansion:[24,176]

$$\phi(\vec{r}) = \frac{1}{4\pi\varepsilon_0}\left[\frac{q}{r} + \frac{\vec{p}\cdot\vec{r}}{r^3} + \frac{1}{2}\sum_{ij}\frac{r_ir_j}{r^5}Q_{ij} + \cdots\right] \tag{17}$$

where q is the total charge (-e) of the BF_4^- anion and $\vec{r}$ is the vector from the boron (B) center to the Li^+. $\vec{p}$ represents the dipole moment associated with the charge distribution in BF_4^-, while Q_{ij} represents the quadrupole term, which can be calculated from

$$\vec{p} = \sum_{i=1}^{4} q_i^F\vec{R}_i^F - q\vec{r} = \sum_{i=1}^{4} q_i^F\vec{r}_i^F \tag{18}$$

$$Q_{ij} = \sum_{k=1}^{4} q_k(3R_i^kR_j^k - R^2\delta_{ij}) \tag{19}$$

where q_i^F is the charge on F atom ($-0.25e$), $\vec{R}_i^F$ is the coordinate of F atom, and $\vec{r}_i^F$ represents the relative coordinate of F atom from B center. q_k is the charge on F atom, and R_i^k represents the ith coordinate of the kth F atom.[24,176]

The dipole plus quadrupole terms of the potential can be calculated based on eq 17 with the different orientational symmetries of BF_4^- anion (Figure 14b). From these calculations, the ground state orientation (C_{3v} group) displays the lowest potential among the four distinctive symmetry groups, which is in the order of -10^{-2} V. The potential difference between the ground state and any other group (T_d, D_{2d}, or C_{2v}) will be accordingly large enough to drive Li^+ ion to a high speed of 10^{-2} Å/fs if all the potential energy is converted to the kinetic energy of Li^+. Furthermore, a spatial variation of the potential due to BF_4^- or BH_4^- rotation on different sites has also been identified, demonstrating the capability of constantly delivering kinetic energy to Li^+ vibration and facilitating Li^+ long-range migration.[24,176] As a result, the calculated activation energy is decreased to 0.210 and 0.301 eV in Li_3SBF_4 and Li_3SBH_4, respectively, compared with 0.303 eV in Li_3OCl simulated via the same method. This confirms that the polyatomic anion rotation can unlock lower potential profiles along the diffusion pathway (Figure 14a) and promote faster ionic diffusion in antiperovskite electrolytes with polyatomic anion rotation. Up to now, NO_2^-, CN^-, BH_4^-, and SO_4^{2-} polyatomic anions have been experimentally introduced into antiperovskite electrolytes and successfully promoted faster ionic diffusion.[14,98,114,177,178] We surmise that with the experience from the investigations of other inorganic systems containing polyatomic units, more antiperovskite electrolytes containing new polyatomic anions can be prepared and provide promising ionic conduction properties.

In addition to the polyatomic anions, low-dimensional structures can also introduce desirable new low-energy diffusion pathways. It has been shown that layered antiperovskites, such as $Li_7O_2Br_3$ and Na_4OI_2, possess higher ionic conductivity and lower activation energy as compared with the 3-D antiperovskite counterparts.[86,87] The enhanced ionic conductions were attributed to the increased Li^+ vacancy concentration due to Li_2O depletion in layered structures. In addition to the higher vacancy concentration mechanism, in-depth investigations on the diffusion pathway suggested that low-dimensional antiperovskite might also contribute to the faster ionic diffusion kinetics in a way of providing a new low-energy diffusion pathway.[87,110] There are three potential cation migration pathways in vacancy-dominant layered antiperovskites, in comparison with the single pathway in vacancy-dominant 3-D antiperovskites due to their isotropy, as shown in Figure 14c-1,c-2. The first one is the interlayer (or interchain) jump between separate X_3BA slabs (indicated by the red arrow in Figure 14c-2). This type of cation migration often involves the highest migration energy probably due to the large physical distance (e.g., 1.1 eV in Na_4OI_2 and 0.800 eV in simulated Li_4OCl_2[87,110]). The rest two are both intralayer (or intrachain) jumps within the X_3BA slabs along the octahedral edge. These two pathways arise because of the existence of two types of cations. One has four nearest halide anions and two nearest oxygen anions, which is similar to those in 3-D antiperovskites (noted as X1). The other cation is surrounded by four nearest halide anions and one nearest oxygen anion (noted as X2). The energy barrier of X1−X1 jump (interchain-2 in Figure 14c-2) in layered Li_4OCl_2 was calculated to be 0.380 eV, which is very close to the 0.370 eV for 3-D Li_3OCl. The energy barrier of X1-X2 jump (interchain-1 in Figure 14c-2) was even lower (0.310 eV), which might be caused by reduced negative electrostatic attraction from surrounding anions. There are also three potential diffusion pathways in 1-D antiperovskite. The interchain pathway also displayed the highest diffusion barrier (0.397 eV), which however is nearly half of that calculated for 2-D antiperovskite (0.800 eV). An extremely low diffusion barrier (0.060 eV) was found for one of the interchain Li^+ jump (interchain-2 in Figure 14c-3), but this motion does not determine the conductivity because it is not percolative. The diffusion barrier of the other interchain jump was found to be 0.211, which is much lower than that of 2-D and 3-D antiperovskites. 0-D antiperovskite structure has two potential Li^+ transport pathways; one is the Li^+ circulation around O center with a barrier of 0.047 eV, and the other is the Li^+ hopping between two separate Li_6O octahedra with a barrier of 0.160 eV.[110] The former one is a localized Li+ motion while the latter one contributes to the long-range Li diffusion directly. These examples show the feasibility of introducing low-energy diffusion pathways by lowering the dimension of antiperovskites. Moreover, it is interesting to note that the proposed Li^+ circulation in 0-D antiperovskite is similar to the aforementioned polyatomic anion rotation. From this prospect, the separated Li_6O octahedra might be a polyatomic unit in practice and possesses the highest degrees of rotational freedom, while Li^+ cations are under-coordinated compared to that in 3-D antiperovskite structures, which might explain the low cation diffusion activation energy.

5.3.4. Reducing Intergranular/Intragranular Pores and Grain Boundaries.

The above conclusions are made on the basis of ionic conductions inside single antiperovskite grain with only point defects. Practical ionic conductions in the electrolyte layer of solid-state batteries are in fact influenced by the intergranular/intragranular pores and grain boundaries as well. The pore effects are generally recognized as detrimental for conduction in all inorganic electrolytes since pores bring in clear physical gaps in otherwise continuous electrolyte layers and disconnect the diffusion pathways in some directions. Therefore, electrolyte layers that are assembled from powders must be densified in order to mitigate pore effects and achieve desirable conductivities. Most sulfide electrolytes are ductile and can be readily densified through cold pressing and the density will be higher if pressing is conducted with simultaneous heating at slightly elevated temperatures. Oxide electrolytes are usually rigid particles and need to be densified through a secondary annealing below the melting points. The underlying grain boundary effects on the other hand are not fully understood and are controversial. Many researchers found low ionic conductivities in electrolytes, particularly the oxide electrolytes, due to the high grain boundary resistances. Coarsened grain or even single-crystal structures are therefore suggested in oxide electrolytes to mitigate this grain boundary effect.[179−181] However, the grain boundary resistance has been found to barely affect the ionic conductivities in sulfide electrolytes. Some even demonstrated that grain boundaries in sulfide electrolytes could contribute faster transport by providing under-coordination of conducting ions.[182] Nevertheless, grain boundary structures are rarely characterized and their influences on ionic conductivities are seldom quantified in detail. They are often mixed with the pore effects since grain coarsening and pore reduction both occur during the annealing process of oxide electrolytes. It has been recognized as impossible to determine whether grain boundaries will be detrimental or beneficial for ionic conduction in a new electrolyte until comprehensive investigations are performed.[183,184]

Antiperovskite electrolytes with oxygen as backbone element perform similarly to the traditional oxide electrolytes. The lack of in-depth grain boundary analysis is also true for antiperovskite electrolytes. In the first Li_3OA (A = Cl, Br) work by Zhao et al., the measured activation energy for Li_3OCl was 0.26 eV, which coincides with the value of 0.2−0.3 eV determined in simulations.[118,164,183] However, recently experimental results gave quite different values of 0.6−0.8 eV.[115,137] This discrepancy has not been explained yet, but after reviewing these data and corresponding experimental procedures we reckon that it might be attributed to the grain boundary effects. In the early Li_3OA work, antiperovskite electrolyte pellets were prepared directly from cutting the solidified melt samples without crushing they into powders, which helps to diminish pore and grain boundary effects. Samples from powder pressing were also prepared for comparison and displayed rather low ionic conductivities (in the range of 10^{-7} S/cm at room temperature, compared with the 10^{-4}~10^{-3} S/cm for the samples cut from melt). After annealing the pressed samples above 250 °C for 24 h, the room-temperature ionic conductivities were increased by 2 orders of magnitude.[11] Many other antiperovskite electrolytes were developed after this work and displayed the similar tendency.[14,115,117,185] Although the high resistance contributions from grain boundaries were often observed in these antiperovskites (e.g., 8.8 and 83.0 kΩ for bulk and grain boundary resistances in Li_3OBr, respectively[86]), explanations of the grain

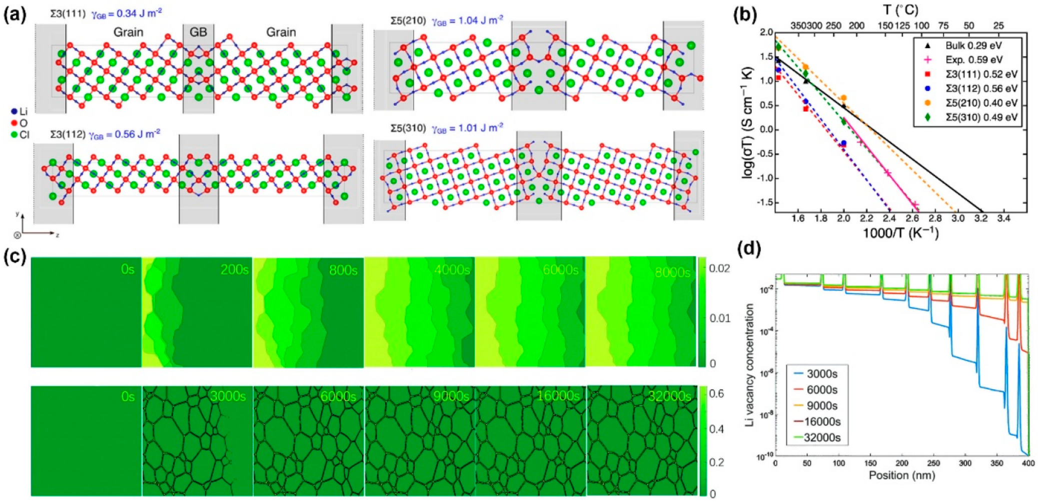

Figure 15. (a) Structures and energies of the ∑3(111), ∑3(112), ∑5(210), and ∑5(310) grain boundaries. x−y plane corresponds to the grain boundary plane and z is perpendicular to the plane. (b) Temperature dependence of the conductivities of bulk Li_3OCl and the four grain boundaries. Reproduced with permission from ref 183. Copyright 2017 American Chemical Society. (c) Schematic illustrations of Li vacancy distribution evolution versus time in polycrystalline Li_3OCl without segregation (upper panel) and with segregation (lower panel). The grain size is 40 nm. (d) Midline scans of the Li vacancy concentration in polycrystalline Li_3OCl with segregation along the filling direction (from left to right) at different times. Reproduced with permission from ref 187. Copyright 2020 the Owner Societies.

boundary effects at the atomic scale were not reported until attempts based on simulations were made recently.[115,183,186,187] Dawson et al. analyzed ionic transport at computed grain boundaries through large-scale molecular dynamics simulations.[183] They established four common symmetrically tilted grain boundary structures (i.e., ∑3(111), ∑3(112), ∑5(210), and ∑5(310)) based on the coincidence site lattice (CSL) theory and calculated the grain boundary energies, as shown in Figure 15a. The results revealed notably low grain boundary energies, especially in the two ∑3 types, suggesting that the ∑3 grain boundaries are likely to be present in high concentrations and dominate the grain boundary effects. The ionic conductivities of the four grain boundaries were found lower than the bulk values in the temperature range of 0 ∼ 150 °C, while the activation energies were significantly higher in all three primary directions (x, y, and z) compared to that in bulk conduction (Figure 15b). The less mobility can be understood by the overcoordination around the alkali ions at the grain boundaries, as has been revolved from the simulated local structures of Li_3OCl and Na_3PO_4.[115,182] It is worth noting that the situation is quite different from that in mechanically soft sulfide electrolytes where the alkali ions are under-coordinated at the grain boundaries and can move faster. As a result, the overall ionic conductivity in Li_3OCl decreases with decreasing grain size (particularly when it is smaller than 100 nm),[183] which is consistent with the trend observed in traditional oxide electrolytes and contrary to that in sulfide electrolytes.[182]

In addition to the direct reduction of cation mobility inside the grain boundaries, the impact of grain boundaries on Li^+ (or Na^+) conduction in antiperovskite may manifest in another aspect, point defect segregation at the grain boundaries. Defect segregation at grain boundaries is a very common phenomenon in inorganic materials and metals. However, it is less noticeable than the aforementioned influence on ionic conduction in inorganic electrolyte research and has been rarely reported. Nevertheless, the influence of this aspect may be profound since the mobile defects, which have been established as the critical charge carriers in SSEs, may also be trapped at grain boundaries in polycrystalline inorganic electrolytes and then further reduce the ionic conduction. Such effect in polycrystalline antiperovskite electrolytes was confirmed recently by Shen et al. based on a combination of first-principles and phase field calculations.[187] Negative segregation energies were obtained for the segregated Li vacancies near the four typical grain boundary structures (∑3(111), ∑3(112), ∑5(210), and ∑5(310)), with dramatically decreasing values as the site approaching the grain boundaries. This confirms that vacancy segregation at grain boundaries is energetically favorable and occurs in a very short-range (10−20 Å). Moreover, Li vacancy diffusion was simulated in polycrystalline Li_3OCl without and with considering the vacancy segregation, as shown in Figure 15c and d. The Li vacancy distribution without considering segregation showed clear gradients along the diffusion direction, which also suggests the detrimental influence from grain boundaries for Li vacancy conduction across them. After considering the segregation effect, it displayed major Li vacancy location at the grain boundaries. The effective diffusion coefficient of the Li vacancy (D_{eff}) was also found to decrease from 3.5% of the bulk diffusion coefficient (D_{bulk}) to 0.3% of the D_{bulk} in a polycrystalline Li_3OCl with an average grain size of 16 nm due to vacancy segregation at the grain boundaries, showing that Li vacancy segregation at the grain boundaries further decrease Li vacancy mobility. The ratio of D_{eff} values without and with vacancy segregation was about 12-fold for the polycrystalline sample with 16 nm grain size, which would decrease as the grain size increased (e.g., nearly 2-fold for the 133 nm grain size).

Therefore, the grain boundaries in polycrystalline antiperovskite electrolytes are likely to influence ionic conduction in generally two aspects. One is the direct high resistance to Li^+/Na^+ motion along or through the grain boundaries. The other is the trap of Li^+/Na^+ vacancies at grain boundaries, which eventually hinders charge carrier motion as well. Increasing the grain size or even eliminate grain boundaries might help to mitigate the detrimental influences on ionic conduction in antiperovskite electrolytes, which can be fulfilled by proper annealing or complete amorphization. Moreover, it has been shown grain boundaries with different orientations performed differently. Therefore, controlling the grain boundary orientation by potential strategies, such as growth substrate optimization, may be another option to enhance ionic conduction in polycrystalline samples.

5.3.5. Lattice Stress Control.

Lattice stress has aroused increasing interest in battery research in recent years mainly due to its influences on the structural stability of electrode materials, especially Si anode and NMC cathodes, in which huge volume variation takes place during the repeated intercalation and deintercalation of Li^+ and causes considerable lattice stress inside the active material particles. The overwhelming lattice stress would lead to cracks in secondary particles of the active materials, which accounts for the failure mechanism in many liquid electrolyte batteries. The lattice stress issue would be more interesting or severe in solid-state batteries where the volume changes cannot be transformed in to a homogeneous, hydrostatic ($\sigma_{xx} = \sigma_{yy} = \sigma_{zz}$) pressure through the liquid medium. Instead, additional lattice stress issues would arise in the SSEs and between the electrolyte and electrodes due to the deformation.[188] The pressure build-up process has been recognized in the volume-constrained solid-state batteries and the influences on the connection between SSEs and electrode materials have been intensively investigated. It is known that the distances between the atoms in inorganic materials will be changed under stress. Therefore, the SSEs may also undergo structure change as a result of the build-up pressure, which eventually affects the intrinsic ionic conduction properties.

The structure of Na_3OBr electrolyte was studied as a function of external mechanical pressure with in situ SR-XRD, which revealed that the cubic antiperovskite structure was quite stable under high pressure up to 23 GPa, and no octahedral tilt occurred.[189] The corresponding lattice parameter a showed a nearly linear decrease as the applied pressure increased. However, the pressure influence on the ionic conduction properties has not been reported in this sample or any other synthetic Li/Na antiperovskite electrolytes yet. The shortage can be mitigated by the investigations on conventional electrolyte systems, for example F^- and O^{2-} ion conductors. It has been shown that the critical temperature for F^- superionic conduction transition in CaF_2 could be increased as much as ~200 K under a hydrostatic pressure of 5 GPa,[189] suggesting the feasibility of tuning ionic conduction in SSEs via the control on stress. Moreover, it also reflected the detrimental influence of compressive hydrostatic stress ($\sigma > 0$) on ionic conduction. The tensile stress ($\sigma < 0$) would, on the other hand, exert positive influence on the ionic conduction property. The critical temperature of CaF_2 was reduced as much as ~300 K at a tensile hydrostatic stress of −5 GPa and ~250 K at a tensile biaxial stress ($\sigma_{xx} = \sigma_{yy} = -5$ GPa, $\sigma_{zz} = 0$), while a ~200 K decrease was obtained for the case with a tensile uniaxial stress ($\sigma_{xx} = \sigma_{yy} = 0$, $\sigma_{zz} = -5$ GPa).[190] The mechanism beneath the stress-induced enhancement is attributed to the expanded lattice under tensile stress in which the formation energy and kinetic barrier for Frenkel defects are both decreased. Similar stress effects have also been observed in O^{2-} conductors. For instance, the oxygen conductivity in yttria-stabilized zirconia showed an increase of 8 orders of magnitude as a result of tensile biaxial stress,[191] suggesting the great potential of the stress mediation route.

Considering that the Frenkel defects can be potentially introduced into antiperovskites, the stress mediation mechanism is likely to be applicable to the Li/Na antiperovskite electrolytes as well. Although experimental evidence have not been reported yet, the hypothesis has been verified through simulations.[192] The formation energy of Frenkel pair defects in Li_3OCl was found to decrease ~15% in the presence of a tensile biaxial stress of −1.5 GPa, whereas a ~12% increase was obtained from a compressive stress of 1.5 GPa.[192] This suggests that more Li^+ interstitials can be produced in Li_3OCl under tensile stress compared to the unstrained one. Moreover, the energy barrier for Li^+ migration would be simultaneously reduced as a result of the expanded lattice volume under tensile stress, similar to the free volume effect. Therefore, an enhanced ionic conduction can be anticipated as a result of the tensile strain.

In practical synthesis of SSEs, the aforementioned tensile biaxial stress (or strain) could be realized by depositing the target antiperovskite electrolyte on a substrate whose lattice parameter is larger than the electrolyte. For example, the lattice parameter of Li_3OCl is 3.91 Å;[11] a commercialized substrate $K(Ta_{1-x}Nb_x)O_3$ (lattice parameter: 3.99−4.00 Å) can then afford a tensile strain of around 2.0% to the deposited Li_3OCl. In addition to the conventional substrates, antiperovskite structure itself, for example Li_3OBr (lattice parameter: 4.02 Å[11]) can also be employed as a substrate to prepare Li_3OBr/Li_3OCl heterostructure and thus to induce a tensile strain of nearly 2.8%. Considering that the lattice parameter of antiperovskite structure varies with doping or substitution, nonuniform doping or substitution to form gradient electrolyte film might also be useful to induce desirable tensile strain and promote higher ionic conductivity. These designs can be best fulfilled in the thin-film formats of solid-state batteries in which electrolyte can be readily deposited on selected substrates through physical or chemical vapor depositions. However, it is noteworthy that the biaxial tensile strain is accompanied by a shrinkage along the direction perpendicular to the tensile strain plane as the Poisson's ratio of antiperovskite electrolytes are generally positive. This would cause anisotropic ionic conductions in these samples, with the in-plane ion migration are boosted while the out-of-plane migration is hampered. Therefore, the electrode and electrolyte stacking direction should be perpendicular to the growth direction of the electrolyte on substrate in order to induce the tensile stress effect, which will be quite different from the conventional layer-by-layer stacking of electrodes and electrolytes on substrates in present thin-film batteries.

6. OTHER PROPERTIES

Besides the ionic conductivity, material stability is another major concern for SSE development, which determines whether the target electrolytes can be synthesized with less impurity or can be used in practical environments. It is known that the moisture sensitivity and poor stability against Li anode hinder the application of sulfide electrolytes even though they have satisfying ionic conductivities. In this part, we will discuss the stability issues in antiperovskite electrolytes with respect to the phase stability, electrochemical stability and the stabilities toward atmospheric gases, hoping to provide a general guide to the processing of these new electrolytes for future practical applications.

6.1. Phase Stability

The stability issues of antiperovskites discussed in Section 2.1 are based on a geometrical point of view. In practical material development, it is necessary to consider the phase stability from dynamical and energetic aspects. Assessment of the dynamical stability of a given phase can be accomplished by checking its

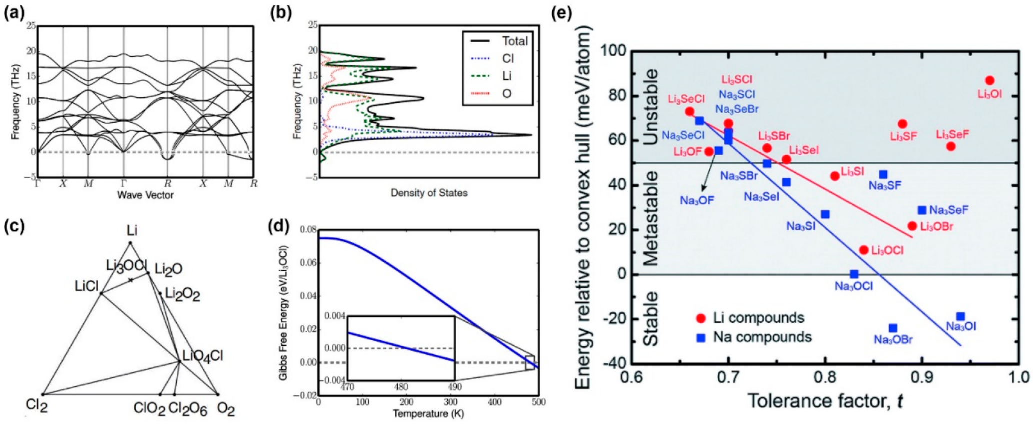

Figure 16. (a) Phonon dispersion curves and (b) density of states of Li_3OCl calculated by a finite displacement method. (c) Calculated ternary Li−O−Cl phase diagram. The solid circles show the stable compounds with lower energy compared to a linear combination of the constituent phases. (d) Temperature dependence of the Gibbs free energy for Li_3OCl antiperovskite electrolyte. (e) Tolerance factor and the energy relative to the convex hull (equivalent to the formation energy) for a series of model antiperovskite SSEs. (a), (b), and (d) are reproduced with permission from ref 119. Copyright 2015 American Physical Society. (c) is reproduced with permission from ref 118. Copyright 2013 American Physical Society. (e) is reproduced with permission from ref 194. Copyright 2019 The Royal Society of Chemistry.

phonon dispersion. The absence of phonon bands associated with imaginary (negative) frequencies in the phonon dispersion curve is often indicative of a dynamically stable phase, for example in Li_3OBr. Simulated Li_3OF structure, on the other hand, displayed substantial imaginary frequencies, indicating its dynamical instability. This is coincided with the fact that the efforts in synthesizing Li_3OF ended in failure. It is noteworthy that the prototypical antiperovskite Li_3OCl also displays imaginary frequencies (photo modes at R and M as shown in Figure 16a). These unstable modes are in fact related to the octahedra rotation, which does not disrupt the overall crystal lattice. As can be observed from the phonon densities of states (Figure 16b), the unstable modes take a small fraction of the total phonon modes and involve only Li cations.[119,193] Therefore, Li_3OCl antiperovskite structure can be synthesized from the viewpoint of dynamic stability but are most likely in a lower energy tilt system other than the $Pm\bar{3}m$.

In addition to the dynamic stability, the formability of an antiperovskite structure should also be evaluated from its stability relative to the corresponding stable constituent phases (i.e., energetic stability). The ternary Li−O−Cl phase diagram, for example, has been constructed at 0 K through minimizing the formation energies of various compositions,[118] as shown in Figure 16c. This phase diagram predicts that Li_3OCl is energetically unstable due to the positive formation energy with respect to that from the Li_2O and LiCl and tends to decompose through the reaction:

$$Li_3OCl \rightarrow Li_2O + LiCl \quad (20)$$

Nevertheless, the energy above the hull (E_{hull}) for Li_3OCl is only 13−22 meV per atom at 0 K,[118,163,195] which is located in the range of 0−50 meV per atom corresponding to the metastable phase of antiperovskite and perovskite structures and suggests the potential of stabilizing Li_3OCl by external conditions.[196] Proton-rich antiperovskite $Li_2(OH)Cl$ is also a metastable phase with the E_{hull} value of 10 meV per atom.[197] In fact, many reported superionic conductors possess positive formation energy but are still synthesizable. A well-known example is the $Li_{10}GeP_2S_{12}$ electrolyte that has a value of 25 meV per atom.[198] Entropy is such an external condition. The Gibbs free energy of a system under certain temperature and pressure can be obtained based on quasi-harmonic approximation.[199] Then using the Gibbs free energies for the three phases, the formation free energy for Li_3OCl can be calculated:[26,119]

$$\Delta G_{Li_3OCl} = G_{Li_3OCl} - G_{Li_2O} - G_{LiCl} \quad (21)$$

It has been shown that the value decreases as the temperature increases and becomes negative when temperature is above ~480 K (207 °C) (Figure 16d), indicating that Li_3OCl can be stabilized at the elevated temperatures.[119] However, it can be inferred from the calculation that a Li_3OCl phase decomposition reaction will occur when temperature is decreased during the cooling process, producing the LiCl and Li_2O impurities that have much lower ionic conductivities. Therefore, it is necessary to avoid the nucleation and growth of the undesirable low-temperature phases in order to achieve a reasonable ionic conductivity. A possible solution to this issue might be the application of rapid cooling immediately after the heating process, which can effectively reduce the window of time during which the low-temperature phases are produced. It should be noted that the metastable phase can be stabilized by pressure as well, which has been confirmed in the case of Li_3OBr.[193] The energies relative to the convex hull (equivalent to the formation energy) of a series of model antiperovskite SSEs have been given (Figure 16e).[194] It is interesting to note that the corresponding Na counterparts (i.e., Na_3OCl and Na_3OBr) are energetically stable, which coincides with the fact that the Na counterparts can be prepared with a high purity without special treatment.

6.2. Intrinsic Electrochemical Stability

The electrochemical window of SSE is a critical parameter that determines the acceptable voltage ranges in full cells and therefore affects the energy densities. The claimed wide electrochemical windows (i.e., 0−5 V) in many SSEs were obtained from cyclic voltammetry (CV) measurements and demonstrated the potential of unlocking the high-voltage cathodes and the metallic Li anode.[4,200] The electrochemical window in $Li_2(OH)_{0.9}F_{0.1}Cl$ antiperovskite electrolyte can even reach 9 V.[104] These electrochemical windows are in fact not the intrinsic electrochemical stability window of the electrolyte, which contains a significant contribution from the high overpotential due to the sluggish decomposition kinetics.[201]

The artificial passivating layer in full cells would also extend the electrochemical windows. In this section, we will focus on the intrinsic electrochemical stability of antiperovskite electrolytes, hoping to promote a deep understanding of the electrochemical window from the perspective of electrolyte itself.

The intrinsic electrochemical stability of an electrolyte is usually assessed from two aspects, the stability against inert electrodes and the stability under chemical potential. The former one is assessed by calculating the energy difference between the lowest unoccupied molecular orbital (LUMO) and the highest occupied molecular orbital (HOMO) of the electrolyte.[202] The Heyd-Scuseria-Ernzerhof (HSE06) screened hybrid functional is usually used for this purpose.[203] According to this method, the calculated band structure of ground-state stable Li_3OCl antiperovskite, for example, reveals a large band gap of 6.26 eV (Figure 17a). This large band gap, although not an exact measurement of the intrinsic redox stability as its alignment with respect to reference potential is not known, provides a high upper limit for the intrinsic stability against reduction and oxidation,[204] suggesting the potential to increase system energy density by broadening the operating voltage range. The large band gap in Li_3OCl is in sharp contrast to many known electrolytes that have competitive ionic conductivities but suffer from small band gaps and poor electrochemical stabilities, for example the prototypical sulfide electrolytes $Li_7P_3S_{11}$ (3.9 eV[205]) and $Li_{10}GeP_2S_{12}$ (3.6 eV[198]). Moreover, the atomic contributions to electronic structures can be revealed by the density of states (DOS). As described previously, the valence band in antiperovskite structure is mainly contributed by the A and B site anions while the conduction band mainly originates from X site cations, as is the case for Li_3OCl (Figure 17a). The valence band for Li_3OCl is mainly determined by Cl and O atoms, while Li dominates the conduction band. A major modification to the Cl or O anion is therefore highly likely to introduce distinct band gaps. For example, BH_4^- polyatomic anions have larger vertical detachment energy than that of halogen anions. Substitution of Cl^- in Li_3OCl antiperovskite by BH_4^- increases the band gap to a remarkable value of 7.0 eV,[176] which is even higher than that of the well-known stable garnet electrolyte LLZO (6.4 eV[206]). On the other hand, substitution of the anions by those with less electron affinities decreases the band gap. For instance, partially replacing O^{2-} in Li_3OI by S^{2-} led to the Li_6OSI_2 double antiperovskite, accompanied by a reduction in the band gap (from 5.3 to 4.5 eV). Nevertheless, the resultant band gaps are still at a relatively high level, suggesting the intrinsic redox stability in antiperovskite type electrolytes. Moreover, the large band gaps also reflect that the antiperovskite electrolytes are good insulators with limited electrical conductivity, meeting the basic requirements for battery application.

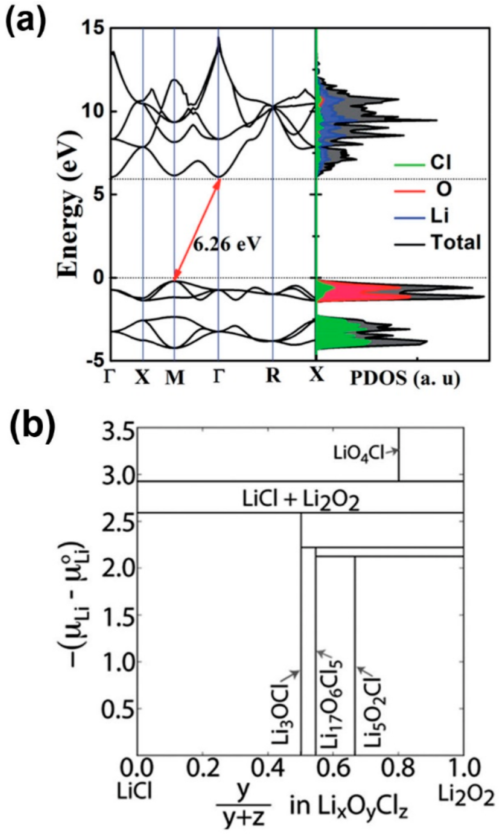

Figure 17. (a) Calculated electronic band structure and density of states for Li_3OCl using the Heyd-Scuseria-Ernzerhof (HSE) functionals. Reproduced with permission from ref 195. Copyright 2018 The Royal Society of Chemistry. (b) Phase diagram of O/Cl composition versus Li chemical potential. The calculation is based on the assumption that Li_3OCl decomposition into LiCl and Li_2O is suppressed. Reproduced with permission from ref 163. Copyright 2013 American Chemical Society.

It is noteworthy that the assessment of the electrochemical stability from electronic structure theory is a rough estimation in which the energy difference of HOMO and LUMO should not be mixed up with the electrochemical stability window. The redox potentials are in fact directly related to the Gibbs free energy difference of the reactants and the products,[207] which can be reflected by the lithium (or sodium) grand potential phase diagrams. The SSEs in practical lithium batteries, for example, are in contact with electrode materials and therefore in principle could react with all the components from the electrode materials. The reactivity with Li species is the most critical since both anode and cathode are Li reservoirs while Li is highly mobile. Therefore, the electrolytes are under a changing Li chemical potential (μ_{Li}). The chemical potential at the metallic Li anode side is very high, which is generally set to zero ($\mu_{Li} = 0$). Therefore, electrolyte tends to be reduced at the anode side by Li uptake. The cathode, on the other hand, has a low Li chemical potential (represented by a negative μ_{Li}) and is likely to oxidize the electrolyte by Li extraction. The cell voltage is given by the Li chemical potential difference between anode and cathode, and then is the negative of μ_{Li}. Phase evolution of electrolytes under the changing chemical potential can be tracked from the phase diagram, and the equilibrium phases at the reductive Li anode and oxidizing cathode can also be determined. The phase diagram of O/Cl composition versus Li chemical potential was constructed by Emly et al.,[163] as shown in Figure 17b. The phase diagram indicates that the Li_3OCl phase is stable up to 2.55 eV (on the basis of suppressed Li_3OCl decomposition into LiCl and Li_2O), and will decompose into Li_2O_2 and LiCl above 2.55 eV.[163] This oxidation potential limit is generally lower than that of oxide electrolytes but higher than that of most sulfide electrolytes (Table 3). The stable potential range is significantly narrower than those calculated from electronic structure approach. In addition, the delithiation reactions continue at higher voltages. Cl_2 and ClO_2 might appear during the oxidation above 4.0 eV,[118] similar to the O_2 gas evolution at high voltages for all oxide-based SSEs. The decomposition would cause

Table 3. Summary of Electrochemical Windows (EW), Equilibria Phases at Reduction and Oxidation Potentials, and Mechanical Properties of Some Typical Li/Na Ionic Conductors

				mechanical properties				
electrolyte	EW vs Li/Na (V)	equilibria phase at reduction potential	equilibria phase at oxidation potential	Young's modulus E (GPa)	Poisson's ratio ν	shear modulus G (GPa)	bulk modulus K (GPa)	ref
$Li_{10}GeP_2S_{12}$ (LGPS)	1.71−2.14	P, Li_4GeS_4, Li_2S	Li_3PS_4, GeS_2, S	21.7	0.37	7.9	27.3	201, 208
Li_3PS_4	1.71−2.31	P, Li_2S	S, P_2S_5	29.5	0.29	11.4	23.3	201, 208
$Li_7P_3S_{11}$	2.28−2.31	Li_3PS_4, P_4S_9	S, P_2S_5	21.9	0.35	8.1	23.9	201, 208
Li_6PS_5Cl	1.71−2.01	P, Li_2S, LiCl	Li_3PS_4, LiCl, S	22.1	0.37	8.1	28.7	201, 208
LiPON	0.68−2.63	Li_3P, $LiPN_2$, Li_2O	P_3N_5, $Li_4P_2O_7$, N_2	77.0	0.25	31.0	51.3	201, 209
$Li_7La_3Zr_2O_{12}$ (LLZO)	0.05−2.91	Zr_3O, La_2O_3, Li_2O	Li_2O_2, La_2O_3, $Li_6Zr_2O_7$	175.1	0.27	68.9	127.4	201, 208
$Li_{0.33}La_{0.56}TiO_3$ (LLTO)	1.75−3.71	$Li_4Ti_5O_{12}$, $Li_{7/6}Ti_{11/6}O_4$, $La_2Ti_2O_7$	O_2, TiO_2, $La_2Ti_2O_7$	233.9−262.5	0.26−0.28	91.2−104.0	179.0−183.5	201, 208
$Li_{1.3}Ti_{1.7}Al_{0.3}(PO_4)_3$ (LATP)	2.17−4.21	P, $LiTiPO_5$, $AlPO_4$, Li_3PO_4	O_2, $LiTi_2(PO_4)_3$, $Li_4P_2O_7$, $AlPO_4$	143.7	0.25	57.6	95.0	201, 208
$Li_{3.5}Zn_{0.25}GeO_4$ (LISICON)	1.44−3.39	Zn, Li_4GeO_4	O_2, Li_2ZnGeO_4, Li_2GeO_3					201
Li_3InCl_6	2.38−4.3	LiCl, In_2Cl_3	Cl_2, $InCl_3$			13.8[a]	36.3[a]	210
Li_3YCl_6	0.62−4.21	LiCl, Y	Cl_2, YCl_3	38.11	0.274	14.95	28.19	210, 211
Li_3OCl	0−2.55	Li_3OCl	Li_2O_2, LiCl	99.7	0.20	41.5	55.7	163, 208
$Li_2(OH)Cl$	0.82−3.15	Li_2O, LiCl, LiH	LiH_2ClO_5, H_2O, LiCl	43.1	0.24	17.4	27.6	212
Na_3PS_4	1.39−2.45	Na_3P, Na_2S	S, P_2S_5	32.6	0.25	13.1	21.5	208, 213
Na_3SbS_4	1.83−1.90	Na_3Sb, Na_2S	$NaSbS_2$, NaS_2					213
$NaZr_2(PO_4)_3$	1.58−4.68	Na_3P, ZrO_2, Na_3PO_4	O_2, $Zr_2P_2O_9$, ZrP_2O_7	120.9	0.27	47.7	86.3	208, 213
Na_3AlF_6	0.46−6.19	Al, NaF	F_2, AlF_3			28	51	213, 214
Na_3OBr	0−1.79	Na_3OBr	Na_2O_2, NaBr	57.4	0.22	23.6	34.0	208, 213

[a] Predicated by materials project. https://materialsproject.org/materials/mp-676109/.

problems for the employment of high-voltage cathodes in batteries with high energy densities. Nevertheless, it should be noted that the electrolyte decomposition depends on kinetic factors, which means decomposition of a phase might be slowed down or interrupted under certain circumstances, for example, a sluggish ion/electron transport in decomposed phases. Moreover, possible reactions involving non-Li species from electrodes are also not clear. More efforts are needed to investigate the electrochemical stabilities of antiperovskite electrolytes.

6.3. Air Stability

The air stability of a SSE is of practical importance in solid-state battery development involving the electrolyte processing and battery assembling, in which the electrolyte will be inevitably exposed to air and undergo structural changes if it is not chemically stable. It might be argued that all the steps could be conducted in an inert atmosphere (e.g., N_2 or Ar); however, it is neither economical nor efficient for large-scale manufacturing. Electrolytes with intrinsic air stabilities are thus highly desirable in both academic and industrial communities. The research interest on air stability of SSEs arises with the development of sulfide electrolytes, such as $Li_2S-P_2S_5$ binary systems, $Li_{10}GeP_2S_{12}$ and the argyrodite family.[4,5,215] These electrolytes generally have high ionic conductivity but are subject to poor chemical stability in air. They tend to decompose and produce harmful H_2S gas due to the hydrolysis reaction with moisture in air,[216,217] which can be understood by the negative Gibbs free energy of the reaction.[218] The air instability also remains as a challenge for oxide electrolytes. Instead of the H_2S issue, the instability of oxide electrolytes is usually reflected as a high interfacial resistance, which is indirectly detected. As a result, oxide electrolytes (e.g., garnets) were initially recognized as stable in ambient air. However, both experimental and theoretical investigations confirm that oxide electrolytes are susceptible to reactions with H_2O as well as CO_2. Nyman et al. revealed the exchange of Li^+ from the garnet lattice with the H^+ from H_2O and found a pH increase in the electrolyte/water suspension.[219] Wang et al. reported a tetragonal-cubic phase transition of LLZO under dry CO_2 exposure.[220] The reaction mechanism of LLZO in air has been investigated by Cheng et al. based on DFT calculations, which can be expressed as follows:[221]

$$\begin{aligned} &Li_{56}La_{24}Zr_{16}O_{96}(s) + H_2O(g) \\ &\quad = Li_{54}La_{24}Zr_{16}O_{95}(s) + 2LiOH(s) \end{aligned} \tag{22}$$

$$\begin{aligned} &Li_{56}La_{24}Zr_{16}O_{96}(s) + CO_2(g) \\ &\quad = Li_{54}La_{24}Zr_{16}O_{95}(s) + Li_2CO_3(s) \end{aligned} \tag{23}$$

Both reactions are energetically favored because of the negative Gibbs free energy. The reaction with H_2O is believed to be more rapid, and produce a LiOH intermediate that subsequently absorbs CO_2 to form Li_2CO_3. The reaction with CO_2 produces Li_2CO_3 directly but proceeds with slower kinetics.

Halide electrolytes are generally stable in dry air because the oxidation potential of Cl^- is much higher than O^{2-}, and O_2 from the air cannot oxidize the Cl^- anion in an ambient environment. Asano et al. investigated the stability of Li_3YCl_6 and Li_3YBr_6 in different atmospheres.[222] Li_3YCl_6 and Li_3YBr_6 electrolytes showed promising thermal and oxidation stability without any thermal decomposition, phase transition, or oxidation reaction in both Ar and O_2. On the basis of the theoretical calculations from Mo's group, most halide electrolytes of Li-M-Cl are stable in contact with tracer amount of H_2O due to the positive hydrolysis reaction energies.[223] The moisture stability is much less of an issue for chlorides compared to sulfides. However, many Li-M-Cl electrolytes suffer from irreversible chemical degradation in experiments when exposed to a highly humid atmosphere. For example, when the Li_3InCl_6 SSE is exposed to an environment with 3−5% humidity, the ionic conductivity of Li_3InCl_6 can still achieve over 10^{-3} S/cm and 10^{-4} S/cm after exposure for 7.5 and 24 h, respectively.[224] When increasing the humidity to 30%, the conductivity of exposed Li_3InCl_6 reduced to 3.98×10^{-7} S/cm after 24 h exposure. However, the ionic conductivity for Li_3YCl_6 electrolytes dropped to 10^{-7} S/cm after 12 h exposure even in 3−5% humidity environment.[225] Additionally, Li_3InCl_6 can be recovered over 92% of its initial ionic conductivity after reheating, while a value of only 0.8% of the initial ionic conductivity was retained for Li_3YCl_6.[225] To understand the degradation mechanism of Li_3InCl_6 exposed to air, in situ and operando optical microscopy, Raman spectroscopy and synchrotron X-ray analytical techniques were carried out to track the chemical and structural changes.[226] It is found that Li_3InCl_6 is hydrophilic, leading to the absorption of moisture from the air. A small portion of Li_3InCl_6 reacts with absorbed H_2O to form In_2O_3, LiCl and HCl, resulting in a decrease in ionic conductivity. Moreover, the remaining electrolyte absorbs H_2O to form a hydrate, $Li_3InCl_6{\cdot}xH_2O$. The $Li_3InCl_6{\cdot}xH_2O$ can be dehydrated to produce Li_3InCl_6, and then the ionic conductivity can be recovered after reheating at 200 °C under vacuum, leading to high tolerance to water. However, the Li_3YCl_6 electrolyte degraded to $YCl_3{\cdot}6H_2O$ and $LiCl{\cdot}H_2O$ even in the low humidity of 3−5%, and cannot be reformed after reheating the sample in a vacuum or inert atmosphere.[227]

Most antiperovskite electrolytes are composed of a large fraction of halide and are highly hygroscopic. Exposure of these electrolytes to air for even a few seconds can lead to the abnormally high "ionic conductivity" based on impendence measurement, which has been attributed to the undesired proton movement.[104] Therefore, moisture is strictly avoided in most antiperovskite electrolyte studies. It is noteworthy that Braga et al., on the contrary, proposed the intentional usage of water during antiperovskite electrolyte synthesis.[13,16] They added some water into the reactants and prepared the Li_3OCl series glass electrolytes in which they obtained the extremely high conductivity (2.5×10^{-2} S/cm at 25 °C). However, the proposed Li_3OCl glass phase in the final product remains controversial as it only reflects as a broad hump or featureless background in the powder XRD pattern. Other amorphous phases may also exist in the product. Recently, Dawson et al. calculated the hydration enthalpy for the Li_3OCl structure based on the following reaction:[158]

$$Li_3OCl + \frac{1}{2}H_2O \rightarrow Li_2(OH)Cl + \frac{1}{2}Li_2O \tag{24}$$

A strongly exothermic value was predicted for the reaction, suggesting a high tendency of Li^+/H^+ exchange in the Li_3OCl and the difficulty in synthesizing H-free samples. Hanghofer et al. also reported the moisture sensitivity of Li_3OCl and pointed out that traces of water could initiate the decomposition.[228] A wide spectrum of approaches were adopted for material characterization in their investigation, including powder X-ray diffraction, powder neutron diffraction and nuclear magnetic resonance spectroscopy. They revealed that the fresh Li_3OCl sample is more likely to be $Li_2(OH)Cl$ and will undergo rapid degradation and eventually transform into Li_2CO_3 and amorphous $LiCl{\cdot}xH_2O$ when exposed to air via the following reactions:

$$2Li_2(OH)Cl + H_2O \rightarrow Li_4(OH)_3Cl + HCl \tag{25}$$

$$Li_4(OH)_3Cl + CO_2 + HCl \rightarrow 2LiCl + Li_2CO_3 + 2H_2O \tag{26}$$

$$LiCl + xH_2O \rightarrow LiCl{\cdot}xH_2O \tag{27}$$

According to the study, $Li_4(OH)_3Cl$ forms as a hydrolysis intermediate and subsequently reacts with CO_2 and HCl to produce LiCl, Li_2CO_3 and H_2O. It was also suggested that the $Li_4(OH)_3Cl$ intermediate might first react with H_2O and transform into LiOH and LiCl. Then, LiOH will react with CO_2 to produce Li_2CO_3. Since hydrated LiCl (i.e., $LiCl{\cdot}xH_2O$) is energetically favored compared to LiCl, $LiCl{\cdot}xH_2O$ is likely to emerge as the hydrolysis product along with the Li_2CO_3, which is consistent with the reported existence of $LiCl{\cdot}H_2O$ phase in hydrolyzed Li_3OCl.[229] Moreover, Hanghofer et al. suggested that the measured extraordinary ionic conductivities in Braga's work may come from the electrical conduction of the highly hydrated forms of $LiCl{\cdot}xH_2O$, which show the same broad hump in powder XRD signal reported by Braga et al. and usually take conductivity values from 1.0×10^{-2} to 1.4×10^{-1} S/cm.[228] Despite the discrepancy, there is no doubt that the existence of H_2O, no matter during electrolyte synthesis or after synthesis, has a significant influence on the ionic conductivity results acquired from impedance measurements. More evidence is needed to verify these assumptions and one of the most direct solutions might be to distinguish ionic conduction, proton conduction and electronic conduction directly in these systems. Comprehensive structure and composition characterizations of the hydrolysis products as well as the starting materials are also needed for analyzing the degradation process before any further conclusions can be made.

On the other hand, understanding the atomistic origins of the degradation is an important step for the design and synthesis of antiperovskite electrolytes with enhanced air stabilities. The interactions of antiperovskite frameworks with H_2O or CO_2 molecules are critical for this study but remain hardly explored. Nevertheless, experience from the intensive investigations on halide perovskite systems may provide some guidance in the treatment of antiperovskite counterparts. The most widely employed hybrid perovskite solar cell material, methylammonium lead iodide ($CH_3NH_3PbI_3$ or $MAPbI_3$), is also subject to degradation in the presence of moisture.[230] Molecular dynamics simulations have shown that the degradation of $MAPbI_3$

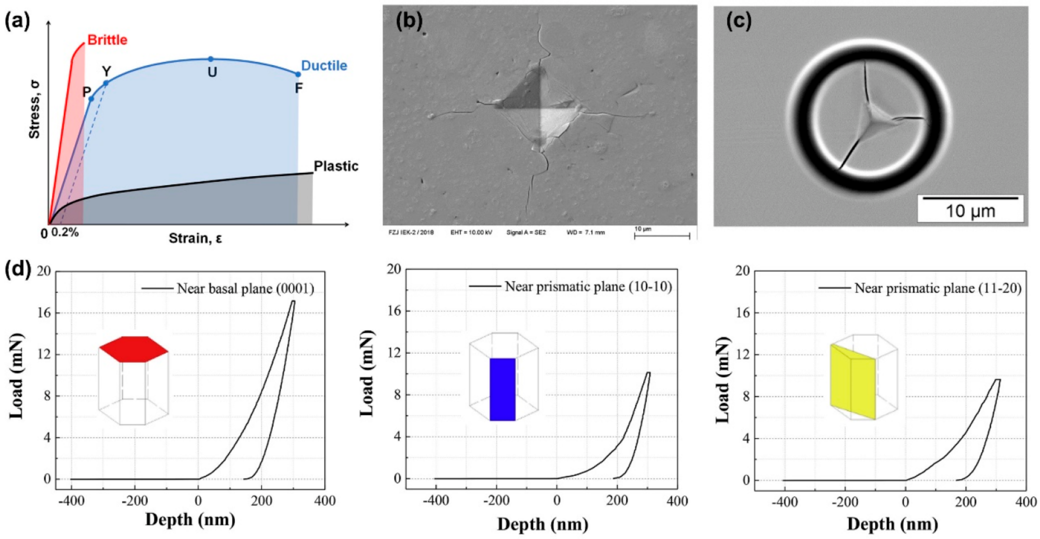

Figure 18. (a) Typical stress−strain curves for brittle, ductile and plastic materials. P, Y, U, and F represent the proportional limit, yield point, ultimate tensile strength and fracture point, respectively. (b) Vickers indentation image of LLZO electrolyte. Reproduced with permission from ref 236. Copyright 2020 Elsevier Ltd. (c) Micropillar indentation image of Al-substituted LLZO. Reproduced with permission from ref 237. Copyright 2018 Elsevier Ltd. (d) Typical load−displacement curves for indentation test in specific orientations. Reproduced with permission from ref 238. Copyright 2019 Elsevier B.V.

perovskite is initiated by H_2O adsorption, which takes place between the organic cation MA^+ and the inorganic framework $[PbI_3]^-$ due to the Coulomb attraction. The trapped H_2O molecule then serves as a catalyst to remove I^- from $[PbI_3]^-$, producing PbI_2 and isolated I^-. The highly negative I^- then takes a proton from MA^+ and forms HI.[77] On the basis of this result, the degradation process of $MAPbI_3$ perovskite can be slowed down or even cut off through two routes: (i) to weaken the interaction between H_2O and $[PbI_3]^-$ so as to reduce H_2O adsorption; (ii) to provide a new $[PbX_3]^-$ framework with stronger Pb-X bonding so that X^- become less likely to be separated from $[PbX_3]^-$. It has been demonstrated that the total charge of −1 could be well-distributed among cluster ions with multi atoms (e.g., SCN^- and $SeCN^-$), generating a weaker interaction with the H_2O molecule than the single I^- ions does. Moreover, the bonding strength of Pb-X will be simultaneously enhanced if I^- ions is replaced by the cluster ions.[27] As a result, the simulated moisture stability of the hybrid perovskite can be significantly improved, which has also been verified from experimental results.[231] In the case of antiperovskite structures, halide anions usually located at the relatively free A sites may accelerate H_2O adsorption and lead to the rapid structure degradation. Following the idea of internal charge distribution, the drawback may be mitigated by substituting the halide anions with suitable cluster ions. Moreover, the ionic conduction in antiperovskites can be accelerated by the introduction of cluster ions, as discussed in Section 5.3, making this strategy particularly attractive.

6.4. Mechanical Properties

The mechanical properties of an electrolyte reflect its tolerance to applied force or stress, but have aroused less attention compared to the aforementioned chemical stabilities. However, it has a profound influence on the postsynthetic processing of electrolytes and the performance of full cells. For example, it is critical to achieve intimate contact between the electrolyte and electrode so as to build intergranular ionic pathways, but it remains as one of the major challenges in solid-state battery fabrication due to the poor solid−solid contact between the electrolyte and electrode. In those with "soft" electrolytes, for example many sulfides or halides, reasonable solid−solid contact can be fulfilled by cold pressing and further enhanced by hot pressing, whereas it is hard for the rigid electrolytes, such as oxide electrolytes. High temperature treatment is often needed to prepare the oxide electrolyte sheets as well as the electrolyte-electrode composites, which will introduce residual stresses inside the layers and may cause cracks or fractures if they do not have proper mechanical properties. In addition to the challenge in battery fabrication, the solid−solid contact issue also occurs during battery operation due to the stress/strain build-up in solid-state batteries. The repeated lattice expansion and shrinkage of electrode materials during cycling introduce dynamic stress on the electrolyte layer. Moreover, the stress at grain boundaries can also be built up under temperature variation due to the mismatch in thermal expansion coefficients. These require the electrolyte to be able to deform as a response to the electrode volume changes so as to avoid cracks or pores between them. The ideal electrolytes are supposed to be "soft" to accommodate the large strains before plastic deformation takes place. On the other hand, the employment of metallic Li as anode in solid-state batteries is highly desirable but hindered by the formation of Li dendrite. Linear elasticity analyses performed by Monroe and Newman suggested that SSEs with sufficient shear modulus (at least twice that of metallic Li, ∼8.5 GPa) could effectively suppress Li dendrite formation.[232] Porz et al. argued that the shear modulus was not the dominant factor to control dendrite formation and pointed out that Li penetrated at defects but only when the current density is above certain critical point.[233] Raj and Wolfenstine also identified the critical current density for dendrite formation in SSE system and found its dependence on the ionic conductivity and fracture strength of the electrolyte.[234] In spite of the divergence, the mechanical properties of SSEs are of increasing importance as the investigations delve into the full cell level. Understanding how electrolytes respond to the force or stress is essential for the practical full cell application.

There are a number of terms used to describe the mechanical properties, for example Young's modulus, plasticity, strength, stiffness, toughness, and brittleness. Some of them can easily be confused with each other. Before discussing the electrolyte mechanical properties that may be useful in electrolyte design and application, it's important to review the general physical concepts behind the mechanical properties. Stress and strain are the two main concepts to start with. In typical cases involving tension or compression, stress (σ) is the ratio of applied force to a cross-section area, while strain (ε) is the ratio of the length change to the initial length, showing the deformation of a solid due to the stress. They can be expressed as

$$\sigma = \frac{F}{A_0} \tag{28}$$

$$\varepsilon = \frac{L - L_0}{L_0} = \frac{\delta}{L_0} \tag{29}$$

where F is the applied force and A_0 is the cross-section area. L_0 and L are the initial and elongated (or compressed) lengths, respectively. δ represents the length change. The relationship between the stress and strain can be given by the stress−strain curve from a tension or compression test on a material specimen. A typical curve is shown in Figure 18a. There are several points of interest in the curve of a specimen of ductile material (e.g., steel and copper), including the proportional limit (P), yield point (Y), ultimate strength (U) and fracture point (F).[235] The stress−strain curve follows a linear relationship from the origin point to the proportional limit (P), which is described by Hooke's law:

$$\sigma = \mathrm{E}\varepsilon \tag{30}$$

where E is the slope of the linear line and generally called Young's modulus. The deformation of the specimen in this region is elastic, which means that it can return to its initial state when the stress is unloaded. The tendency for the recovering (or the resistance to elastic deformation) is generally called stiffness, and it is evaluated by the value of the Young's modulus E.

The stress−strain relationships are identical in materials under tension or compression as long as the stresses are below the P point. Moreover, similar relationship also exists in samples under shear stress/strain and can be described by Hooke's Law. The corresponding slope in this case is referred to as the shear modulus (G), which can be related to the Young's modulus (E) by

$$\mathrm{G} = \frac{E}{2(1 + \nu)} \tag{31}$$

where ν is the ratio of lateral strain to axial strain and noted as the Poisson's ratio.

The deformation is still elastic in the region from the proportional limit (P) to the yield point (Y) even though the stress−strain curve does not follow the linear relationship. The maximum energy that the specimen can absorb during elastic deformation is defined as the resilience of the specimen, which can be calculated by taking the area under the stress−strain curve from the origin to the yield point. Permanent deformation occurs when the applied stress is beyond the yield point. In some cases, the exact yield point cannot be clearly identified from the stress−strain curve, and an offset yield point is defined under this circumstance. The point is set by drawing a parallel line offset by 0.2% strain, and the intercept point with the stress−strain curve is the target point. The associated stress at this point is known as the yield strength or proof stress. The ultimate tensile strength (U), or tensile strength, is the next step from yield point and shows the maximum stress that the specimen can withstand before fracture occurs. When the stress is in the range from yield point to ultimate strength, the strength of the sample increases as a result of strain hardening. Beyond the ultimate strength, the specimen undergoes necking, and eventually breaks at the fracture point (F). Stress associated with this point is called the fracture strength or breaking strength. In contrast to the resilience, the total energy that can be absorbed by the sample without fracturing is called toughness. Modulus of toughness is calculated as the area under the stress−strain curve from the origin to the fracture point, as highlighted in Figure 18a. Fracture toughness (K) is one definition of toughness, which measures a material's resistance to fracture in the presence of a crack or other stress-concentrating defect and represents a key parameter for evaluating the stability of SSEs in operating solid-state batteries from mechanical viewpoint. It has been widely recognized that defects (e.g., microcracks) could be generated in electrolyte membranes during synthesis or cell operation and lower the ionic conductivity.[239] Therefore, a high fracture toughness is desirable to resist crack propagation and keep the integrity and conductivity of the electrolyte layer. Moreover, it is noteworthy that the resilience or toughness is often confused with the term of hardness that measures the ability of a material to resist localized plastic deformation from compressive loads, including denting, bouncing and scratching. A large hardness in materials represents the high resistance to surface deformation and the value can be given by a variety of measurements, for example the Vickers hardness testing as a common route.[240]

The behaviors of specimens made from plastic and brittle materials under stress are different from that of ductile samples, as shown in Figure 18a. Plastic materials (e.g., organic polymers) also exhibit elastic and plastic deformations; however, the elastic deformation occurs in a much smaller stress region than that in ductile materials. Moreover, the plastic materials do not display strain hardening during the plastic deformation. Brittle materials, on the other hand, display little elastic deformation and hardly any plastic deformation before fracturing. Brittle materials can only absorb very limited energy and will sustain fracture without significant strain. The yield strength, ultimate and fracture strength of these materials are usually the same. It can be estimated from the stress−strain diagrams that a brittle material may have a small toughness although it has a higher ultimate tensile strength. The plastic material also shows a small toughness in spite of the high ductility. From this viewpoint, materials with both a high ultimate tensile strength and a high ductility are likely to achieve a large toughness.

Materials are generally designed to operate within their elastic deformation region, especially for the inorganic electrolytes that are intrinsically brittle. SSEs in practical full cells must possess appropriate elastic properties in order to deform elastically and effectively compensate stress released from electrode materials, which will otherwise build up concentrated stress at the interfaces and cause cracks in the electrode or disconnection between the electrode and electrolyte, and eventually lead to cell failure. It is also necessary to suppress fracturing or flaw propagation under an applied stress. Therefore, it is important to evaluate the mechanical properties of SSEs for all-solid-state battery application. However, there have been only a few reports on this topic. Recently, efforts from experimental and theoretical exploration have shown some progress. The experimental data of the mechanical properties of SSEs were collected primarily from oxide electrolytes through the indentation route (Figure 18b,c). Cho et al. characterized the Young's modulus and hardness of LLTO through the nanoindentation and Vickers indentation.[241] The Young's modulus and hardness of LLTO were measured to be ∼200 GPa and ∼9.2 GPa, respectively. Such high Young's modulus and hardness were suggested to ensure mechanical integrity of the electrolyte in aqueous Li−air batteries. The fracture toughness of LLTO was further determined based on the length of the Vickers-induced cracks and measured to be ∼1 MPa $m^{1/2}$, which was considered to be low. Wang et al. investigated the mechanical properties of Al-substituted LLZO by utilizing micropillar indentation splitting technique, providing a locally resolved characterization of the sample in contrast to the conventional Vickers indentation test (macroscopic characterization).[237] The microscopic fracture toughness of Al-LLZO was measured to be ∼0.99 MPa $m^{1/2}$, which was slightly lower than the Vickers fracture toughness (1.19 MPa $m^{1/2}$). The Young's modulus and hardness were measured to be ∼145.6 GPa and ∼8.5 GPa, respectively. Yu et al. reported the elastic properties of LLZO based on a combination of first-principles calculations, acoustic impulse excitation and nanoindentation measurements.[242] Generally, the oxide electrolytes possess very high Young's moduli (100−200 GPa), indicating a high stiffness in these materials, while their fracture toughness needs to be improved. It is worth noting that anisotropy should be considered in evaluating the mechanical properties of SSEs. For example, LATP electrolyte was found to possess noticeable anisotropic mechanical properties (Figure 18d). The Young's modulus of LATP decreased from ∼150 GPa for the basal plane to ∼107 GPa for the prismatic plane, whereas the hardness decreased from 10.0 GPa for the basal plane to 5.5 GPa for the prismatic plane.[238] Attention should be paid to the anisotropic behavior of SSEs since the thickness of the SSE layer in high-energy density solid-state batteries has been suggested to be less than 30 μm and the orientations of electrolyte particles, if not in controlled manner, are likely to cause inhomogeneity and affect the overall structural integrity of the SSE layer under stress.[238,243]

Sulfide electrolytes are generally less stiff than oxide electrolytes. It has been proposed that soft sulfide electrolytes with low elastic modulus would be ideal candidates for solid-state batteries, accommodating the significant stress induced by the volume changes of electrode materials during change and discharge.[188] The Young's modulus of hot-pressed $xLi_2S\cdot(100-x)P_2S_5$ (mol.%) electrolyte was measured to be in the range of 18−25 GPa, and it decreased with decreasing Li_2S content.[244−246] The Young's modulus of cold-pressed pellets were even lower than that of the hot-pressed sample and in the range of 14−17 GPa. A simple room-temperature pressure sintering process was demonstrated to offer dense SSE pellets and intimate solid−solid contacts between SSEs and active materials, which is beneficial for producing solid-state batteries. The mechanical properties of β-Li_3PS_4 were investigated from theoretical (first-principles calculations) and experimental (nanoindentation and bulk acoustic techniques) routes, both giving very low bulk and shear moduli.[208,247] The soft texture of sulfide electrolyte may arise from the low bond dissociation energy per unit volume and the ion packing density.[244] However, such soft sulfide electrolytes have been shown to be brittle with low resistance to fracture.[246]

The mechanical properties of antiperovskite electrolytes have not been assessed experimentally yet. Nevertheless, efforts from theoretical investigation have provided some valuable information. Deng et al. obtained the elastic constants (C_{ij}) of 23 typical inorganic electrolytes including antiperovskite electrolytes with the help of first-principles calculations based on DFT.[208] The simulated elastic constants of the antiperovskite electrolytes are positive, which meets the "Born stability criteria" and indicates the mechanical stability of unstressed antiperovskite structures.[248] The elastic properties, including Young's, shear and bulk modulus (K, which measures the compressibility of a material and gives the required hydrostatic pressure to trigger a volume change in that material), and Poison's ratio of the electrolytes have been further calculated based on the elastic constants (some of results are summarized in Table 3). The Young's, shear and bulk modulus of the prototypical Li_3OCl antiperovskite electrolyte were calculated to be 99.7, 41.4, and 55.7 GPa, respectively, which are larger than that of most sulfide electrolytes but smaller than that of the traditional oxide electrolyte, suggesting a medium stiffness in the antiperovskite electrolyte under the order of thiophosphate < antiperovskite < NASICON < garnet < perovskite. Moreover, antiperovskite with a larger cation or anions was found to have lower elastic moduli; the Young's modulus of Na_3OCl and Li_3OBr are 60.2 and 92.8 GPa, respectively, which are smaller than that of Li_3OCl (99.7 GPa). This trend is coincident with the result found in sulfide electrolytes based on experimental observation.[244] It might be employed to tune the mechanical properties of antiperovskite electrolytes for enhanced performance.

It is worth noting that the calculated shear modulus of the Li_3OCl antiperovskite reaches 41.4 GPa, which is much higher than the stability threshold suggested by Monroe and Newman (∼8.5 GPa) and indicates a potential to block lithium dendrites. In comparison, the shear modulus of proton-rich counterpart $Li_2(OH)Cl$ was estimated to be 17.4 GPa (Table 3), which is significantly lower than that of Li_3OCl but still higher than the stability threshold. However, the criterion was originally developed for polymer separators and its accuracy has not been determined conclusively for inorganic SSEs, particularly after the observation of Li penetration in several SSEs, like LLZO that possesses very high shear modulus (68.9 GPa).[233,249,250] Recent theoretical investigation suggested that significant softening in elastic properties could occur in nanoscale regions near grain boundaries of SSEs. The grain boundary shear modulus could be 50% smaller than in bulk regions because of the large excess volume associated with a grain boundary.[251,252] As a result, lithium dendrite would penetrate the electrolytes through grain boundaries in spite of the high shear modulus in the bulk regions of SSEs. This may explain the reported Li penetration in $Li_2(OH)Cl$ electrolyte and short-circuit of the Li/SSE/Li cells at 65 °C.[104] Interestingly, similar cells could cycle repeatedly without detectable lithium dendrite over much longer time at 195 °C,[117] probably due to reduced shear modulus of the Li anode (in molten state) at the elevated temperature, or reduced grain boundaries or pores in the electrolyte after heating the cells. Further study is needed to assess these factors.

The ratio of bulk modulus to shear modulus (K/G) is an indication of the ductility/brittleness of a material and a low K/G value is usually associated with a high brittleness.[253] The calculated K/G values of antiperovskites are generally low (∼1.4 compared to >2.0 for sulfide electrolytes and 1.6−2.0 for most oxide electrolytes),[208] indicating that antiperovskites electrolytes are more brittle than the traditional sulfide and oxides electrolytes. Therefore, caution should be displayed during the electrolyte thin-film processing and cell assembly.

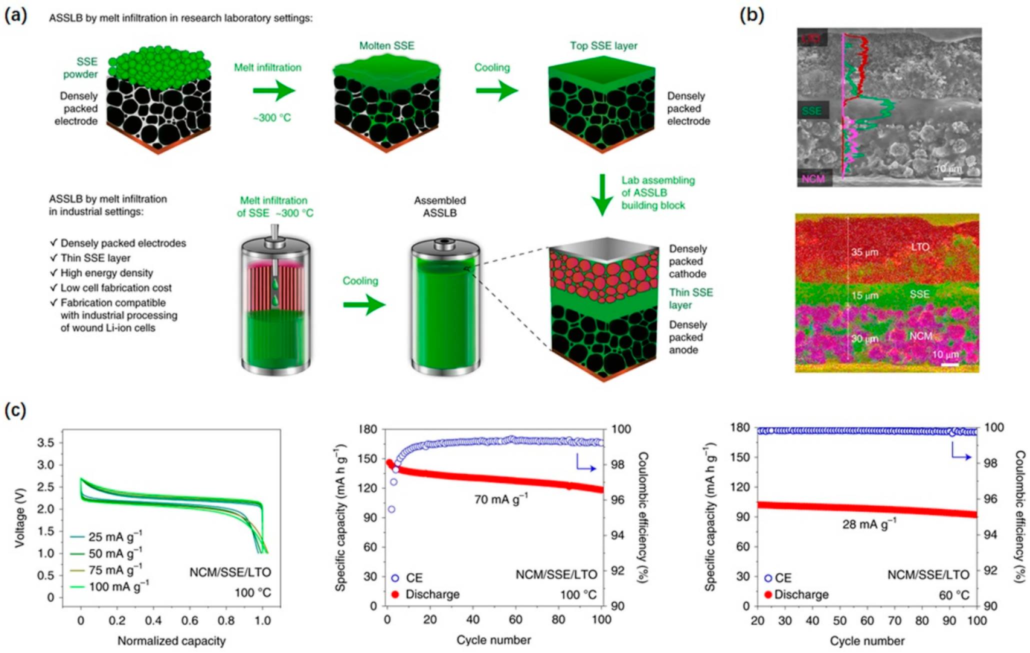

Figure 19. (a) Schematic illustration of the melt-infiltration process for solid-state batteries using low-melting antiperovskite electrolyte. (b) Scanning electron microscopy (SEM) image and EDS mapping of the cross-section of a solid-state cell with an NCM cathode and LTO anode prepared by the melt-infiltration technique. (c) Electrochemical performance of the cell. Reproduced with permission from ref 15. Copyright 2021 Springer Nature Limited.

7. SOLID-STATE BATTERIES USING ANTIPEROVSKITE ELECTROLYTES

7.1. Cell Engineering and Performance

Solid-state batteries generally consist of a stack of three components (cathode layer, SSE layer, and anode layer). The layers require intimate contact between particles and therefore fabrication involves densification and integration of electrolyte/active materials.

Cold-pressing of dry components has been the most common route to fabricate solid-state batteries at the lab scale. In this method, powder samples (electrolyte or composite electrode materials) are pressed in molds to form pellets. For example, antiperovskite $Li_2(OH)Br_{0.98}F_{0.02}$ electrolyte powders were pressed on a preformed $LiFePO_4$ cathode and attached with a lithium metal anode, forming an all-solid-state battery. The full cell exhibited an initial discharge capacity of 99.5 mAh/g at 0.2 C and maintained a capacity of 68.0 mAh/g after 30 cycles when operating at 80 °C.[254] The initial discharge capacity is relatively low compared to the value obtained in liquid-electrolyte-based cells (around 158 mAh/g), which might arise from the limited utilization of active materials in the solid-state cell due to low densification and thus incomplete contact between the rigid active material and SSE particles. High densification can be achieved by applying heat during pressing, such as that observed through the spark plasma sintering (SPS) process. It has been found that SPS managed to increase the relative density of pressed antiperovskite Na_3OBr pellets to 96% from 89% of cold-pressing sample, which reduced the interfacial impedance by 3 orders of magnitude.[185] An increase in the active material utilization and a decrease in the ohmic resistance can be anticipated in the resultant full cells. This phenomenon can be understood from the viewpoint of the mechanical properties of antiperovskite electrolytes that generally possess high elastic modulus, as discussed in the last section. Therefore, antiperovskite electrolytes cannot be easily densified at low temperatures by simple pressing, in contrast to the softer materials such as sulfides and borohydrides that can afford rather high densification after cold-pressing. Simultaneous application of pressure and heat is effective in increasing the densification of electrolyte pellets or cell stacks; however, such processes are prohibitively costly and have limitations on the thickness and area of the pressed sample, limiting its utilization in the pursuit of thin, large-area electrolyte membranes that are required for constructing high-energy density solid-state batteries.[243]

Vapor deposition methods are able to deliver high-quality membranes with controlled thicknesses, high densification, and intimate solid−solid contacts. This route has been industrialized to produce solid-state thin film microbatteries that possess high energy and powder densities, excellent cycle life and extremely low self-discharge rate.[255,256] By using layer-by-layer PLD techniques, researchers have built all-solid-state batteries with graphite, antiperovskite Li_3OCl and $LiCoO_2$ films as the anode, electrolyte and cathode, respectively.[138] The resultant Li_3OCl electrolyte film was shown to possess large grain size, which reduces the overall resistance and leads to higher ionic conductivity as compared to the bulk pressed counterpart (2.0×10^{-4} S/cm vs 5.8×10^{-7} S/cm). The full cells were tested between 2.2 and 4.2 V at a current density of 10 mA/g at room temperature, and they gave an initial discharge capacity of ~120 mAh/g (calculated from the weight of $LiCoO_2$ cathode), which was nearly 83% of the measured capacity of $LiCoO_2$ in liquid electrolyte system (~145 mAh/g). This suggests improved active material utilization in the full cells prepared via vapor deposition compared to the above cold-pressed cells. Despite of the aforementioned advantages, the scalability of bulk solid-state batteries through this route still remains doubtful due to the costs involved.[257]

A cost-effective route for building bulk solid-sate batteries with reasonable densification/contact is the wet (solvent-based) method, which has been verified in many sulfide electrolyte-based systems.[146,147] In this route, SSE powders are dispersed or dissolved in a volatile solvent and then deposited as a uniform coating layer on the surface of active electrode materials after evaporating the solvent, which provides improved solid−solid contact area. Moreover, the slurry containing electrolyte or electrolyte/electrode composite can be coated on a substrate and produce large-area thin films by using a similar process to lithium-ion battery electrode manufacturing. The different layer components can be well-integrated after layer-by-layer slurry coating and drying. Antiperovskite $Li_{2.99}Ba_{0.005}O_{1+x}Cl_{1-2x}$ glass electrolyte was introduced into a porous substrate (fiberglass sheet or recycled paper sheet) by researchers through the wet method, forming an electrolyte membrane without grain boundaries.[16] The thickness of the electrolyte membrane was 0.06 mm in this report, which can be controlled by the selection of substrate. The membrane was pressed between a lithium anode and composite cathode containing sulfur, SSE and carbon (47:43:10 wt %), forming an all-solid-state Li−S cell. Interestingly, the resultant Li−S cell showed a significantly greater discharge capacity than the capacity of the sulfur cathode. The authors proposed a different mechanism from the conventional electrochemical process, claiming that the lithium metal with a high-energy Fermi level can be plated on the cathode current collector with a low-energy Fermi level. The voltage of the cell was proposed to be determined by a cathode redox center having an energy between the Fermi levels of the anode and that of the cathode current collector. However, there exists controversy about this explanation considering the risk of first-law violation.[258]

Many antiperovskite electrolytes have relatively low-melting points,[11,86,87] which is an important feature that differentiates antiperovskite electrolytes from other electrolytes such as oxide and sulfide electrolytes. This feature makes it possible to engineer antiperovskite pellets or membranes with high densities as well as desired thicknesses through melt casting.[117] Analogous to the wet method, melt casting could also promote intimate solid−solid contact, ensuring excellent ion transport in the bulk. Very recently, researchers took advantage of the low-melting point of antiperovskite $Li_{1.9}(OH)Cl_{0.9}$ electrolyte (∼300 °C), and fabricated all-solid-state batteries with $LiNi_{0.33}Mn_{0.33}Co_{0.33}O_2$ (NCM111) cathodes and both $Li_4Ti_5O_{12}$ (LTO) and graphite anodes.[15] The $Li_{1.9}(OH)Cl_{0.9}$ electrolytes were melted and infiltrated into thermally stable electrodes at elevated temperatures, and then solidified during cooling, forming integrated electrode/electrolyte stacks after the simple one-step procedure, as shown in Figure 19a and b. The cell possessed low interfacial resistance and demonstrated small voltage hysteresis between charge and discharge curves (e.g., 0.1 V at 25 mA/g for the LTO/SSE/NCM111 cells) and reasonable rate capability at an elevated temperature of 100 °C. It delivered a high capacity of ∼150 mAh/g and a considerable capacity retention of over 80% after 100 cycles (Figure 19c). The cell also worked well at a reduced temperature of 60 °C, delivering similarly small voltage hysteresis and high capacity retention during cycling. As demonstrated by this example, the melt casting route could deliver high-quality membranes or integrated stacks like the wet method does; moreover, it is more environmentally friendly (solvent free). This method opens a new avenue for the low-cost fabrication of bulk solid-state batteries with improved volumetric energy density. It should be noted that the engineering and understanding of full solid-state batteries using antiperovskite materials as SSEs is just in its initial stages. With more research efforts being devoted to this direction, it can be expected that higher performance solid-state batteries using antiperovskite materials may be developed.

7.2. Antiperovskite Electrolyte/Electrode Interfaces

As discussed above, antiperovskite electrolytes have been studied in the past years, in which reasonable ionic conductivity has been achieved. However, there is only a few reports demonstrating the full cell performances using antiperovskite electrolytes. One of the major obstacles is the interface instability in antiperovskite electrolyte-based solid-state batteries. For example, solid-state batteries consisting of graphite/Li_3OCl/$LiCoO_2$ can be prepared with excellent solid−solid contacts through the PLD method. However, the cell capacity decayed quickly to 55% after only 20 cycles.[138] It is considered that the capacity fading is attributed to the irreversible side reactions at the interfaces between the electrodes and antiperovskite electrolytes. To realize the high-performance solid-state batteries, there should exist stable interfaces between SSEs and electrodes. Generally, the interfacial stability of solid-state batteries includes electrochemical, chemical, mechanical, and thermal stabilities in addition to interface wettability. In this section, we will focus on the electrochemical and chemical stabilities that have been investigated in the antiperovskite electrolyte related interfaces.

The interfaces in solid-state batteries are categorized according to three types, (i) thermodynamically stable interfaces, (ii) mixed ionic−electronic conducting interphases (MCI) with both electronic and ionic conductivity, and (iii) solid electrolyte interphases (SEI) with negligible electronic conductivity. Generally, the type (i) and (iii) interfaces are expected to be beneficial toward the stable electrochemical performances of solid-state batteries. The thermodynamic stability at the interface depends on the electrochemical windows of the SSEs, which has been discussed in the previous section. The electrochemical stability windows of the SSEs present the capability for resisting oxidation and reduction during the extraction or insertion of the alkali ions and electrons. Ideally, the SSEs are expected to have a wide electrochemical stability window with high operating oxidation potential for high-voltage cathodes and low reduction potential toward alkali metal anodes. Computational methodologies have been developed to examine the thermodynamics of the formation of resistive interfacial phases.[201,213,259] According to the calculations, the prototypical oxide electrolyte, garnet LLZO, has a relatively wide electrochemical window of 0.07−3.2 V. Therefore, it is predicted to be stable toward Li metal but may be oxidized at high voltage. Most of the sulfide-based solid-state batteries have narrow stability windows based on the simulation results, which are approximately 2−2.5 V. For example, LGPS is predicted to have an electrochemical stability window of 1.7−2.1 V. The electrochemical windows of typical antiperovskite electrolytes such as Li_3OCl and Na_3OBr are approximately 0−3 V and 0−2 V, respectively. Accordingly, these proton-free antiperovskite electrolytes are thermodynamically stable with Li and Na metal anodes. The electrochemical window of proton-rich counterparts is narrower (for example, 0.82−3.15 V for $Li_2(OH)Cl$[212]). The cathode/antiperovskite electrolyte interface is one of the biggest issues due to their low oxidation potentials. The antiperovskite electrolytes will be decomposed at ∼3 V. In this case, antiperovskite electrolytes are unstable against most of the popular cathode materials, such as $LiCoO_2$, $LiFePO_4$, $LiMnO_2$, $LiNiO_2$, NMC, etc. However, there is no

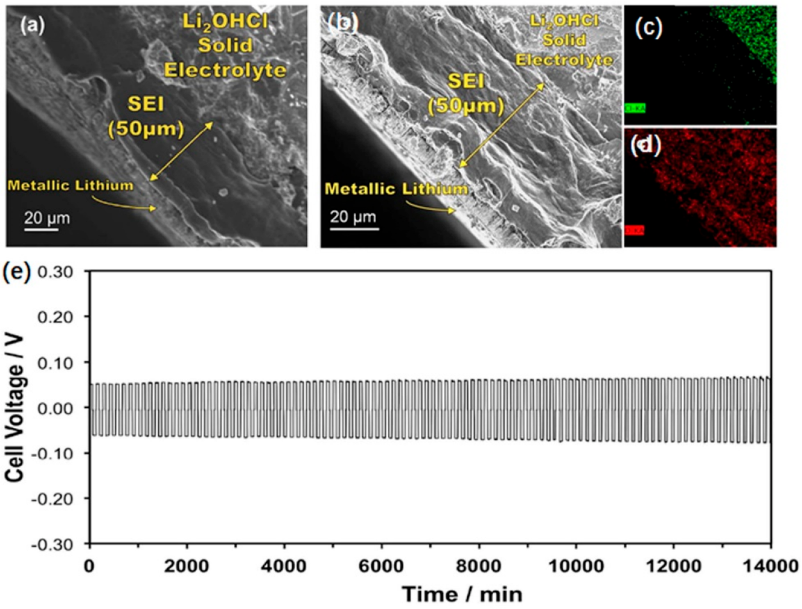

Figure 20. SEM images of a Li/$Li_2(OH)Cl$/Li symmetric cell showing a cross-section of the SEI (a) after 40 and (b) after 160 charge/discharge cycles. Correlating EDX mapping of (b): chlorine in green (c) and oxygen in red (d). (e) The cyclability of the Li/$Li_2(OH)Cl$/Li symmetric cell at 195 °C with a current density of 1.0 mA/cm^2. Reproduced with permission from ref 117. Copyright 2016 American Chemical Society.

study to report the electrochemical reaction mechanism between the antiperovskite electrolytes with different cathode materials. More efforts should be attempted to understand the interface between the antiperovskite electrolytes and electrodes (both Li metal and cathode) beyond the thermodynamic calculations.

Besides the electrochemical stability, chemical reactions may also occur on the interface between the SSEs and electrodes of cathode and anode. The chemical instability is driven without external potential and is considered as a slow, static process. At the cathode/SSE interface, the chemical stability between the cathode electrode and SSEs have been predicted by theoretical simulations. Both the cathode and SSEs may be decomposed upon contact and without external potential. For example, most of the sulfide SSEs are chemically unstable against oxide cathodes such as $LiCoO_2$ and NMC due to their high chemical potential. The oxide SSE/cathode interfaces are regarded as more stable, however, elemental interdiffusion has been observed for both oxide and sulfide SSE/cathode interfaces. Particularly, the high-temperature sintering process for oxide SSEs will aggravate the interfacial diffusions/reactions between oxide SSEs and cathode electrodes. Furthermore, the space charge layer is another factor that contributes to the large resistance between the SSEs and cathodes. Li-ions are expected to transfer between cathode and SSEs under different chemical potentials. The Li-ion redistribution on the interface will lead to a carrier depletion zone across the SSEs, which will increase the resistance and hinder the Li-ion transport during the electrochemical process. At the anode interface, the metallic Li (or Na) is highly reactive and can react with most SSEs. For example, SSEs with high oxidation state elements such as Nb^{5+}, Ge^{4+}, and Ti^{4+} are reduced when placed in contact with Li metal, resulting in electrochemical performance decay. Proton-free antiperovskite electrolytes, such as Li_3OCl and Na_3OBr, are known to be stable with metal anodes. This stability can be understood to arise from the anions being present in their lowest oxidation state. Proton-rich antiperovskites, on the other hand, are prone to react with molten Li (or Na) metal at elevated temperatures to form new antiperovskites through the deprotonation reaction as described in Section 4, but this reaction has not been observed at room temperature most likely due to the sluggish reaction kinetics. The chemical stability between antiperovskite and cathode materials has not been investigated and is expected to be explored further.

The interfacial properties and ionic transport between antiperovskite Li_3OCl SSEs and Li metal anode have been investigated by first-principles calculations and AIMD simulation.[260] On the basis of the results, the interface between antiperovskite Li_3OCl electrolyte Li metal is stable, which is electronically insulating and Li-ion conductive. The Li-ion mobilities across the interface are predominantly along the interfacial boundary and the Li ionic conductivity at the Li_3OCl side of the L_3OCl/Li interface is 1 order of magnitude higher than that of bulk Li_3OCl. The simulation results provide detailed information on the interfacial stability and properties between antiperovskite Li_3OCl electrolyte and Li metal. Besides the computational results, some experimental works were also reported to prove the stability between the antiperovskite electrolytes and Li metal anodes. A Li/Li_3OCl/Li symmetric cell with PLD deposited Li_3OCl electrolyte showed an interesting self-stabilizing phenomenon in the first 20 charge−discharge cycles at room temperature.[137] Afterward, the interface can be stabilized with constant overpotential. Another work by the same group also showed that the overpotential of Li/Li_3OCl/Li symmetric cell increased gradually during the first few cycles and then remained approximately stable up to 72 h.[138] Furthermore, the interface stability against Li for the proton-rich antiperovskite $Li_2(OH)Cl$ electrolyte was studied.[117] As shown in Figure 20, the symmetric Li/$Li_2(OH)Cl$/Li cell showed great cyclability with molten lithium anode when the cell was run at 195 °C. A stable interlayer, with a thickness of 50 μm, was further identified between the electrolyte and lithium anode. The in situ generated interlayer had a higher concentration of oxygen. It was proposed that the antiperovskite $Li_2(OH)Cl$

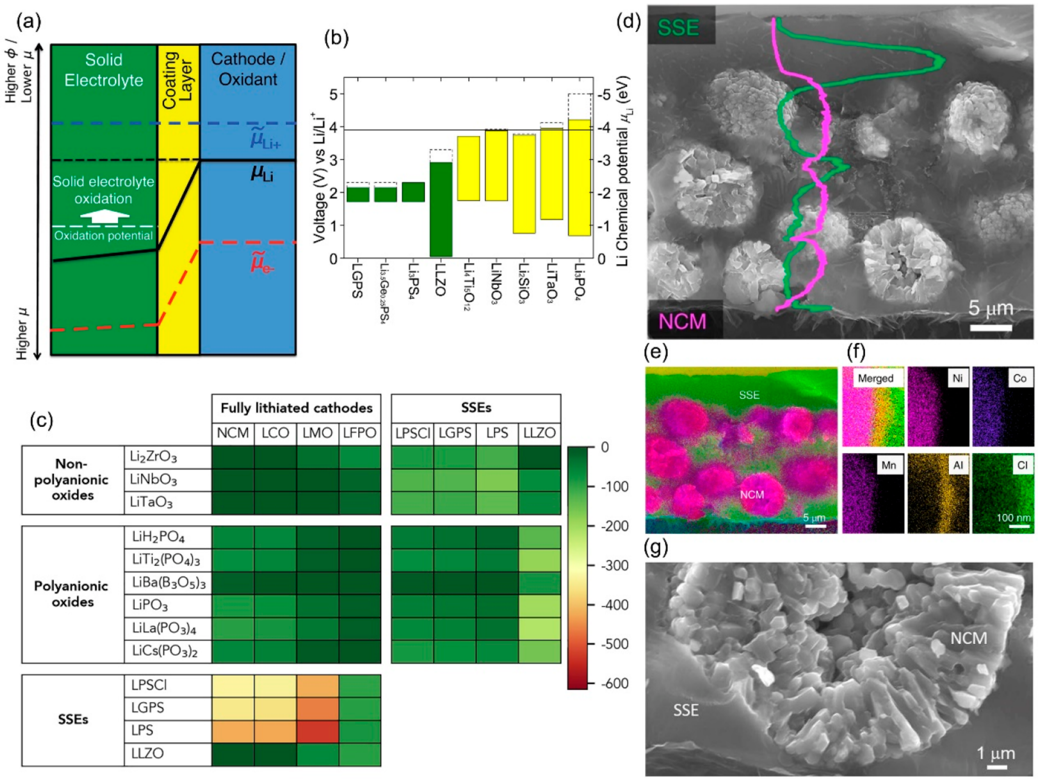

Figure 21. Interface engineering at cathode/electrolyte. (a) Reaction energies at fully lithiated cathode/electrolyte, fully lithiated cathode/coating, and coating/electrolyte interfaces. (b) Some common interfacial materials. Reproduced with permission from ref 201. Copyright 2015 American Chemical Society. (c) Polyanionic oxides as coating layers for cathode materials. Reproduced with permission from ref 264. Copyright 2019 Elsevier B.V. (d) SEM cross-section of an Al_2O_3-coated NCM^{111} electrode infiltrated with antiperovskite $Li_{1.9}(OH)Cl_{0.9}$ electrolyte; vertical EDS line scans show Ni (from NCM, purple) and Cl (from electrolyte, green). (e) EDS mapping the melt-infiltrated NCM^{111} electrode, where the purple color represents combined Ni/Co/Mn (from NCM) and the green color represents Cl (from electrolyte). (f) High-resolution EDS mapping of the NCM−electrolyte interface. (g) SEM image of the NCM−electrolyte interface after 100 charge−discharge cycles of the cells. Reproduced with permission from ref 15. Copyright 2021 Springer Nature Limited.

electrolyte reacted with molten lithium to form Li_2O, LiCl and H_2 gas under chemical and electrochemical reactions. The LiCl product was located closer to the $Li_2(OH)Cl$ electrolyte, while Li_2O was closer to the lithium anode and constituted the bulk of the interlayer. This interphase layer can prevent further reactions between $Li_2(OH)Cl$ and Li metal while maintaining good electrochemical cycling. On the basis of the reported works, antiperovskite electrolytes are quite stable against Li metal. However, a deeper understanding of the composition of the interface and mechanism of formation are expected to be further explored.

Additionally, due to the good interface stability between antiperovskite electrolytes with lithium metal, the electrolytes have been employed to construct composites with oxide or sulfide electrolytes that are less stable with lithium metal anodes. For example, antiperovskite Li_3OCl electrolyte was mixed with LLZTO electrolyte to form a composite electrolyte, in which the Li_3OCl electrolyte acting as a binder, filler, and promoted a continuous ionic conductive network among LLZTO particles.[261] The resultant solid-state $LiFePO_4$/LLZTO-Li_3OCl/Li cell delivered stable specific capacities as high as 157.5 mAh/g and 85.7 mAh/g at 0.05 and 0.5 C, respectively. A similar concept of garnet-based bulk-type all-ceramic lithium battery has also been demonstrated, in which the antiperovskite $Li_{2.985}B_{0.005}OCl$ electrolyte was used as sintering agent and was uniformly coated on both $LiCoO_2$ and LLZO.[262] The $Li_{2.985}B_{0.005}OCl$ displayed a low melting point and high ionic conductivity, which provided fast Li^+ transportation in the cathode and lead to low interfacial resistance. In another work, the antiperovskite $Li_2(OH)Br$ electrolyte was applied as additives for $Li_7P_3S_{11}$ sulfide electrolyte and the mixed electrolytes were obtained by high energy ball-milling method.[263] The as-prepared $Li_7P_3S_{11}$−$Li_2(OH)Br$ composite electrolytes showed improved electrochemical performances with good cycling stability and extended electrochemical window. With 10% $Li_2(OH)Br$, the composite electrolyte presented the highest ionic conductivity of 4.4×10^{-4} S/cm at room temperature. Full cell using $LiNi_{0.6}Mn_{0.2}Co_{0.2}O_2$ (NMC622) as the cathode material exhibited a discharge capacity of 135 mAh/g at room temperature. These studies revealed that the antiperovskite electrolytes can be used not only as the electrolyte layer but also to modify the interface between other electrolytes and electrode materials due to their excellent stability against lithium metal anodes.

7.3. Interface Modification Approaches

As discussed, the major limitation of antiperovskite electrolytes is at the cathode/electrolyte interface, especially for high voltage cathode materials. To address the issues associated with the cathode/electrolyte interface, interfacial coatings have been proposed as effective strategies. Although this area has not been explored in antiperovskite electrolytes, researchers can start from drawing lessons from the studies of other electrolyte systems, such as sulfide or oxide electrolytes. The basic requirements for the interfacial coating materials on cathode/

electrolyte interface share some similarities, including the need for uniform and conformable coatings, good ionic conductivity, wide electrochemical windows, and suitable mechanical properties. The electrochemical windows of the interfacial coating materials should bridge the potential gap between antiperovskites electrolytes and cathode materials, which are usually in a range between 3 and 4 (5) V. Theoretically, the coating layers mitigate the low Li chemical potential μ_{Li} from the cathode material applied on the electrolytes, as shown in Figure 21a. In this case, the oxidation and delithiation of the electrolytes at the cathode interface can be prevented, and the oxidation potential of the electrolyte is extended by the artificial coating layer.[201] Therefore, the oxidation potential of the antiperovskites electrolytes can be effectively extended from 3 V to over 4 V. On the basis of this principle and the calculated results, some popular oxides might be promising candidates for interface engineering, such as $LiNbO_3$, Li_2SiO_3, $LiTaO_3$, Li_3PO_4, Li_2ZrO_3, et al. Most of these coating layers have electrochemical windows with reduction potentials of 0.7−1.7 V and oxidation potentials of 3.7−4.2 V (Figure 21b). Moreover, computational screening has shown the possibility for polyanionic oxides as coating layers for cathode materials,[264] as shown in Figure 21c. Compared to the nonpolyanionic oxide, the polyanionic oxides, including LiH_2PO_4 and $LiTi_2(PO_4)_3$, meta-phosphates $LiPO_3$, $LiLa(PO_3)_4$, and $LiCs(PO_3)_2$, and borate $LiBa(B_3O_5)_3$, generally have higher oxidation limits (>4.5 V). Moreover, metal oxide coatings and polyanionic coatings provide a much more stable interface with oxide cathodes than most of the SSEs, as shown in Figure 21c. In addition to oxide coatings, the fluoride compounds, including LiF, Li_3AlF_6, etc., display even higher electrochemical window up to 6 V, which have also been reported as coating layers for solid-state batteries.

Different methods have been attempted to obtain a good interfacial coating for SSBs, such as the wet-chemical method, spray coating, PLD, and ALD.[265] The wet-chemical method is one of the most widely used and cheapest methods to fabricate the coating layer on cathode materials for either liquid battery and solid-state batteries. Different coating materials, such as metal oxide, and oxide SSEs, have been synthesized by the wet-chemical method for solid-state batteries.[266−271] However, one of the shortfalls of the wet-chemical method is that the thickness, morphology, and homogeneity of the coating layer cannot be precisely controlled. Another concern related to the wet-chemical method is the presence of solvent and the postannealing process at high temperatures. PLD, as a physical vapor deposition method, has been employed to deposit the coating of Li_3PO_4 for solid-state batteries with smaller interfacial resistances, enhanced cycle life and improved capacities.[272−274] However, one disadvantage of the PLD method is that it is challenging to achieve conformal coatings and the thickness of the PLD is usually quite thick (up to 50 nm), which can potentially impede ionic transport.

Among the various approaches, ALD and molecular layer deposition (MLD) are the most promising methods to modify the interface. MLD has been further developed by replacing the oxidizing precursors used in ALD (e.g., H_2O, O_2, O_3) with organic linkers or molecular fragments into the film. ALD/MLD is a self-limiting process in which the growth of the film is dictated by gas−solid surface reactions.[275−277] ALD/MLD techniques show unique properties, including excellent uniformity and conformity, precisely controlled thickness, and low growth temperatures.[278−280] Different interfacial materials listed above, such as $LiNbO_3$, Li_2SiO_3, $LiTaO_3$, Li_3PO_4, $LiZrO_2$, LiF, and Li_3AlF_6, have been successfully developed by ALD.[281−287] ALD/MLD techniques have received increasing attention to solving the interfacial issues for batteries, including liquid and solid systems. The ALD coatings (such as Li_3PO_4, $LiTaO_3$, $LiNbO_3$) were deposited on different cathode materials and then used in different solid-state batteries. For example, we reported the ALD $LiNbO_3$ coating for Ni-rich layered oxide $LiNi_{0.8}Mn_{0.1}Co_{0.1}O_2$ (NMC811) cathode used in sulfide-based solid-state batteries with LGPS as SSE. As a result, the ALD $LiNbO_3$ layer can effectively prevent the reactions between NMC cathode and LGPS SSEs.[288] Furthermore, a dual-functional Li_3PO_4 (LPO) modification was designed for Ni-rich layered oxide cathodes in sulfide-based solid-state batteries with significantly improved performances.[289] However, one of the major concerns for ALD/MLD is the practicality of large-scale deposition for industrial applications. To address this concern, large-scale spatial ALD systems have been proposed and developed. For example, the rotary reactor and fluidized bed reactor have been successfully developed for the large scale ALD/MLD deposition on powders with the capabilities of processing material from kilogram to ton's levels.[290−295]

Currently, there is no systematic study focusing on the understanding and modification of the interface between antiperovskite electrolytes and cathode electrodes. However, the interfacial challenges still remain based on the calculated electrochemical windows. To achieve stable cathode/antiperovskite electrolyte interfaces, interfacial engineering approaches, such as wet-chemical, PLD, ALD, and MLD, are expected to play an important role based on the experience from other electrolyte systems (like sulfides). In a recent work by Xiao et al., NCM cathodes were coated by a thin layer of Al_2O_3 through ALD, which offered an excellent wetting of the NCM cathodes with the antiperovskite electrolyte after melt-infiltration and avoid further reactions between cathode and electrolyte (Figure 21d−f).[15] This resulted in minimal interfacial impedance at the interface and promoted a tight connection between the cathode and the SSE even after prolonged cycling of the cells (Figure 21g).

8. ADVANCED CHARACTERIZATION TECHNIQUES FOR ANTIPEROVSKITE ELECTROLYTE STUDY

The development of new antiperovskite electrolytes for solid-state battery applications relies on the thorough understanding of material structures and interface evolution at multiple scales, which can be assisted through the use of a variety of characterization techniques. XRD, scanning electron microscopy (SEM) and transmission electron microscopy (TEM) are the most frequently used techniques in laboratories, however each of them has their own limitations in delivering structural information. In this section, we will focus on some advanced characterization techniques that are less used but stand out as necessary complements to the conventional techniques in the study of antiperovskite electrolyte materials and solid-state batteries.

8.1. Solid-State Nuclear Magnetic Resonance

Solid-state nuclear magnetic resonance (ss-NMR) spectroscopy is a powerful method for probing the chemical environments of various magnetically active elements. It is ideal for investigating the small changes in local structure. On the one hand, magic angle spinning (MAS) NMR is used to average out internal interactions (e.g., dipolar and quadrupolar couplings between nuclei) of the anisotropic solids, which is beneficial for collecting

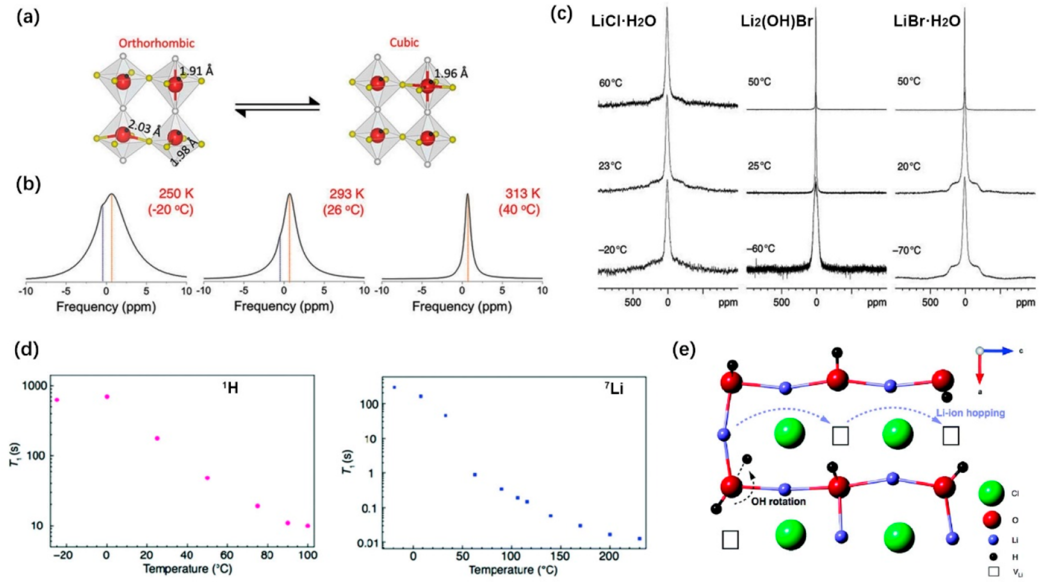

Figure 22. (a) Structure transformation of $Li_2(OH)Cl$ (Li, yellow; V_{Li}', white; O, red; H, dark gray). (b) ^{7}Li MAS NMR of $Li_2(OH)Cl$ with ^{1}H decoupling at 250, 293, and 313 K at 15 kHz spinning speed. (c) ^{7}Li NMR spectra of $LiCl·H_2O$, $Li_2(OH)Br$ and $LiBr·H_2O$ showing no, a smooth and a sharp transition into a cubic phase, respectively. (d) T_1 value of ^{1}H and ^{7}Li for $Li_2(OH)Cl$. (e) Schematic representation of the Li-ion hopping mechanism in the cubic $Li_2(OH)Cl$. The OH^- groups point toward Li vacancies. Li-ion hopping occurs via these vacancies, denoted by the blue dashed arrows. Rotation of the OH^- groups occurs as a result of a nearby Li ion hopping to an adjacent site, denoted by the black dashed arrow. (a,b) Reproduced with permission from ref 159. Copyright 1999−2021 John Wiley and Sons, Inc. (c) Reproduced with permission from ref 39. Copyright 1999−2021 John Wiley and Sons, Inc. (d, e) Reproduced with permission from ref 158. Copyright 2018 The Royal Society of Chemistry.

high-resolution spectra similar to that seen in the liquid-based NMR. This can provide a quantitative measurement for the phase and material structure evolutions at the atomic level versus the time scale. On the other hand, the NMR resonance is very sensitive to movements of diffusive ions, such as Li ions and protons while completely excluding the effect of grain boundaries. Therefore, ss-NMR can be used to precisely analyze the dynamic feature of movable species in solid-state electrolytes via designing variable-temperature (VT) experiments or saturation recovery and spin-lock pulse sequences. Specifically, the motional narrowing effect of NMR line shapes for nuclei reflects the Li-ion dynamics in different crystal structures, while the spin−lattice relaxation time (T_1) indicates the rate of energy transfers from an excited state to equilibrium under the influence of neighboring environment (coordination, vacancy, etc.).

With respect to the crystal structure of antiperovskites, ss-NMR was demonstrated to witness the phase evolution of antiperovskites based on the line shape analysis of ^{7}Li NMR spectra. Principally, the quadrupole ^{7}Li can present two spin transitions: central transition ($+1/2 \leftrightarrow -1/2$) and satellite transition ($\pm 3/2 \leftrightarrow \pm 1/2$), leading to narrow and broad resonance peaks, respectively. When the local symmetry at the site of the ^{7}Li is virtually cubic, the broad component is absent. The phase transformation of $Li_2(OH)Cl$ can be illustrated in Figure 22a, and the traced ^{7}Li MAS NMR spectra in different intermediate stages are displayed in Figure 22b.[159] A broad spectrum at −20 °C is assigned to the environment of featured Li atoms in the orthorhombic structure, which consists of at least two overlapping peaks at −0.481 and 0.708 ppm. Upon heating to 40 °C, only one single ^{7}Li resonance peak at 0.697 ppm remains, whereas the broad flank peaks vanish. The occurrence of one single peak corresponds to two near equivalent Li sites per unit cell with similar Li−O bond lengths of 1.96 Å, which agree well with the cubic symmetry obtained from the corresponding XRD analysis. Schwering et al. also investigated the ^{7}Li NMR spectra of $LiCl·H_2O$, $Li_2(OH)Br$, and $LiBr·H_2O$ in the temperature range of −70 to 60 °C.[39] As shown in Figure 22c, $LiCl·H_2O$ shows no phase transformation in the entire temperature range, because the board spectra (peak width 120 kHz) keep steady in the wide temperature range. Comparatively, an obvious line shape change occurs at each designated temperature for the bromide counterpart ($LiBr·H_2O$). In the spectra taken at temperatures above 30 °C (cubic phase), the quadrupolar coupling pattern collapses and a narrow signal shows up. The phase transformation in the case of $Li_2(OH)Br$ is not confirmed, but somewhat cubic environment of the ^{7}Li nucleus is presented between −60 and 50 °C.

VT line shape analysis and T_1 measurement for ^{7}Li are the two most commonly used NMR-related techniques to analyze the dynamics in antiperovskites as in other Li-ion conductors,[39,228,296] while the largest characteristic of using ss-NMR for antiperovskite electrolytes is identifying the dynamics of proton correlating with Li-ion motion. The related research history can retrospect to Chihara et al. early in 1969.[99] They used VT ^{1}H and ^{7}Li NMR to study the disorder in lithium iodide monohydrate ($LiI·H_2O$) material that shares a similar cubic structure with the antiperovskite $Li_{2+x}H_{1-x}OX$ (X = Cl, Br). The H_2O molecule is found that reorient at the body-center position with an activation energy of 13.4 kcal/mol and Li^+ ions diffuse among face-center positions with an energy barrier of 13.5 kcal/mol. Moreover, the motions of H_2O and Li^+ ions are not independent but correlate with each other. The mutually pulling mechanism between H_2O and Li^+ ions is believed to show some similarity compared with the recent findings by Song et al. that presence of proton in $Li_{2+x}H_{1-x}OCl$ ($0 \leq x < 1$) yields significantly improved Li^+ ionic conductivity.[105] In 1997, Eilbracht et al. also confirmed a similar dynamical orientational disordering of OD^- in $Li_2(OD)X$ (D: deuterium, X = Cl, Br) with VT ^{2}H NMR.[157]

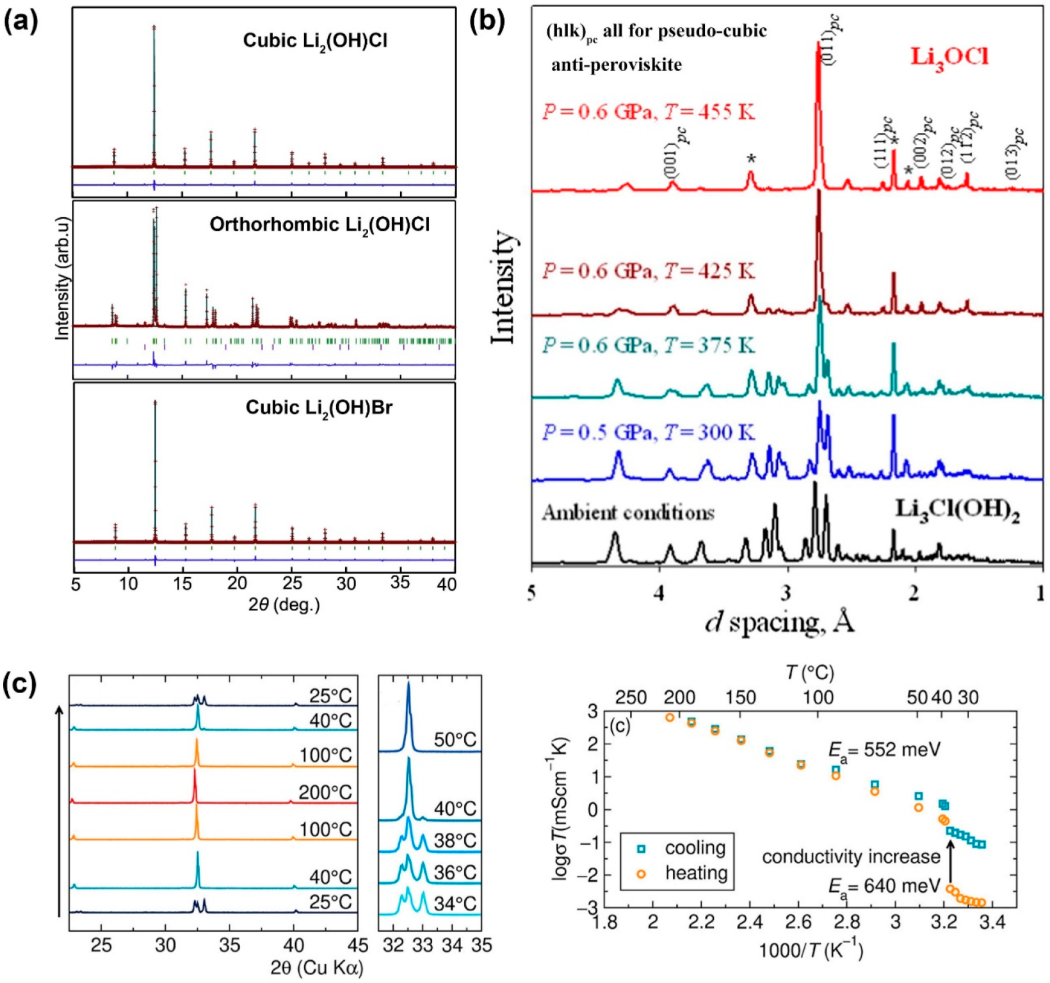

Figure 23. SR-XRD for antiperovskite electrolytes: (a) $Li_2(OH)Cl$ and $Li_2(OH)Br$. Reproduced with permission from ref 305. Copyright 2020 Elsevier Inc. (b) In situ SR-XRD under high P-T conditions. Reproduced with permission from ref 142. Copyright 2014 Elsevier B.V. (c) Temperature-dependent SR-XRD patterns of $Li_2(OH)Cl$ and the correlated ionic conductivity change as a function of temperature. Reproduced with permission from ref 304. Copyright 2020 American Chemical Society.

However, there was no comprehensive examination of Li^+ ion diffusion correlating with proton dynamics in the H-containing antiperovskites (e.g., representative $Li_{2-x}OH_{1-x}Cl$ electrolytes, $0 \leq x < 1$) until 2018. Dawson et al. first applied ^1H, ^2H and ^7Li ss-NMR spectroscopy in combination with AIMD simulation to indicate a fast Li-ion diffusion but ruled out the contribution of long-range proton diffusion.[158] Namely, the proton motion is verified as localized, but Li-ion mobility occurs in the long-range. They obtained the ^1H and ^7Li T_1 values of $Li_2(OH)Cl$ along with elevated temperatures as displayed in Figure 22d, respectively. The rapid change of T_1 between 0 and ∼60 °C for both cases indicates the phase change from orthorhombic to cubic intermediately. Comparing the ^1H and ^7Li T_1 values at 100 °C, there is an order of magnitude difference, which suggests high Li-ion mobility in $Li_2(OH)Cl$ but limited proton mobility. To further investigate the local behavior and mobility of the OH^- groups, the author studied deuterated $Li_2(OH)Cl$ electrolyte using VT MAS ^2H NMR from −19 to 110 °C. Although the known phase transition occurs at 35−40 °C, the almost unchanged ^2H NMR spectra indicate the OH^-/OD^- groups are still static. Even at 63 °C, accomplishment of phase change cannot trigger the movement of OH^-/OD^- groups. Till to 69 °C, significant line shape change of ^2H NMR spectrum took place, suggesting the mobility change of OH^-/OD^- groups. However, the single relatively broad (2.7 kHz) resonance of deuteron at 110 °C indicate that the movement is from OH^-/OD^- groups (H/D rotation around the oxygen) rather than a free deuteron. Combining these NMR results with AIMD simulation, the authors concluded that the mobility of the Li^+ ions in $Li_2(OH)Cl/Li_2(OD)Cl$ is intimately connected to the position of the OH^-/OD^- groups within the structure. They proposed the Li-ion hopping mechanism in cubic $Li_2(OH)Cl$ as illustrated in Figure 22e. The transport of Li^+ ions is based on Li vacancies, while this hopping can influence the position of the OH^- groups. When a Li vacancy is filled, the H will rotate around the oxygen, repositioning itself so that it can always point toward a vacancy. As such, the greatest degree of freedom and movement is achieved.

Recently, Song et al. reported a more detailed analysis of the T_1 data to study the role of H in the representative $Li_2(OH)Cl$ antiperovskite.[159] They used a biexponential function with two different relaxation times T_1 (fast) and T_1 (slow) to perform a good fitting for T_1 of both ^1H and ^7Li. The temperature range is ∼40 to 80 °C, covering four commonly studied stages of this antiperovskite: Stages I/II - orthorhombic, Stage III - structural transformation to tetragonal/cubic, and Stage IV - cubic structures. For the ^7Li, both fast and slow relaxation rates R_1 (the reverse of T_1) continuously increase through all stages. At temperatures above 0 °C, the fast relaxation component becomes dominant, and the T_1 becomes a single-exponential with the relaxivity R_1 (Li, fast) in Stage IV. This suggests that translational motion of Li^+ occurs at high temperatures in Stage IV (small peak with of ~0.7 kHz starting at 40 °C), and the Li^+ ions travel through vacancies in the structure, thus averaging out various relaxations that exist at low temperature (Stages I−III). In contrast, for T_1 relaxation of ^1H, even at the highest temperature, the curve remains nonexponential, which means protons in the OH remaining on a fixed lattice. In addition, the authors correlated the dynamic analyzed by measurement of T_1 with the ionic conductivity via EIS to further illustrate the motional feature of protons. The activation energies derived from ^7Li relaxation rates are 0.326 and 1.51 eV for cubic (Stage IV) and orthorhombic structures (Stage III), respectively. They are in good agreement with the EIS results. Nevertheless, the activation energies of the ^1H-T_1 relaxation are lower by a factor of 2−3 in both aforementioned structures, demonstrating a more localized nature of the ^1H motion.

8.2. Synchrotron Radiation X-ray Techniques

Synchrotron radiation (SR) is a powerful tool for studying the fundamental working mechanism of battery materials.[297] The SR X-ray techniques have various advantages of high flux and brilliance, highly collimated light with tunable energies, and a broad spectrum of the X-ray beams. These properties enable its use for characterization tools involving scattering, spectroscopy, and imaging techniques, which are used to obtain structural and chemical information with different levels of spatial and temporal length scales.[298−300] The SR X-ray techniques have been developed in the recent year to characterize the physical and chemical properties of the battery materials.[301,302]

SR-XRD is one of the most widely used methods to study the structural and chemical information of electrolytes, including the antiperovskite electrolytes. The working principle of SR-XRD is similar to the conventional XRD. However, the SR-XRD has better resolution and intensity using a synchrotron beam along with enhanced signal strength with reduced test time, which enables the development of time-resolved XRD and in situ/operando XRD in synchrotron beamlines.[297] The SR-XRD was developed to analyze the phase transition and crystal structure of the antiperovskite electrolytes.[130,303,304] For example, the SR-XRD patterns of $Li_2(OH)Cl$ and $Li_2(OH)Br$ are shown in Figure 23a with their refinement results.[305] The cubic $Li_2(OH)Cl$ and $Li_2(OH)Br$ are shown to possess cubic antiperovskite crystal structure models with the space group $Pm\bar{3}m$. The SR-XRD patterns of orthorhombic $Li_2(OH)Cl$ was refined with an orthorhombic cell with the space group $Pmc2_1$. Moreover, the detailed lattice parameters for $Li_2(OH)Cl$ and $Li_2(OH)Br$ were refined from the SR-XRD results.

In addition to the regular SR-XRD measurements, in situ XRD has been developed to study the phase and crystal structure of antiperovskite electrolytes under different conditions. We have applied in situ and real-time SR-XRD to study the formation processes of Li_3OCl and Li_3OBr antiperovskite under high P-T conditions,[142] as shown in Figure 23b. A $Li_3Cl(OH)_2$ phase was formed at 425 K and 0.6 GPa using the Li_2O:LiCl precursors with a 1:1 molar ratio. After heating to 425 K, the cubic $Pm\bar{3}m$ structure can be observed from the diffraction line, indicating the formation of Li_3OCl antiperovskite. The temperature-dependent SR-XRD has been further developed to study the phase change of antiperovskite $Li_2(OH)Cl$ upon heating and cooling,[304] as shown in Figure 23c. It was observed that the $Li_2(OH)Cl$ displayed a phase transition near 38 °C from an orthorhombic phase to the cubic phase. As a result, the ionic conductivity change from 1.2×10^{-8} S/cm at 37 °C to 1.4×10^{-6} S/cm at 39 °C. Upon cooling through the phase transition, the conductivity decreases abruptly by about a factor of 10 at the same transition temperature. Furthermore, in situ SR-XRD upon compression and decompression at different pressures was also designed to study the phase change of antiperovskite Na_3OBr and Na_4OI_2 electrolytes.[306] The results showed that both cubic Na_3OBr and tetragonal Na_4OI_2 are stable up to 24.3 GPa upon compression. After decompression, the sample returns to a similar cell volume observed at ambient conditions. It is believed that the stable structure of Na_3OBr and Na_4OI_2 under pressure is due to the pseudorigid building blocks consisting of ONa_6 octahedron.

As discussed in the previous section, the interfacial stabilities, including electrochemical, chemical, mechanical, and thermal stabilities, significantly affect the performances of the solid-state batteries. To comprehensively understand the interfacial reactions and phenomenon, many typical SR X-ray techniques have been employed, such as high-energy X-ray photoelectron spectroscopy (HEXPS), X-ray absorption near edge structure (XANES), and extended X-ray absorption fine structure (EXAFS). These techniques are developed to investigate the chemical/electrochemical interfacial reaction mechanisms of solid-state batteries. For example, XPS is an effective approach to study the chemical state, overall electronic structure and state of the interfaces while providing quantitative information of elemental compositions. Compared to the traditional XPS, faster measurements and better resolution can be obtained with the use of bright synchrotron radiation. Moreover, by tuning the photon energy by SR, a tunable depth sensitivity of 2−50 nm can be achieved to perform nondestructive depth-resolved analysis. The usage of SR-HEXPS has been demonstrated to study the interfacial stability of NASICON type electrolyte LATP against the Li metal anode.[307] Furthermore, X-ray absorption spectroscopy (XAS) is widely used in the investigation of the local geometric and electronic structure of materials, especially for battery application. The full XAS spectrum is typically divided into two regions consisting of XANES and EXAFS, in which the XANES data provides quantitative or qualitative information on oxidation states, site symmetries and covalent bond strength of specific elements and EXAFS can be used to provide information on the local atomic structure of the probed elements.[297] Ex-situ and in situ XANES have also been developed to study the interfacial reactions for polymer, oxide, sulfide, and halide SSBs.[288,307−309] To date, there is almost no study on the development of SR X-ray spectroscopy (such as XPS and XAS) techniques for the study of interfacial behaviors in antiperovskite solid-state batteries. However, as described in the previous sections, the chemical/electrochemical mechanism between the antiperovskite electrolytes with different electrode materials is poorly understood, in which the SR X-ray techniques can provide a promising opportunity for future studies.

8.3. Neutron Diffraction

One of the most important features of neutron diffraction for the study of SSEs, particularly for antiperovskite electrolyte investigation, is the capability of detecting low-Z elements (or light elements, such as H, Li, O, and F) that cannot be detected by X-ray (synchrotron) techniques with sufficient accuracy. The reason lies in the fact that X-rays are electromagnetic waves, also called photons, and interact with electrons of atoms via the

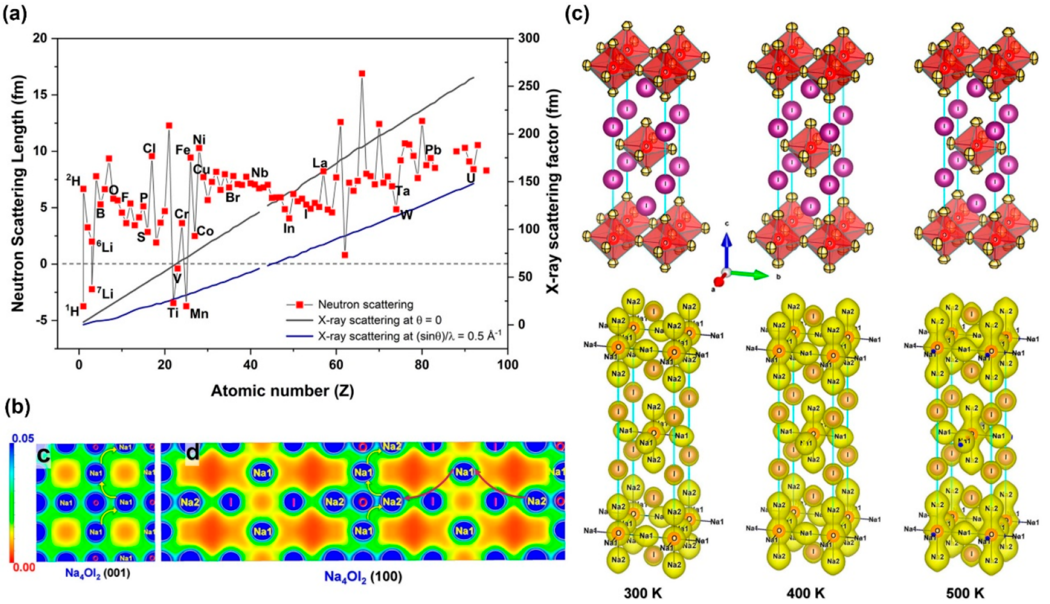

Figure 24. (a) Neutron scattering length of some selected elements. The atomic scattering factors for X-rays are also displayed for comparison. The values of the scattering factors for X-rays vary with Bragg angle θ (results for $\theta = 0$ and $(\sin\theta)/\lambda = 0.5$ Å^{-1} are given here), whereas they keep the same at all angles for neutron. (b) 2-D version of the nuclear density distributions of Na_4OI_2 at 500 K. The arrows show two potential pathways in Na_4OI_2. (c) Upper panel shows the Na_4OI_2 crystal structures at 300, 400, and 500 K. The thermal ellipsoids are drawn with 80% probability; Lower panel shows the nuclear density distributions of Na atoms in Na_4OI_2 at 300, 400, and 500 K from MEM analysis at the iso-surface level of 0.03 fm/Å^3. Reproduced with permission from ref 87. Copyright 2016 American Chemical Society.

electromagnetic interaction. The scattering power of X-rays (and neutrons) by an atom is measured by the coherent scattering cross section σ ($\sigma = 4\pi b^2$, where b is the coherent scattering length). The X-ray coherent scattering length is proportional to the atomic number Z, as shown in Figure 24a. The X-ray signals of light elements are weak and easily overwhelmed by signals from high-Z elements if present in the sample. In contrast, thermal neutrons are subatomic particles and interact directly with atomic nuclei through short-range nuclear forces.[310,311] The neutron scattering length of the atoms is rather random and can be either positive or negative, while the values of the scattering length for the low-Z elements are of the same order of magnitude as those of the high-Z elements (Figure 24a).[312] Another important feature of neutron diffraction is the ability to distinguish nearby elements, which arises from the discernible difference between the neutron scattering lengths of the neighboring atoms. This is of particular importance for the study of transition metal elements Fe, Co, Ni, and Mn that constitute most cathode materials and possess very similar X-ray scattering lengths.

The utilization of neutron diffraction for the study of antiperovskite electrolytes has been performed mainly for two purposes. One is the need for structure interpretation. For example, antiperovskite M_3HCh (M = Li, Na; Ch = S, Se, Te) electrolytes were designed and synthesized via high-pressure methods,[143] as discussed in Section 4. The idea behind this design was to exploit the large polarizability of hydride (H^-) together with chalcogenide (Ch^{2-}) to construct antiperovskites with substantially soft anionic sublattices, and therefore to lower the migration batteries for Li^+/Na^+ transport and to achieve high ionic conductivity. The proposed antiperovskites are very interesting from the structural point of view as most of the antiperovskite electrolytes have been obtained with divalent anions (oxide/sulfide) at the octahedral B sites and with larger monovalent cations occupying the dodecahedra A sites (Figure 2a). However, the monovalent cation proposed in this work is H^-, which is smaller than the divalent anions S^{2-}, Se^{2-}, and Te^{2-},[313] and raised questions on the formability of these compounds and the subtle anion arrangement. Time-of-flight (TOF) powder neutron diffraction was employed to elucidate these issues after a preliminary structure analysis by SR-XRD in this work. It was revealed that the Li^+, H^-, and S^{2-} ions of the Li_3HS compound fully occupied their respective crystallographic sites with Li^+ at the $3d$ (1/2, 0, 0) Wyckoff position and H^- at the $1a$ (0, 0, 0) site and S^{2-} at the $1b$ (1/2, 1/2, 1/2) site of the cubic antiperovskite structure ($Pm\overline{3}m$ space group). The possibility of antisite disorder between H^- and S^{2-} was examined by Rietveld refinement assuming the anion exchange; however, it resulted in the full occupancy of H^- at the B site with $R_{wp} = 1.37\%$ and $R_{Bragg} = 6.64\%$, confirming the fully ordered anion sublattices.[143]

Another key point of using neutron diffraction is to determine the diffusion pathway of lithium/sodium ions in target compounds. This can aid our fundamental understanding of the conduction mechanism and help guide the rational design of new electrolytes with faster ionic conduction. The investigation is usually conducted by collecting neutron diffraction data in variable temperatures and then analyzing the nuclear density from the Bragg intensity by the maximum entropy method (MEM).[314,315] A series of in-depth studies by research teams led by M. Yashima, Y. Zhao, and A. Yamada et al. have illustrated the process of utilizing this method to investigate the motion of lithium ions in SSEs or electrode materials, and clearly demonstrated the conversion from thermal vibration of atoms to continuous diffusion.[316−318] Investigation of the diffusion pathways in antiperovskite electrolytes was exemplified by the representative antiperovskite Na_3OBr and the layered antiperovskite Na_4OI_2 derivative.[87] Na_3OBr crystallizes in a standard cubic antiperovskite structure with the $Pm\overline{3}m$ space group, while Na_4OI_2 is a tetragonal antiperovskite with a $I4/$

mmm space group. The latter species is a layered intergrowth K_2NiF_4-type structure, characterized by the "Na_3OI" antiperovskite slabs and the "NaI" rock-salt layers. Although the geometric information of the two compounds is clear, the potential difference in the diffusion pathways of sodium ions in the compounds was not known before this study. Neutron diffraction investigation of Na_3OBr and Na_4OI_2 was carried out at 300, 400, and 500 K and the nuclear density distribution maps were deducted from MEM analysis. The results showed that the sodium ions in Na_3OBr transport among nearest Na^+ sites and vacancies along the edges of Na_6O octahedra. Since all the sodium atoms in Na_3OBr are crystallographically equivalent, the diffusion path is three-dimensional (Figure 12d and e). In contrast, there are two inequivalent sodium positions in Na_4OI_2, resulting in three possible diffusion pathways: Na1−Na1, Na1−Na2 and Na2−Na2, as shown in Figure 24b and c. The sodium ions at Na1 position display an elliptic nuclear density in the *ab* plane, while sodium ions at Na2 position show an elliptic nuclear density along the *c* direction, suggesting potential diffusion in the *ab* plane as well as along the *c* axis. The latter route is of minor probability considering the largest migration distance (4.7627(3)Å for Na2−Na2, compared with 3.3042(4) and 3.2603(1) Å for Na1−Na1 and Na1−Na2, respectively). Nevertheless, the MEM results also gave the polarized nuclear density distribution of I^- ion, which overlaps with Na2 ion and can act as a pathway of a negative charge center and facilitate sodium diffusion along the *c* axis.[87] The investigation of diffusion pathways in the antiperovskites by MEM has promoted deeper understanding of ionic diffusion mechanism in the new structures and showed promising potential for guiding further structural manipulations.

Moreover, neutrons feature high penetrability due to the interaction with atomic nuclei instead of the electrons, making them particularly suitable for in situ investigation of the chemistry and structure dynamics in model cells or even practical full cells.[319−325] For example, in situ neutron diffraction was employed to investigate the nonequilibrium states in commercial $LiFePO_4$ cathode under operating condition.[326] The electrochemical cell for this investigation was prepared by rolling a stack of Celgard (insulator), $LiFePO_4$ cathode paste on aluminum foil, Celgard (separator) and lithium metal anode, followed by insertion of the stack into a 9 mm diameter vanadium can. Copper wire was attached with the lithium anode and the aluminum current collector of the cathode. Electrolyte made of a 1/1 vol% mixture of deuterated EC and DMC was added to the vanadium can, followed by sealing with wax. The cell was placed in a neutron beam of wavelength $\lambda = 2.4053(1)$ Å and the patterns were collected every 5 min for 67 h between $16° \leq 2\theta \leq 136°$, during which the cell was cycled within selected voltage range under galvanostatic mode. The neutron diffraction signals displayed extreme sensitivity to bulk crystallographic changes in the $LiFePO_4$ cathode and revealed the simultaneous occurrence of solid-solution and two-phase reactions after deep discharge.[326] This investigation presented a great example for the experimental probe of the nature of the transition interface in electrode materials even in a closed operating system, demonstrating the advantage of neutron diffraction for in situ characterization. Although there has been no report on the in situ neutron investigation of solid-state cells based on antiperovskite electrolytes so far, the feasibility for this study can be anticipated.

It is noteworthy that the neutron scattering properties of all elements must be examined before running the diffraction experiments, particularly for the in situ cell investigation in which the existence of particular elements in component materials of electrode/electrolyte or in sealing parts can result in low-quality neutron signals. For example, hydrogen exists in many antiperovskite electrolytes and organic cell components; however it has a large incoherent neutron scattering cross section and usually causes high background intensity in neutron diffraction patterns. Vanadium(V) has a near-zero scattering length, as shown in Figure 24a. For this reason, vanadium is often used for making sample containers. Some elements such as boron (B), cadmium (Cd), and gadolinium (Gd) have very large absorption cross sections for thermal neutrons, making it extremely difficult to collect useful information through normal neutron diffraction from samples containing these neutron absorbers. Therefore, it is highly recommended to check the neutron coherent, incoherent and absorption cross-section of each element before neutron diffraction experiments. Table 4 summarizes the neutron scattering properties of some commonly used elements for antiperovskite electrolytes and related solid-state batteries, which can be used as a quick check. Complete information can be found in ref 312. Isotope substitution can be considered when coming across the above situations. For instance, substitution of deuterium for hydrogen provides a way to accurate refinement of the atomic position as the incoherent scattering of the neutron can be reduced to a much lower level with deuterium. This also holds for the substitution of ^7Li for ^6Li in a natural mixture of lithium isotopes (natural abundance: ^6Li-7.5%, ^7Li-92.5%) when high-quality neutron diffraction data are needed.

Table 4. Neutron Coherent Scattering Lengths and Coherent, Incoherent, and Absorption Cross-Section of Some Elements

element	coherent scattering length (10^{-12} m)	coherent cross-section (10^{-24} cm^2)	incoherent cross-section (10^{-24} cm^2)	absorption cross-section (10^{-24} cm^2)
H	−3.7390	1.7568	80.26	0.3326
D (^2H)	6.671	5.592	2.05	0.000519
Li	−1.90	0.454	0.92	70.5
^7Li	−2.22	0.619	0.78	0.0454
B	5.30	3.54	1.70	767(8)
C	6.6460	5.550	0.001	0.0035
N	9.36	11.01	0.50	1.90
O	5.803	4.232	0.0008	0.00019
F	5.654	4.017	0.0008	0.0096
Na	3.63	1.66	1.62	0.530
Mg	5.375	3.631	0.08	0.063
Al	3.449	1.495	0.0082	0.231
Si	4.1491	2.1633	0.004	0.171
P	5.13	3.307	0.005	0.172
S	2.847	1.0186	0.007	0.53
Cl	9.5770	11.526	5.3	33.5
Mn	−3.73	1.75	0.40	13.3
Fe	9.45	11.22	0.40	2.56
Co	2.49	0.779	4.8	37.18
Ni	10.3	13.3	5.2	4.49
Br	6.795	5.80	0.10	6.9
I	5.28	3.50	0.31	6.15

9. SUMMARY AND PERSPECTIVES

Since the early discovery of the Ag_3SI antiperovskite electrolyte and the ionic conductivity breakthrough achieved with Li_3OCl

(Br), a number of lithium and sodium ionic conductors with antiperovskite structures have been developed to date. The electrolytes have displayed highly desirable stability against alkali metal anodes, rapid preparation and scalability in addition to reasonably high conductivities. These properties have been rarely obtained with the traditional SSEs. Therefore, antiperovskite electrolytes stand out as a promising new family of inorganic conductors for solid-state batteries and are attracting ever-growing interests. Reviewing the state-of-the-art SSEs in this field, we find that the number of reported antiperovskite electrolytes is still limited compared with the traditional perovskite, LISICON, argyrodite or garnet type electrolytes, and the relevant full-cell studies are even rarer. Nevertheless, the flexibility of the antiperovskite structure enables substantial chemical tailoring, such as substitution at any of the A, B, and X positions of X_3BA antiperovskite structures with a wide range of ions and valences, presenting plenty of opportunities for optimizing the electrolyte composition and the electrochemical performance. For example, halogen anions in the A sites (e.g., Cl^-, Br^-) can be replaced by superhalogen anions (e.g., BH_4^-, BF_4^-, NO_2^-) with higher ionization potential, potentially increasing the electrochemical stability window of the antiperovskite electrolytes in addition to the enhanced ionic conduction triggered by the rotational motion of superhalogen anions. The anionic sublattice can be softened by partial or complete replacement of the anions on A or B sites with other anions with larger polarizability, which is anticipated to lower the migration barrier for cation transport and high ionic conductivity. It is also feasible to design new deficient antiperovskites with a formula such as $X_5B_2A_2$ in which the ordering of X vacancies may significantly influence the overall ionic conductivity.

In addition to the structure manipulation to enhance the ionic conduction or structural stability of antiperovskite electrolytes, breakthroughs can also be found elsewhere. Herein, several points of particular importance are listed for reference.

(1) The conducting mechanism in antiperovskite electrolytes should be identified, with particular attention to the proton effects and potential anion diffusion. Most reported antiperovskite electrolytes are extremely sensitive to moisture and tend to decompose into proton-rich compounds or hydrates, which may introduce undesirable proton or electron conduction. Moreover, anions with relatively small ionic radii are able to diffuse within solids at elevated temperatures (e.g., F^- in perovskite $NaMgF_3$). F^- and Cl^- diffusion in antiperovskite electrolytes may affect the output of solid-state batteries and interfacial properties and therefore should be excluded or utilized properly.

(2) The stability of antiperovskite electrolytes toward low potential anodes is one of the major advantages of antiperovskite electrolytes over others. It is known that the stable interface between electrolyte and electrode arises either from the intrinsic thermodynamical stability of the electrolyte or from the formation of interphases with negligible electronic conductivity. Although the current results based on experimental and theoretical calculations have indicated considerable chemical and electrochemical stability for antiperovskite electrolytes against lithium or sodium metal anodes, the interfacial phase(s) between antiperovskite electrolytes and Li/Na anode has not been clearly identified, which limits our understanding of the stabilization mechanism at the anode interface. Detailed characterization of the electrolyte-anode interface is therefore essential.

(3) According to the experimental results based on cyclic voltammetry testing, antiperovskite electrolytes have very large electrochemical stability windows that cover the upper-voltage limits of current cathode materials. However, the calculated windows are limited by the low oxidation potentials and are much smaller than the experimental results. The discrepancy mainly arises from the inaccuracy in conventional testing methods using a Li/SSE/inert metal (e.g., stainless steel, Pt) semiblocking electrode configuration in which the contact area between electrolyte and inert metal is very limited. Therefore, it is necessary to characterize the true electrochemical stability window through modified methods before full cell studies are carried out. Potential interfacial reactions and composition of the byproducts on the electrolyte−cathode interface also require further clarification.

(4) Coating high-voltage cathodes with thermodynamically stable layers is a potential solution to the interface issues arising from the chemical or electrochemical reactions between cathode and antiperovskite electrolytes. Although several promising inorganic coatings have been identified for traditional sulfide electrolyte-based systems, they are not necessarily compatible with the new antiperovskite electrolytes. Systematic investigation on the composition and thickness of the coating layer is still needed. Moreover, the coating layers are believed to be passivated during the initial electrochemical cycles. The phase and structure evolutions of the coating layers during extraction or insertion of the alkali ions are a topic of interest, and they are of particular importance for evaluating the long-term cycling stability.

(5) The mechanical properties of each component in all-solid-state batteries are crucial for prolonged cycling. This is especially important for batteries made from antiperovskite electrolytes that possess large stiffness and low ductility. The dynamic volume change of active electrode materials during change and discharge is likely to interrupt the integrity of the electrode or the contact between different layers when using SSEs. Application of external pressure on all-solid-state full cells has been generally adopted to maintain a reasonable solid−solid contact during cycling, even for cells with soft sulfide electrolytes. Antiperovskite electrolytes cannot deform as easily as their sulfide counterparts, and are more likely to lose connectivity in ionic and electronic conduction pathways after the volume change of electrode materials. In this regard, studies on the structural integrity of electrode and electrode/electrolyte assembly during cycling would be important.

(6) Antiperovskite electrolytes have demonstrated great potential for scalable manufacturing of electrolyte thin films, electrodes and full cells using the melt infiltration method. It is worth noting that thermal residual stresses may be established between the electrode materials and electrolytes upon cooling from the melt due to the difference in thermal expansion between them. Such stresses may influence the ionic conductivity in electrolytes or electrode materials and can also cause mechanical failure during operation. Moreover, antiperovskite electrolytes become more reactive in the molten state at

elevated temperatures and may react with the electrode materials (or the coating layer) and the conducting carbon additives. High-impedance layers may form as a result and affect the output of full cells. More effort is required for understanding the complex interfacial mechanics and chemistries.

ASSOCIATED CONTENT

Supporting Information

The Supporting Information is available free of charge at https://pubs.acs.org/doi/10.1021/acs.chemrev.1c00594.

Table summarizing electronic conductivity and calculated band gap of several representative Li/Na-ion electrolytes (PDF)

AUTHOR INFORMATION

Corresponding Authors

Xueliang Sun − *Department of Mechanical and Materials Engineering, University of Western Ontario, London, Ontario N6A 5B9, Canada;* orcid.org/0000-0003-0374-1245; Email: xsun9@uwo.ca

Yusheng Zhao − *Shenzhen Key Laboratory of Solid State Batteries, Guangdong Provincial Key Laboratory of Energy Materials for Electric Power, Academy for Advanced Interdisciplinary Studies, Southern University of Science and Technology, Shenzhen 518055, China*; Email: zhaoys@sustech.edu.cn

Ruqiang Zou − *Beijing Key Laboratory for Theory and Technology of Advanced Battery Materials, School of Materials Science and Engineering, Peking University, Beijing 100871, China;* orcid.org/0000-0003-0456-4615; Email: rzou@pku.edu.cn

Authors

Wei Xia − *Department of Mechanical and Materials Engineering, University of Western Ontario, London, Ontario N6A 5B9, Canada; Shenzhen Key Laboratory of Solid State Batteries, Guangdong Provincial Key Laboratory of Energy Materials for Electric Power, Academy for Advanced Interdisciplinary Studies, Southern University of Science and Technology, Shenzhen 518055, China*

Yang Zhao − *Department of Mechanical and Materials Engineering, University of Western Ontario, London, Ontario N6A 5B9, Canada;* orcid.org/0000-0002-4148-2603

Feipeng Zhao − *Department of Mechanical and Materials Engineering, University of Western Ontario, London, Ontario N6A 5B9, Canada*

Keegan Adair − *Department of Mechanical and Materials Engineering, University of Western Ontario, London, Ontario N6A 5B9, Canada*

Ruo Zhao − *Shenzhen Key Laboratory of Solid State Batteries, Guangdong Provincial Key Laboratory of Energy Materials for Electric Power, Academy for Advanced Interdisciplinary Studies, Southern University of Science and Technology, Shenzhen 518055, China*

Shuai Li − *Shenzhen Key Laboratory of Solid State Batteries, Guangdong Provincial Key Laboratory of Energy Materials for Electric Power, Academy for Advanced Interdisciplinary Studies, Southern University of Science and Technology, Shenzhen 518055, China*

Complete contact information is available at: https://pubs.acs.org/10.1021/acs.chemrev.1c00594

Author Contributions

$^{\perp}$W.X., Y.Z., and F.Z. contributed equally.

Notes

The authors declare no competing financial interest.

Biographies

Wei Xia received his Ph.D. degree in Adv. Mater. and Mechanics from Peking University in 2016, under the supervision of Prof. Ruqiang Zou. He is currently a research assistant professor in the Academy for Advanced Interdisciplinary Studies at Southern University of Science and Technology, and a visiting Professor and an Associate Fellow in Prof. Xueliang (Andy) Sun's Group at the University of Western Ontario. Dr. Xia has previous experience in the battery industry through work at battery R&D center of a terminal manufacturer. His research interests include solid-state batteries, lithium-ion batteries, electrocatalysis, and functional porous materials.

Yang Zhao is an Assistant Professor in the Department of Mechanical and Materials Engineering at the University of Western Ontario, Canada. Dr. Zhao received his B.S. and M.S. degrees from Northwestern Polytechnical University (Xi'an, China) in 2011 and 2014, respectively. He obtained his Ph.D. degree under the supervisor of Dr. Xueliang (Andy) Sun from the University of Western Ontario in 2018. Then he had his postdoc training at Western and the Advanced Light Source of Lawrence Berkeley National Laboratory with Dr. Jinghua Guo in 2019−2020. His research interests focus on Adv. Mater. and interfaces for energy storage applications, and synchrotron-based X-ray techniques.

Feipeng Zhao is a Postdoctoral Associate (PDA) at Western University. He received his Ph.D. degree in Mechanical and Materials Engineering from Western University, Canada, in August 2021. He obtained his B.S. degree and M.S. degree in Materials Science from Soochow University in 2014 and 2017, respectively. He is working on the synthesis and characterizations of advanced inorganic solid-state electrolytes and interfaces for high-performance all-solid-state batteries.

Keegan Adair received his B.Sc. in Chemistry from the University of British Columbia in 2016. He is currently a Ph.D. candidate in Prof. Xueliang (Andy) Sun's Group at the University of Western Ontario, Canada. Keegan has previous experience in the battery industry through internships at companies including E-One Moli Energy and General Motors R&D. His research interests include the design of advanced Li metal anodes and nanoscale interfacial coatings for battery applications.

Ruo Zhao is currently a Research Associate from Prof. Yusheng Zhao's group in Southern University of Science and Technology, China. She received her Ph.D. degree in 2019 from the Department of Materials Science and Engineering, Peking University, China. Her research interests include the synthesis of metal−organic frameworks and Li-rich antiperovskites as well as their applications in solid-state electrolytes, lithium-ion batteries, and electrocatalysts.

Shuai Li received her Ph.D. degree in condensed matter physics from the Institute of Physics, CAS in 2013, under the supervision of Prof. Liquan Chen. She joined the group of Prof. Yusheng Zhao at University of Nevada Las Vegas from 2013 to 2016 as a postdoctoral fellow, and then joined Huawei Technologies as a senior engineer from 2016 to 2018. She became a research associate professor at Southern University of Science and Technology (SUSTech, Shenzhen) in April 2018. Her research interests focus on antiperovskite materials and solid-state lithium batteries.

Ruqiang Zou is currently a Professor of Materials Science and Engineering, Peking University, China. He received his Ph.D. degree in Engineering in 2008 from Kobe University and the National Institute of Advanced Industrial Science and Technology, Japan. He held the JSPS Younger Scientist during his doctoral course and a Director's Postdoc Fellow at Los Alamos National Laboratory from 2008 to 2010. His research interests focus on the controllable preparation and application of hierarchically porous functional materials for energy and environmental application.

Yusheng Zhao is currently a Chair Professor at Department of Physics and the president of Academy for Advanced Interdisciplinary Studies, South University of Science and Technology. He received his Bachelor's and Master's degrees from Peking University, and Ph.D. degree from the State University of New York at Stony Brook. Prof. Yusheng Zhao is the director of Guangdong Provincial Key Laboratory of Energy Materials for Electric Power, and the director of Shenzhen Key Laboratory of Solid State Batteries. His current research interests focus on the design, synthesis, and mechanism study of Li-rich antiperovskites as solid-state electrolytes, and their applications in solid-state batteries.

Xueliang Sun is a Canada Research Chair in Development of Nanomaterials for Clean Energy, Fellow of the Royal Society of Canada, and Canadian Academy of Engineering and Full Professor at the University of Western Ontario, Canada. Dr. Sun received his Ph.D. in Materials Chemistry in 1999 from the University of Manchester, U.K., which he followed up by working as a postdoctoral fellow at the University of British Columbia, Canada, and as a Research Associate at L'Institut National de la Recherche Scientifique (INRS), Canada. His current research interests are focused on advanced materials for electrochemical energy storage and conversion including solid-state batteries, interface and solid state electrolytes, and electrocatalysts.

ACKNOWLEDGMENTS

This research was supported by the Natural Sciences and Engineering Research Council of Canada (NSERC), the Canada Research Chair Program (CRC), the Canada Foundation for Innovation (CFI), the Ontario Research Fund, and the Natural Science Foundation of China (No. 51902150), the Shenzhen Science and Technology Program (No. KQTD20200820113047086), and the Guangdong Provincial Key Laboratory of Energy Materials for Electric Power (No. 2018B030322001).

REFERENCES

(1) Kumar, P. P.; Yashonath, S. Ionic Conduction in the Solid State. *Proc. - Indian Acad. Sci., Chem. Sci.* **2006**, *118*, 135−154.

(2) Shi, S.; Lu, P.; Liu, Z.; Qi, Y.; Hector, L. G.; Li, H.; Harris, S. J. Direct Calculation of Li-Ion Transport in the Solid Electrolyte Interphase. *J. Am. Chem. Soc.* **2012**, *134*, 15476−15487.

(3) He, X.; Zhu, Y.; Mo, Y. Origin of Fast Ion Diffusion in Super-Ionic Conductors. *Nat. Commun.* **2017**, *8*, 15893.

(4) Kamaya, N.; Homma, K.; Yamakawa, Y.; Hirayama, M.; Kanno, R.; Yonemura, M.; Kamiyama, T.; Kato, Y.; Hama, S.; Kawamoto, K.; et al. A Lithium Superionic Conductor. *Nat. Mater.* **2011**, *10*, 682−686.

(5) Deiseroth, H.-J.; Kong, S.-T.; Eckert, H.; Vannahme, J.; Reiner, C.; Zaiß, T.; Schlosser, M. Li_6PS_5X: A Class of Crystalline Li-Rich Solids with an Unusually High Li^+ Mobility. *Angew. Chem., Int. Ed.* **2008**, *47*, 755−758.

(6) Wang, C.; Fu, K.; Kammampata, S. P.; McOwen, D. W.; Samson, A. J.; Zhang, L.; Hitz, G. T.; Nolan, A. M.; Wachsman, E. D.; Mo, Y.; et al. Garnet-Type Solid-State Electrolytes: Materials, Interfaces, and Batteries. *Chem. Rev.* **2020**, *120*, 4257−4300.

(7) Bachman, J. C.; Muy, S.; Grimaud, A.; Chang, H.-H.; Pour, N.; Lux, S. F.; Paschos, O.; Maglia, F.; Lupart, S.; Lamp, P.; et al. Inorganic Solid-State Electrolytes for Lithium Batteries: Mechanisms and Properties Governing Ion Conduction. *Chem. Rev.* **2016**, *116*, 140−162.

(8) Zhao, W.; Yi, J.; He, P.; Zhou, H. Solid-State Electrolytes for Lithium-Ion Batteries: Fundamentals, Challenges and Perspectives. *Electrochem. Energy Rev.* **2019**, *2*, 574−605.

(9) Chen, R.; Qu, W.; Guo, X.; Li, L.; Wu, F. The pursuit of solid-state electrolytes for lithium batteries: from comprehensive insight to emerging horizons. *Mater. Horiz.* **2016**, *3*, 487−516.

(10) Wang, Y.; Zhang, H.; Zhu, J.; Lü, X.; Li, S.; Zou, R.; Zhao, Y. Antiperovskites with Exceptional Functionalities. *Adv. Mater.* **2020**, *32*, 1905007.

(11) Zhao, Y.; Daemen, L. L. Superionic Conductivity in Lithium-Rich Anti-Perovskites. *J. Am. Chem. Soc.* **2012**, *134*, 15042−15047.

(12) Wang, Y.; Richards, W. D.; Ong, S. P.; Miara, L. J.; Kim, J. C.; Mo, Y.; Ceder, G. Design Principles for Solid-State Lithium Superionic Conductors. *Nat. Mater.* **2015**, *14*, 1026−1031.

(13) Braga, M. H.; Ferreira, J. A.; Stockhausen, V.; Oliveira, J. E.; El-Azab, A. Novel Li_3ClO Based Glasses with Superionic Properties for Lithium Batteries. *J. Mater. Chem. A* **2014**, *2*, 5470−5480.

(14) Sun, Y.; Wang, Y.; Liang, X.; Xia, Y.; Peng, L.; Jia, H.; Li, H.; Bai, L.; Feng, J.; Jiang, H.; et al. Rotational Cluster Anion Enabling Superionic Conductivity in Sodium-Rich Antiperovskite Na_3OBH4. *J. Am. Chem. Soc.* **2019**, *141*, 5640−5644.

(15) Xiao, Y.; Turcheniuk, K.; Narla, A.; Song, A.-Y.; Ren, X.; Magasinski, A.; Jain, A.; Huang, S.; Lee, H.; Yushin, G. Electrolyte Melt Infiltration for Scalable Manufacturing of Inorganic All-Solid-State Lithium-Ion Batteries. *Nat. Mater.* **2021**, *20*, 984−990.

(16) Braga, M. H.; Grundish, N. S.; Murchison, A. J.; Goodenough, J. B. Alternative Strategy for a Safe Rechargeable Battery. *Energy Environ. Sci.* **2017**, *10*, 331−336.

(17) Zhang, H.; Xia, W.; Shen, H.; Guo, W.; Liang, Z.; Zhang, K.; Wu, Y.; Zhu, B.; Zou, R. Antiperovskite Intermetallic Nanoparticles for Enhanced Oxygen Reduction. *Angew. Chem., Int. Ed.* **2020**, *59*, 1871−1877.

(18) Vaughn, D. D., II; Araujo, J.; Meduri, P.; Callejas, J. F.; Hickner, M. A.; Schaak, R. E. Solution Synthesis of Cu_3PdN Nanocrystals as Ternary Metal Nitride Electrocatalysts for the Oxygen Reduction Reaction. *Chem. Mater.* **2014**, *26*, 6226−6232.

(19) He, T.; Huang, Q.; Ramirez, A. P.; Wang, Y.; Regan, K. A.; Rogado, N.; Hayward, M. A.; Haas, M. K.; Slusky, J. S.; Inumara, K.; et al. Superconductivity in the Non-Oxide Perovskite $MgCNi_3$. *Nature* **2001**, *411*, 54−56.

(20) Shannon, R. D.; Prewitt, C. T. Effective Ionic Radii in Oxides and Fluorides. *Acta Crystallogr., Sect. B: Struct. Crystallogr. Cryst. Chem.* **1969**, *25*, 925−946.

(21) Shannon, R. Revised Effective Ionic Radii and Systematic Studies of Interatomic Distances in Halides and Chalcogenides. *Acta Crystallogr., Sect. A: Cryst. Phys., Diffr., Theor. Gen. Crystallogr.* **1976**, *32*, 751−767.

(22) Goldschmidt, V. M. J. N. Die Gesetze der Krystallochemie. *Naturwissenschaften* **1926**, *14*, 477−485.

(23) Kieslich, G.; Sun, S.; Cheetham, A. K. Solid-State Principles Applied to Organic-Inorganic Perovskites: New Tricks for an Old Dog. *Chem. Sci.* **2014**, *5*, 4712−4715.

(24) Fang, H.; Jena, P. Li-Rich Antiperovskite Superionic Conductors Based on Cluster Ions. *Proc. Natl. Acad. Sci. U. S. A.* **2017**, *114*, 11046−11051.

(25) Fang, H.; Jena, P. Sodium Superionic Conductors Based on Clusters. *ACS Appl. Mater. Interfaces* **2019**, *11*, 963−972.

(26) Wang, Z.; Xu, H.; Xuan, M.; Shao, G. From Anti-Perovskite to Double Anti-Perovskite: Tuning Lattice Chemistry to Achieve Super-Fast Li^+ Transport in Cubic Solid Lithium Halogen-Chalcogenides. *J. Mater. Chem. A* **2018**, *6*, 73−83.

(27) Fang, H.; Jena, P. Atomic-Level Design of Water-Resistant Hybrid Perovskites for Solar Cells by Using Cluster Ions. *J. Phys. Chem. Lett.* **2017**, *8*, 3726−3733.

(28) Yu, Y.; Wang, Z.; Shao, G. Theoretical Formulation of Na_3AO_4X (A = S/Se, X = F/Cl) as High-Performance Solid Electrolytes for All-Solid-State Sodium Batteries. *J. Mater. Chem. A* **2019**, *7*, 21985−21996.

(29) Akkerman, Q. A.; Manna, L. What Defines a Halide Perovskite? *ACS Energy Lett.* **2020**, *5*, 604−610.

(30) Li, C.; Soh, K. C. K.; Wu, P. Formability of ABO_3 Perovskites. *J. Alloys Compd.* **2004**, *372*, 40−48.

(31) Travis, W.; Glover, E. N. K.; Bronstein, H.; Scanlon, D. O.; Palgrave, R. G. On the Application of the Tolerance Factor to Inorganic and Hybrid Halide Perovskites: A Revised System. *Chem. Sci.* **2016**, *7*, 4548−4556.

(32) Li, C.; Lu, X.; Ding, W.; Feng, L.; Gao, Y.; Guo, Z. Formability of ABX_3 (X = F, Cl, Br, I) Halide Perovskites. *Acta Crystallogr., Sect. B: Struct. Sci.* **2008**, *64*, 702−707.

(33) Bartel, C. J.; Sutton, C.; Goldsmith, B. R.; Ouyang, R.; Musgrave, C. B.; Ghiringhelli, L. M.; Scheffler, M. New Tolerance Factor to Predict the Stability of Perovskite Oxides and Halides. *Sci. Adv.* **2019**, *5*, No. eaav0693.

(34) Wang, B.; Ohgushi, K. Post-Perovskite Transition in Anti-Structure. *Sci. Rep.* **2016**, *6*, 37896.

(35) Ross, N. L. Distortion of $GdFeO_3$-Type Perovskites with Pressure: A Study of $YAlO_3$ to 5 GPa. *Phase Transitions* **1996**, *58*, 27−41.

(36) Wolf, G. H.; Bukowinski, M. S. T. Theoretical Study of the Structural Properties and Equations of State of $MgSiO_3$ and $CaSiO_3$ Perovskites: Implications for Lower Mantle Composition. *Geophys. Monogr.* **1987**, *39*, 313−331.

(37) O'Keeffe, M.; Hyde, B. G. Some Structures Topologically Related to Cubic Perovskite (E21), ReO_3 (D09) and Cu_3Au (L12). *Acta Crystallogr., Sect. B: Struct. Crystallogr. Cryst. Chem.* **1977**, *33*, 3802−3813.

(38) Zhao, Y. Crystal Chemistry and Phase Transitions of Perovskite in $P-T-X$ Space: Data for (K_xNa_{1-x}) MgF_3 Perovskites. *J. Solid State Chem.* **1998**, *141*, 121−132.

(39) Schwering, G.; Hönnerscheid, A.; van Wüllen, L.; Jansen, M. High Lithium Ionic Conductivity in the Lithium Halide Hydrates $Li_{3-n}(OH_n)Cl$ ($0.83 \le n \le 2$) and $Li_{3-n}(OH_n)Br$ ($1 \le n \le 2$) at Ambient Temperatures. *ChemPhysChem* **2003**, *4*, 343−348.

(40) King, G.; Woodward, P. M. Cation Ordering in Perovskites. *J. Mater. Chem.* **2010**, *20*, 5785−5796.

(41) Mitchell, R. H.; Welch, M. D.; Chakhmouradian, A. R. Nomenclature of the Perovskite Supergroup: A Hierarchical System of Classification Based on Crystal Structure and Composition. *Mineral. Mag.* **2017**, *81*, 411−461.

(42) Zhao, Y.; Weidner, D. J.; Parise, J. B.; Cox, D. E. Critical Phenomena and Phase Transition of Perovskite — Data for $NaMgF_3$ Perovskite. Part II. *Phys. Earth Planet. Inter.* **1993**, *76*, 17−34.

(43) Glazer, A. The Classification of Tilted Octahedra in Perovskites. *Acta Crystallogr., Sect. B: Struct. Crystallogr. Cryst. Chem.* **1972**, *28*, 3384−3392.

(44) Glazer, A. Simple Ways of Determining Perovskite Structures. *Acta Crystallogr., Sect. A: Cryst. Phys., Diffr., Theor. Gen. Crystallogr.* **1975**, *31*, 756−762.

(45) Howard, C. J.; Stokes, H. T. Group-Theoretical Analysis of Octahedral Tilting in Perovskites. *Acta Crystallogr., Sect. B: Struct. Sci.* **1998**, *54*, 782−789.

(46) Wu, Z.; Zhang, Q.; Li, B.; Shi, Z.; Xu, K.; Chen, Y.; Ning, Z.; Mi, Q. Stabilizing the $CsSnCl_3$ Perovskite Lattice by B-Site Substitution for Enhanced Light Emission. *Chem. Mater.* **2019**, *31*, 4999−5004.

(47) Ju, M.-G.; Dai, J.; Ma, L.; Zeng, X. C. Lead-Free Mixed Tin and Germanium Perovskites for Photovoltaic Application. *J. Am. Chem. Soc.* **2017**, *139*, 8038−8043.

(48) Sutton, R. J.; Eperon, G. E.; Miranda, L.; Parrott, E. S.; Kamino, B. A.; Patel, J. B.; Hörantner, M. T.; Johnston, M. B.; Haghighirad, A. A.; Moore, D. T.; et al. Bandgap-Tunable Cesium Lead Halide Perovskites with High Thermal Stability for Efficient Solar Cells. *Adv. Energy Mater.* **2016**, *6*, 1502458.

(49) Wang, Y.; Wang, Q.; Liu, Z.; Zhou, Z.; Li, S.; Zhu, J.; Zou, R.; Wang, Y.; Lin, J.; Zhao, Y. Structural Manipulation Approaches towards Enhanced Sodium Ionic Conductivity in Na-Rich Antiperovskites. *J. Power Sources* **2015**, *293*, 735−740.

(50) Ducau, M.; Suh, K. S.; Senegas, J.; Darriet, J. Crystal Structure and NMR Studies of a Cubic Perovskite: The Fluoride $NaBaLiNiF_6$. *Mater. Res. Bull.* **1992**, *27*, 1115−1123.

(51) Sabelli, C. Structure Refinement of Elpasolite from Cetine Mine, Tuscany, Italy. *Neues Jahrbuch fur Mineralogie, Monatshefte* **1987**, 481−487.

(52) Millange, F.; Caignaert, V.; Domengès, B.; Raveau, B.; Suard, E. Order−Disorder Phenomena in New $LaBaMn_2O_{6-x}$ CMR Perovskites. Crystal and Magnetic Structure. *Chem. Mater.* **1998**, *10*, 1974−1983.

(53) Lufaso, M. W.; Woodward, P. M. Jahn-Teller Distortions, Cation Ordering and Octahedral Tilting in Perovskites. *Acta Crystallogr., Sect. B: Struct. Sci.* **2004**, *60*, 10−20.

(54) Leinenweber, K.; Parise, J. High-Pressure Synthesis and Crystal Structure of $CaFeTi_2O_6$, a New Perovskite Structure Type. *J. Solid State Chem.* **1995**, *114*, 277−281.

(55) Woodward, P. M.; Vogt, T.; Cox, D. E.; Arulraj, A.; Rao, C. N. R.; Karen, P.; Cheetham, A. K. Influence of Cation Size on the Structural Features of $Ln_{1/2}A_{1/2}MnO_3$ Perovskites at Room Temperature. *Chem. Mater.* **1998**, *10*, 3652−3665.

(56) Davies, P. K.; Wu, H.; Borisevich, A. Y.; Molodetsky, I. E.; Farber, L. Crystal Chemistry of Complex Perovskites: New Cation-Ordered Dielectric Oxides. *Annu. Rev. Mater. Res.* **2008**, *38*, 369−401.

(57) Yang, M.; Oró-Solé, J.; Rodgers, J. A.; Jorge, A. B.; Fuertes, A.; Attfield, J. P. Anion Order in Perovskite Oxynitrides. *Nat. Chem.* **2011**, *3*, 47−52.

(58) Rautama, E.-L.; Boullay, P.; Kundu, A. K.; Caignaert, V.; Pralong, V.; Karppinen, M.; Raveau, B. Cationic Ordering and Microstructural Effects in the Ferromagnetic Perovskite $La_{0.5}Ba_{0.5}CoO_3$: Impact upon Magnetotransport Properties. *Chem. Mater.* **2008**, *20*, 2742−2750.

(59) Anderson, M. T.; Greenwood, K. B.; Taylor, G. A.; Poeppelmeier, K. R. B-Cation Arrangements in Double Perovskites. *Prog. Solid State Chem.* **1993**, *22*, 197−233.

(60) Turp, S. A.; Hargreaves, J.; Baek, J.; Halasyamani, P. S.; Hayward, M. A. Noncentrosymmetric Cation Order in the Cubic Perovskite $Ba_4CaFe_3O_{9.5}$. *Chem. Mater.* **2010**, *22*, 5580−5587.

(61) Yu, Y.; Wang, Z.; Shao, G. Theoretical Design of Double Anti-Perovskite Na_6SOI_2 as a Super-Fast Ion Conductor for Solid Na^+ Ion Batteries. *J. Mater. Chem. A* **2018**, *6*, 19843−19852.

(62) Kröger, F. A.; Vink, H. J. Relations between the Concentrations of Imperfections in Crystalline Solids. *Solid State Phys.* **1956**, *3*, 307−435.

(63) Maughan, A. E.; Ganose, A. M.; Scanlon, D. O.; Neilson, J. R. Perspectives and Design Principles of Vacancy-Ordered Double Perovskite Halide Semiconductors. *Chem. Mater.* **2019**, *31*, 1184−1195.

(64) He, Y.; Kontsevoi, O. Y.; Stoumpos, C. C.; Trimarchi, G. G.; Islam, S. M.; Liu, Z.; Kostina, S. S.; Das, S.; Kim, J.-I.; Lin, W.; et al. Defect Antiperovskite Compounds $Hg_3Q_2I_2$ (Q = S, Se, and Te) for Room-Temperature Hard Radiation Detection. *J. Am. Chem. Soc.* **2017**, *139*, 7939−7951.

(65) Valldor, M.; Wright, T.; Fitch, A.; Prots, Y. Metal Vacancy Ordering in an Antiperovskite Resulting in Two Modifications of Fe_2SeO. *Angew. Chem., Int. Ed.* **2016**, *55*, 9380−9383.

(66) de Quilettes, D. W.; Vorpahl, S. M.; Stranks, S. D.; Nagaoka, H.; Eperon, G. E.; Ziffer, M. E.; Snaith, H. J.; Ginger, D. S. Impact of Microstructure on Local Carrier Lifetime in Perovskite Solar Cells. *Science* **2015**, *348*, 683−686.

(67) Ball, J. M.; Petrozza, A. Defects in Perovskite-Halides and Their Effects in Solar Cells. *Nat. Energy* **2016**, *1*, 16149.

(68) Vikrant, K. S. N.; García, R. E. Charged Grain Boundary Transitions in Ionic Ceramics for Energy Applications. *npj Comput. Mater.* **2019**, *5*, 24.

(69) Kojima, A.; Teshima, K.; Shirai, Y.; Miyasaka, T. Organometal Halide Perovskites as Visible-Light Sensitizers for Photovoltaic Cells. *J. Am. Chem. Soc.* **2009**, *131*, 6050−6051.

(70) Koh, T. M.; Fu, K.; Fang, Y.; Chen, S.; Sum, T. C.; Mathews, N.; Mhaisalkar, S. G.; Boix, P. P.; Baikie, T. Formamidinium-Containing

Metal-Halide: An Alternative Material for Near-IR Absorption Perovskite Solar Cells. *J. Phys. Chem. C* **2014**, *118*, 16458−16462.

(71) Arpino, K. E.; Wallace, D. C.; Nie, Y. F.; Birol, T.; King, P. D. C.; Chatterjee, S.; Uchida, M.; Koohpayeh, S. M.; Wen, J. J.; Page, K.; et al. Evidence for Topologically Protected Surface States and a Superconducting Phase in $[Tl_4](Tl_{1-x}Sn_x)Te_3$ Using Photoemission, Specific Heat, and Magnetization Measurements, and Density Functional Theory. *Phys. Rev. Lett.* **2014**, *112*, No. 017002.

(72) Klösters, G.; van Wüllen, L.; Jansen, M. The Nature of the Nitrite Disorder in Na_3ONO_2. *Phys. Chem. Chem. Phys.* **2002**, *4*, 3461−3466.

(73) Skakle, J. M. S.; Fletcher, J. G.; West, A. R. Polymorphism, Structures and Phase Transformation of $K_3[SO_4]F$. *J. Chem. Soc., Dalton Trans.* **1996**, *12*, 2497−2501.

(74) Kanishcheva, A. S.; Zaitseva, I. Y.; Kovalyova, I. S.; Mikhailov, Y. N. Synthesis and Crystal Structure of Cs_3ZnBr_5. *Russ. J. Inorg. Chem.* **2010**, *55*, 1882−1887.

(75) Zhang, X.; Liu, K.; He, J.-Q.; Wu, H.; Huang, Q.-Z.; Lin, J.-H.; Lu, Z.-Y.; Huang, F.-Q. Antiperovskite Chalco-Halides $Ba_3(FeS_4)Cl$, $Ba_3(FeS_4)Br$ and $Ba_3(FeSe_4)Br$ with Spin Super-Super Exchange. *Sci. Rep.* **2015**, *5*, 15910.

(76) Gebhardt, J.; Rappe, A. M. Mix and Match: Organic and Inorganic Ions in the Perovskite Lattice. *Adv. Mater.* **2019**, *31*, 1802697.

(77) Fang, H.; Jena, P. Super-Ion Inspired Colorful Hybrid Perovskite Solar Cells. *J. Mater. Chem. A* **2016**, *4*, 4728−4737.

(78) Leguy, A. M. A.; Frost, J. M.; McMahon, A. P.; Sakai, V. G.; Kockelmann, W.; Law, C.; Li, X.; Foglia, F.; Walsh, A.; O'Regan, B. C.; et al. The Dynamics of Methylammonium Ions in Hybrid Organic-Inorganic Perovskite solar cells. *Nat. Commun.* **2015**, *6*, 7124.

(79) Wasylishen, R. E.; Knop, O.; Macdonald, J. B. Cation Rotation in Methylammonium Lead Halides. *Solid State Commun.* **1985**, *56*, 581−582.

(80) Poglitsch, A.; Weber, D. Dynamic Disorder in Methylammoniumtrihalogenoplumbates (II) Observed by Millimeter-Wave Spectroscopy. *J. Chem. Phys.* **1987**, *87*, 6373−6378.

(81) Mattoni, A.; Filippetti, A.; Saba, M.; Delugas, P. Methylammonium Rotational Dynamics in Lead Halide Perovskite by Classical Molecular Dynamics: The Role of Temperature. *J. Phys. Chem. C* **2015**, *119*, 17421−17428.

(82) Weller, M. T.; Weber, O. J.; Henry, P. F.; Di Pumpo, A. M.; Hansen, T. C. Complete Structure and Cation Orientation in the Perovskite Photovoltaic Methylammonium Lead Iodide between 100 and 352 K. *Chem. Commun.* **2015**, *51*, 4180−4183.

(83) Balachandran, P. V.; Puggioni, D.; Rondinelli, J. M. Crystal-Chemistry Guidelines for Noncentrosymmetric A_2BO_4 Ruddlesden-Popper Oxides. *Inorg. Chem.* **2014**, *53*, 336−348.

(84) Iliev, M. N.; Popov, V. N.; Litvinchuk, A. P.; Abrashev, M. V.; Bäckström, J.; Sun, Y. Y.; Meng, R. L.; Chu, C. W. Comparative Raman Studies of Sr_2RuO_4, $Sr_3Ru_2O_7$ and $Sr_4Ru_3O_{10}$. *Phys. B* **2005**, *358*, 138−152.

(85) Xu, Z.; Chen, M.; Liu, S. F. Layer-Dependent Ultrahigh-Mobility Transport Properties in All-Inorganic Two-Dimensional $Cs_2PbI_2Cl_2$ and $Cs_2SnI_2Cl_2$ Perovskites. *J. Phys. Chem. C* **2019**, *123*, 27978−27985.

(86) Zhu, J.; Li, S.; Zhang, Y.; Howard, J. W.; Lü, X.; Li, Y.; Wang, Y.; Kumar, R. S.; Wang, L.; Zhao, Y. Enhanced Ionic Conductivity with $Li_7O_2Br_3$ Phase in Li_3OBr Anti-Perovskite Solid Electrolyte. *Appl. Phys. Lett.* **2016**, *109*, 101904.

(87) Zhu, J.; Wang, Y.; Li, S.; Howard, J. W.; Neuefeind, J.; Ren, Y.; Wang, H.; Liang, C.; Yang, W.; Zou, R.; et al. Sodium Ion Transport Mechanisms in Antiperovskite Electrolytes Na_3OBr and Na_4OI_2: An in Situ Neutron Diffraction Study. *Inorg. Chem.* **2016**, *55*, 5993−5998.

(88) Mao, L.; Ke, W.; Pedesseau, L.; Wu, Y.; Katan, C.; Even, J.; Wasielewski, M. R.; Stoumpos, C. C.; Kanatzidis, M. G. Hybrid Dion-Jacobson 2D Lead Iodide Perovskites. *J. Am. Chem. Soc.* **2018**, *140*, 3775−3783.

(89) Gebhardt, J.; Rappe, A. M. Adding to the Perovskite Universe: Inverse-Hybrid Perovskites. *ACS Energy Lett.* **2017**, *2*, 2681−2685.

(90) Krivovichev, S. V. Minerals with Antiperovskite Structure: A Review. *Z. Kristallogr. - Cryst. Mater.* **2008**, *223*, 109−113.

(91) Wiedemann, D.; Meutzner, F.; Fabelo, O.; Ganschow, S. The Inverse Perovskite $BaLiF_3$: Single-Crystal Neutron Diffraction and Analyses of Potential Ion Pathways. *Acta Crystallogr., Sect. B: Struct. Sci., Cryst. Eng. Mater.* **2018**, *74*, 643−650.

(92) Glasser, L. Lattice Energies of Crystals with Multiple Ions: A Generalized Kapustinskii Equation. *Inorg. Chem.* **1995**, *34*, 4935−4936.

(93) Mouta, R.; Melo, M. Á. B.; Diniz, E. M.; Paschoal, C. W. A. Concentration of Charge Carriers, Migration, and Stability in Li_3OCl Solid Electrolytes. *Chem. Mater.* **2014**, *26*, 7137−7144.

(94) Kovalenko, M. V.; Protesescu, L.; Bodnarchuk, M. I. Properties and Potential Optoelectronic Applications of Lead Halide Perovskite Nanocrystals. *Science* **2017**, *358*, 745−750.

(95) Reuter, B.; Hardel, K. Silbersulfidbromid Ag_3SBr und Silbersulfidjodid Ag_3Sj. I. Darstellung, Eigenschaften und Phasenverhältnisse von Ag_3SBr und Ag_3SJ. *Z. Anorg. Allg. Chem.* **1965**, *340*, 158−167.

(96) Reuter, B.; Hardel, K. Silbersulfidbromid Ag_3SBr und Silbersulfidjodid Ag_3SJ. II. Die Kristallstrukturen von Ag_3SBr, β -und α-Ag_3SJ. *Z. Anorg. Allg. Chem.* **1965**, *340*, 168−180.

(97) Reuter, B.; Hardel, K. Silbersulfidbromid Ag_3SBr und Silbersulfidjodid Ag_3SJ. III. Die Halbleitereigenschaften von Ag_3SBr, β- und α-Ag_3SJ. *Ber. Bunsenges. Phys. Chem.* **1966**, *70*, 82−86.

(98) Müller, W.; Jansen, M. $(CN)ONa_3$, Kristallstruktur und Natriumionenleitfähigkeit. *Z. Anorg. Allg. Chem.* **1990**, *591*, 41−46.

(99) Chihara, H.; Kawakami, T.; Soda, G. The NMR Study of the Disorder in Lithium Iodide Monohydrate and Monodeuterate. *J. Magn. Reson.* **1969**, *1*, 75−88.

(100) Armstrong, R.; Landles, K. Electrochemical Behaviour of Lithium Iodide Monohydrate. *J. Appl. Electrochem.* **1981**, *11*, 247−251.

(101) Poulsen, F. W. Ionic Conductivity of Solid Lithium Iodide and Its Monohydrate. *Solid State Ionics* **1981**, *2*, 53−57.

(102) Archer, W. I.; Armstrong, R. D. Electrochemical Properties of $LiBr.H_2O$. *Electrochim. Acta* **1981**, *26*, 1083−1085.

(103) Nakamura, O.; Goodenough, J. B. Conductivity Enhancement of Lithium Bromide Monohydrate by Al_2O_3 Particles. *Solid State Ionics* **1982**, *7*, 119−123.

(104) Li, Y.; Zhou, W.; Xin, S.; Li, S.; Zhu, J.; Lü, X.; Cui, Z.; Jia, Q.; Zhou, J.; Zhao, Y.; et al. Fluorine-Doped Antiperovskite Electrolyte for All-Solid-State Lithium-Ion Batteries. *Angew. Chem., Int. Ed.* **2016**, *55*, 9965−9968.

(105) Song, A.-Y.; Xiao, Y.; Turcheniuk, K.; Upadhya, P.; Ramanujapuram, A.; Benson, J.; Magasinski, A.; Olguin, M.; Meda, L.; Borodin, O.; et al. Protons Enhance Conductivities in Lithium Halide Hydroxide/Lithium Oxyhalide Solid Electrolytes by Forming Rotating Hydroxy Groups. *Adv. Energy Mater.* **2018**, *8*, 1700971.

(106) Braga, M. H.; Murchison, A. J.; Ferreira, J. A.; Singh, P.; Goodenough, J. B. Glass-Amorphous Alkali-Ion Solid Electrolytes and Their Performance in Symmetrical Cells. *Energy Environ. Sci.* **2016**, *9*, 948−954.

(107) Han, F.; Westover, A. S.; Yue, J.; Fan, X.; Wang, F.; Chi, M.; Leonard, D. N.; Dudney, N. J.; Wang, H.; Wang, C. High Electronic Conductivity as the Origin of Lithium Dendrite Formation within Solid Electrolytes. *Nat. Energy* **2019**, *4*, 187−196.

(108) Braga, M. H.; M Subramaniyam, C.; Murchison, A. J.; Goodenough, J. B. Nontraditional, Safe, High Voltage Rechargeable Cells of Long Cycle Life. *J. Am. Chem. Soc.* **2018**, *140*, 6343−6352.

(109) Wortmann, R.; Sitta, S.; Sabrowsky, H. $Li_7O_2Br_3$ Eine weitere Strukturvariante der neuen Alkalimetallchalkogenidhalogenid-Perowskite/$Li_7O_2Br_3$ A Further Structure Variant of the New Alkali Metal Chalcogenide Halide Perovskites. *Z. Naturforsch., B: J. Chem. Sci.* **1989**, *44*, 1348−1350.

(110) Lu, Z.; Liu, J.; Ciucci, F. Superionic Conduction in Low-Dimensional-Networked Anti-Perovskites. *Energy Storage Mater.* **2020**, *28*, 146−152.

(111) Gutsev, G. L.; Boldyrev, A. I. DVM-Xα Calculations on the Ionization Potentials of MX_{k+1}^- complex anions and the electron affinities of MX_{k+1} "superhalogens. *Chem. Phys.* **1981**, *56*, 277−283.

(112) Jena, P.; Sun, Q. Super Atomic Clusters: Design Rules and Potential for Building Blocks of Materials. *Chem. Rev.* **2018**, *118*, 5755−5870.

(113) Fang, H.; Jena, P. Molecular Origin of Properties of Organic−Inorganic Hybrid Perovskites: The Big Picture from Small Clusters. *J. Phys. Chem. Lett.* **2016**, *7*, 1596−1603.

(114) Jansen, M.; Feldmann, C.; Müller, W. Über die quasi-binären Systeme $NaNO_2/Na_2O$ und $NaCN/Na_2O$. Phasendiagramme und Natrium-Ionenleitung in $Na_3O(NO_2)$ und $Na_3O(CN)$. *Z. Anorg. Allg. Chem.* **1992**, *611*, 7−10.

(115) Xu, H.; Xuan, M.; Xiao, W.; Shen, Y.; Li, Z.; Wang, Z.; Hu, J.; Shao, G. Lithium Ion Conductivity in Double Antiperovskite $Li_{6.5}OS_{1.5}I_{1.5}$: Alloying and Boundary Effects. *ACS Appl. Energy Mater.* **2019**, *2*, 6288−6294.

(116) Hartwig, P.; Rabenau, A.; Weppner, W. Lithium Hydroxide Halides: Phase Equilibria and Ionic Conductivities. *J. Less-Common Met.* **1981**, *78*, 227−233.

(117) Hood, Z. D.; Wang, H.; Samuthira Pandian, A.; Keum, J. K.; Liang, C. Li_2OHCl Crystalline Electrolyte for Stable Metallic Lithium Anodes. *J. Am. Chem. Soc.* **2016**, *138*, 1768−1771.

(118) Zhang, Y.; Zhao, Y.; Chen, C. Ab Initio Study of the Stabilities of and Mechanism of Superionic Transport in Lithium-Rich Antiperovskites. *Phys. Rev. B: Condens. Matter Mater. Phys.* **2013**, *87*, 134303.

(119) Chen, M.-H.; Emly, A.; Van der Ven, A. Anharmonicity and Phase Stability of Antiperovskite Li_3OCl. *Phys. Rev. B: Condens. Matter Mater. Phys.* **2015**, *91*, 214306.

(120) Ortman, M. S.; Larsen, E. M. Preparation, Characterization, and Melting Point of High-Purity Lithium Oxide. *J. Am. Ceram. Soc.* **1983**, *66*, 645−648.

(121) Haynes, W. M.*CRC Handbook of Chemistry and Physics*, 97th ed.; CRC Press, 2016; pp 4−70.

(122) Achchaq, F.; Palomo del Barrio, E.; Lebraud, E.; Péchev, S.; Toutain, J. Development of a New LiBr/LiOH-Based Alloy for Thermal Energy Storage. *J. Phys. Chem. Solids* **2019**, *131*, 173−179.

(123) Friese, K.; Hönnerscheid, A.; Jansen, M. Crystal Structure Determination of Systematically Intergrown Compounds: $Li_5(OH)_2Br_3$ and $Li_2(OH)Br$. *Z. Kristallogr. - Cryst. Mater.* **2003**, *218*, 536−541.

(124) Li, S.; Zhu, J.; Wang, Y.; Howard, J. W.; Lü, X.; Li, Y.; Kumar, R. S.; Wang, L.; Daemen, L. L.; Zhao, Y. Reaction Mechanism Studies towards Effective Fabrication of Lithium-Rich Anti-Perovskites Li_3OX (X = Cl, Br). *Solid State Ionics* **2016**, *284*, 14−19.

(125) Zhang, Q.; Saito, F. A Review on Mechanochemical Syntheses of Functional Materials. *Adv. Powder Technol.* **2012**, *23*, 523−531.

(126) Howard, J. L.; Cao, Q.; Browne, D. L. Mechanochemistry as an Emerging Tool for Molecular Synthesis: What Can It Offer? *Chem. Sci.* **2018**, *9*, 3080−3094.

(127) Urakaev, F.Mechanism and Kinetics of Mechanochemical Processes. In *High-Energy Ball Milling*; Woodhead Publishing, 2010; pp 9−44.

(128) Gautam, A.; Sadowski, M.; Prinz, N.; Eickhoff, H.; Minafra, N.; Ghidiu, M.; Culver, S. P.; Albe, K.; Fässler, T. F.; Zobel, M.; et al. Rapid Crystallization and Kinetic Freezing of Site-Disorder in the Lithium Superionic Argyrodite Li_6PS_5Br. *Chem. Mater.* **2019**, *31*, 10178−10185.

(129) Schlem, R.; Muy, S.; Prinz, N.; Banik, A.; Shao-Horn, Y.; Zobel, M.; Zeier, W. G. Mechanochemical Synthesis: A Tool to Tune Cation Site Disorder and Ionic Transport Properties of Li_3MCl_6 (M = Y, Er) Superionic Conductors. *Adv. Energy Mater.* **2020**, *10*, 1903719.

(130) Sugumar, M. K.; Yamamoto, T.; Motoyama, M.; Iriyama, Y. Room Temperature Synthesis of Anti-Perovskite Structured Li_2OHBr. *Solid State Ionics* **2020**, *349*, 115298.

(131) Yamamoto, T.; Shiba, H.; Mitsukuchi, N.; Sugumar, M. K.; Motoyama, M.; Iriyama, Y. Synthesis of the Metastable Cubic Phase of Li_2OHCl by a Mechanochemical Method. *Inorg. Chem.* **2020**, *59*, 11901−11904.

(132) Makiura, R.; Yonemura, T.; Yamada, T.; Yamauchi, M.; Ikeda, R.; Kitagawa, H.; Kato, K.; Takata, M. Size-Controlled Stabilization of the Superionic Phase to Room Temperature in Polymer-Coated AgI Nanoparticles. *Nat. Mater.* **2009**, *8*, 476−480.

(133) Ohkoshi, S.-i.; Tsunobuchi, Y.; Matsuda, T.; Hashimoto, K.; Namai, A.; Hakoe, F.; Tokoro, H. Synthesis of a Metal Oxide with a Room-Temperature Photoreversible Phase Transition. *Nat. Chem.* **2010**, *2*, 539−545.

(134) Bates, J. B.; Dudney, N. J.; Neudecker, B.; Ueda, A.; Evans, C. D. Thin-Film Lithium and Lithium-Ion Batteries. *Solid State Ionics* **2000**, *135*, 33−45.

(135) Oudenhoven, J. F. M.; Baggetto, L.; Notten, P. H. L. All-Solid-State Lithium-Ion Microbatteries: A Review of Various Three-Dimensional Concepts. *Adv. Energy Mater.* **2011**, *1*, 10−33.

(136) Singh, R. K.; Narayan, J. Pulsed-Laser Evaporation Technique for Deposition of Thin Films: Physics and Theoretical Model. *Phys. Rev. B: Condens. Matter Mater. Phys.* **1990**, *41*, 8843−8859.

(137) Lü, X.; Wu, G.; Howard, J. W.; Chen, A.; Zhao, Y.; Daemen, L. L.; Jia, Q. Li-rich Anti-Perovskite Li_3OCl Films with Enhanced Ionic Conductivity. *Chem. Commun.* **2014**, *50*, 11520−11522.

(138) Lü, X.; Howard, J. W.; Chen, A.; Zhu, J.; Li, S.; Wu, G.; Dowden, P.; Xu, H.; Zhao, Y.; Jia, Q. Antiperovskite Li_3OCl Superionic Conductor Films for Solid-State Li-Ion Batteries. *Adv. Sci.* **2016**, *3*, 1500359.

(139) Badding, J. V. High-Pressure Synthesis, Characterization, and Tuning of Solid State Materials. *Annu. Rev. Mater. Sci.* **1998**, *28*, 631−658.

(140) Liu, X.-Y.High Pressure Synthesis and Preparation of Inorganic Materials. In *Modern Inorganic Synthetic Chemistry*, 2nd ed.; Xu, R., Xu, Y., Eds.; Elsevier: Amsterdam, 2017; pp 105−141.

(141) Brazhkin, V. V. High-Pressure Synthesized Materials: Treasures and Hints. *High Pressure Res.* **2007**, *27*, 333−351.

(142) Zhang, J.; Han, J.; Zhu, J.; Lin, Z.; Braga, M. H.; Daemen, L. L.; Wang, L.; Zhao, Y. High Pressure-High Temperature Synthesis of Lithium-Rich $Li_3O(Cl, Br)$ and $Li_{3-x}Ca_{x/2}OCl$ Anti-Perovskite Halides. *Inorg. Chem. Commun.* **2014**, *48*, 140−143.

(143) Gao, S.; Broux, T.; Fujii, S.; Tassel, C.; Yamamoto, K.; Xiao, Y.; Oikawa, I.; Takamura, H.; Ubukata, H.; Watanabe, Y.; et al. Hydride-Based Antiperovskites with Soft Anionic Sublattices as Fast Alkali Ionic Conductors. *Nat. Commun.* **2021**, *12*, 201.

(144) Zhang, J.; Zhu, J.; Wang, L.; Zhao, Y. A New Lithium-Rich Anti-Spinel in Li−O−Br System. *Chem. Commun.* **2015**, *51*, 9666−9669.

(145) Hussain, F.; Li, P.; Li, Z.; Yang, J. Ion Conductivity Enhancement in Anti-Spinel Li_3OBr with Intrinsic Vacancies. *Adv. Theory Simul.* **2019**, *2*, 1800138.

(146) Miura, A.; Rosero-Navarro, N. C.; Sakuda, A.; Tadanaga, K.; Phuc, N. H. H.; Matsuda, A.; Machida, N.; Hayashi, A.; Tatsumisago, M. Liquid-Phase Syntheses of Sulfide Electrolytes for All-Solid-State Lithium Battery. *Nat. Rev. Chem.* **2019**, *3*, 189−198.

(147) Xu, J.; Liu, L.; Yao, N.; Wu, F.; Li, H.; Chen, L. Liquid-Involved Synthesis and Processing of Sulfide-Based Solid Electrolytes, Electrodes, and All-Solid-State Batteries. *Mater. Today Nano* **2019**, *8*, 100048.

(148) Ghidiu, M.; Ruhl, J.; Culver, S. P.; Zeier, W. G. Solution-Based Synthesis of Lithium Thiophosphate Superionic Conductors for Solid-State Batteries: A Chemistry Perspective. *J. Mater. Chem. A* **2019**, *7*, 17735−17753.

(149) Liu, Z.; Fu, W.; Payzant, E. A.; Yu, X.; Wu, Z.; Dudney, N. J.; Kiggans, J.; Hong, K.; Rondinone, A. J.; Liang, C. Anomalous High Ionic Conductivity of Nanoporous β-Li_3PS_4. *J. Am. Chem. Soc.* **2013**, *135*, 975−978.

(150) Ito, S.; Nakakita, M.; Aihara, Y.; Uehara, T.; Machida, N. A Synthesis of Crystalline $Li_7P_3S_{11}$ Solid Electrolyte from 1,2-Dimethoxyethane Solvent. *J. Power Sources* **2014**, *271*, 342−345.

(151) Yao, X.; Liu, D.; Wang, C.; Long, P.; Peng, G.; Hu, Y.-S.; Li, H.; Chen, L.; Xu, X. High-Energy All-Solid-State Lithium Batteries with Ultralong Cycle Life. *Nano Lett.* **2016**, *16*, 7148−7154.

(152) Calpa, M.; Rosero-Navarro, N. C.; Miura, A.; Tadanaga, K. Instantaneous Preparation of High Lithium-Ion Conducting Sulfide Solid Electrolyte $Li_7P_3S_{11}$ by a Liquid Phase Process. *RSC Adv.* **2017**, *7*, 46499−46504.

(153) Agmon, N. The Grotthuss Mechanism. *Chem. Phys. Lett.* **1995**, *244*, 456−462.

(154) Kreuer, K.-D. Proton Conductivity: Materials and Applications. *Chem. Mater.* **1996**, *8*, 610−641.

(155) Freund, F.; Wengeler, H. Proton Conductivity of Simple Ionic Hydroxides Part I: The Proton Conductivities of $Al(OH)_3$, $Ca(OH)_2$, and $Mg(OH)_2$. *Ber. Bunsenges. Phys. Chem.* **1980**, *84*, 866−873.

(156) Xia, W.; Mahmood, A.; Zou, R.; Xu, Q. Metal-Organic Frameworks and Their Derived Nanostructures for Electrochemical Energy Storage and Conversion. *Energy Environ. Sci.* **2015**, *8*, 1837−1866.

(157) Eilbracht, C.; Kockelmann, W.; Hohlwein, D.; Jacobs, H. Orientational Disorder in Perovskite Like Structures of $Li_2X(OD)$ (X = Cl, Br) and $LiBr{\cdot}D_2O$. *Phys. B* **1997**, *234−236*, 48−50.

(158) Dawson, J. A.; Attari, T. S.; Chen, H.; Emge, S. P.; Johnston, K. E.; Islam, M. S. Elucidating Lithium-Ion and Proton Dynamics in Anti-Perovskite Solid Electrolytes. *Energy Environ. Sci.* **2018**, *11*, 2993−3002.

(159) Song, A.-Y.; Turcheniuk, K.; Leisen, J.; Xiao, Y.; Meda, L.; Borodin, O.; Yushin, G. Understanding Li-Ion Dynamics in Lithium Hydroxychloride (Li_2OHCl) Solid State Electrolyte via Addressing the Role of Protons. *Adv. Energy Mater.* **2020**, *10*, 1903480.

(160) Howard, J.; Hood, Z. D.; Holzwarth, N. A. W. Fundamental Aspects of the Structural and Electrolyte Properties of Li_2OHCl from Simulations and Experiment. *Phys. Rev. Mater.* **2017**, *1*, No. 075406.

(161) Nakamura, O.; Goodenough, J. B. Fast Lithium-Ion Transport in Composites Containing Lithium-Bromide Dihydrate. *Solid State Ionics* **1982**, *7*, 125−128.

(162) Heenen, H. H.; Voss, J.; Scheurer, C.; Reuter, K.; Luntz, A. C. Multi-ion Conduction in Li_3OCl Glass Electrolytes. *J. Phys. Chem. Lett.* **2019**, *10*, 2264−2269.

(163) Emly, A.; Kioupakis, E.; Van der Ven, A. Phase Stability and Transport Mechanisms in Antiperovskite Li_3OCl and Li_3OBr Superionic Conductors. *Chem. Mater.* **2013**, *25*, 4663−4670.

(164) Lu, Z.; Chen, C.; Baiyee, Z. M.; Chen, X.; Niu, C.; Ciucci, F. Defect Chemistry and Lithium Transport in Li_3OCl Anti-Perovskite Superionic Conductors. *Phys. Chem. Chem. Phys.* **2015**, *17*, 32547−32555.

(165) Mouta, R.; Diniz, E. M.; Paschoal, C. W. A. Li^+ Interstitials as the Charge Carriers in Superionic Lithium-Rich Anti-Perovskites. *J. Mater. Chem. A* **2016**, *4*, 1586−1590.

(166) Kato, Y.; Hori, S.; Saito, T.; Suzuki, K.; Hirayama, M.; Mitsui, A.; Yonemura, M.; Iba, H.; Kanno, R. High-Power All-Solid-State Batteries Using Sulfide Superionic Conductors. *Nat. Energy* **2016**, *1*, 16030.

(167) Stegmaier, S.; Voss, J.; Reuter, K.; Luntz, A. C. Li^+ Defects in a Solid-State Li Ion Battery: Theoretical Insights with a Li_3OCl Electrolyte. *Chem. Mater.* **2017**, *29*, 4330−4340.

(168) Li, P.; Hussain, F.; Cui, P.; Li, Z.; Yang, J. Boosting Ionic Conductivity in Antiperovskite Li_3OCl via Defect Engineering: Interstitial versus Vacancy. *Phys. Rev. Mater.* **2019**, *3*, 115402.

(169) Benrath, A.; Drekopf, K. Über die elektrische Leitfähigkeit von Salzen und Salzgemischen. *Z. Phys. Chem.* **1921**, *99*, 57−70.

(170) Kvist, A.; Bengtzelius, A.Tracer Diffusion and Electrical Conductivity of Cubic Lithium Sulphate and a Transport Model for Cubic Sulphates. In *Fast Ion Transport in Solids*; van Gool, W., Ed.; North-Holland Publishing Company, 1973; pp 193−199.

(171) Lundén, A. Enhancement of Cation Mobility in Some Sulphate Phases due to a Paddle-Wheel Mechanism. *Solid State Ionics* **1988**, *28−30*, 163−167.

(172) Witschas, M.; Eckert, H.; Wilmer, D.; Banhatti, R. D.; Funke, H.; Fitter, J.; Lechner, R. E.; Korus, G.; Jansen, M. Anion Rotation and Cation Transport in the Rotor Phase α-Sodium Orthophosphate: Paddle-Wheel Mechanism Redefined in View of New Experimental Results. *Z. Phys. Chem.* **2000**, *214*, 643−673.

(173) Lu, Z.; Ciucci, F. Metal Borohydrides as Electrolytes for Solid-State Li, Na, Mg, and Ca Batteries: A First-Principles Study. *Chem. Mater.* **2017**, *29*, 9308−9319.

(174) Smith, J. G.; Siegel, D. J. Low-Temperature Paddlewheel Effect in Glassy Solid Electrolytes. *Nat. Commun.* **2020**, *11*, 1483.

(175) Jansen, M. Volume Effect or Paddle-Wheel Mechanism—Fast Alkali-Metal Ionic Conduction in Solids with Rotationally Disordered Complex Anions. *Angew. Chem., Int. Ed. Engl.* **1991**, *30*, 1547−1558.

(176) Fang, H.; Wang, S.; Liu, J.; Sun, Q.; Jena, P. Superhalogen-Based Lithium Superionic Conductors. *J. Mater. Chem. A* **2017**, *5*, 13373−13381.

(177) Gao, L.; Zhang, H.; Wang, Y.; Li, S.; Zhao, R.; Wang, Y.; Gao, S.; He, L.; Song, H.-F.; Zou, R.; et al. Mechanism of Enhanced Ionic Conductivity by Rotational Nitrite Group in Antiperovskite Na_3ONO_2. *J. Mater. Chem. A* **2020**, *8*, 21265−21272.

(178) Fan, S.; Lei, M.; Wu, H.; Hu, J.; Yin, C.; Liang, T.; Li, C. A Na-Rich Fluorinated Sulfate Anti-Perovskite with Dual Doping as Solid Electrolyte for Na Metal Solid State Batteries. *Energy Storage Mater.* **2020**, *31*, 87−94.

(179) Ban, C. W.; Choi, G. M. The Effect of Sintering on the Grain Boundary Conductivity of Lithium Lanthanum Titanates. *Solid State Ionics* **2001**, *140*, 285−292.

(180) Kataoka, K.; Nagata, H.; Akimoto, J. Lithium-Ion Conducting Oxide Single Crystal as Solid Electrolyte for Advanced Lithium Battery Application. *Sci. Rep.* **2018**, *8*, 9965.

(181) Stanje, B.; Rettenwander, D.; Breuer, S.; Uitz, M.; Berendts, S.; Lerch, M.; Uecker, R.; Redhammer, G.; Hanzu, I.; Wilkening, M. Solid Electrolytes: Extremely Fast Charge Carriers in Garnet-Type $Li_6La_3ZrTaO_{12}$ Single Crystals. *Ann. Phys.* **2017**, *529*, 1700140.

(182) Dawson, J. A.; Canepa, P.; Clarke, M. J.; Famprikis, T.; Ghosh, D.; Islam, M. S. Toward Understanding the Different Influences of Grain Boundaries on Ion Transport in Sulfide and Oxide Solid Electrolytes. *Chem. Mater.* **2019**, *31*, 5296−5304.

(183) Dawson, J. A.; Canepa, P.; Famprikis, T.; Masquelier, C.; Islam, M. S. Atomic-Scale Influence of Grain Boundaries on Li-ion Conduction in Solid Electrolytes for All-Solid-State Batteries. *J. Am. Chem. Soc.* **2018**, *140*, 362−368.

(184) Atkinson, A.; Monty, C.Grain Boundary Diffusion in Ceramics. In *Surfaces and Interfaces of Ceramic Materials*; Dufour, L.-C., Monty, C., Petot-Ervas, G.; Springer Netherlands: Dordrecht, 1989; pp 273−284.

(185) Nguyen, H.; Hy, S.; Wu, E.; Deng, Z.; Samiee, M.; Yersak, T.; Luo, J.; Ong, S. P.; Meng, Y. S. Experimental and Computational Evaluation of a Sodium-Rich Anti-Perovskite for Solid State Electrolytes. *J. Electrochem. Soc.* **2016**, *163*, A2165−A2171.

(186) Chen, B.; Xu, C.; Zhou, J. Insights into Grain Boundary in Lithium-Rich Anti-Perovskite as Solid Electrolytes. *J. Electrochem. Soc.* **2018**, *165*, A3946−A3951.

(187) Shen, K.; Wang, Y.; Zhang, J.; Zong, Y.; Li, G.; Zhao, C.; Chen, H. Revealing the Effect of Grain Boundary Segregation on Li Ion Transport in Polycrystalline Anti-Perovskite Li_3ClO: A Phase Field Study. *Phys. Chem. Chem. Phys.* **2020**, *22*, 3030−3036.

(188) Koerver, R.; Zhang, W.; de Biasi, L.; Schweidler, S.; Kondrakov, A. O.; Kolling, S.; Brezesinski, T.; Hartmann, P.; Zeier, W. G.; Janek, J. Chemo-Mechanical Expansion of Lithium Electrode Materials – on the Route to Mechanically Optimized All-Solid-State Batteries. *Energy Environ. Sci.* **2018**, *11*, 2142−2158.

(189) Cazorla, C.; Errandonea, D. Superionicity and Polymorphism in Calcium Fluoride at High Pressure. *Phys. Rev. Lett.* **2014**, *113*, 235902.

(190) Cazorla, C.; Errandonea, D. Giant Mechanocaloric Effects in Fluorite-Structured Superionic Materials. *Nano Lett.* **2016**, *16*, 3124−3129.

(191) Garcia-Barriocanal, J.; Rivera-Calzada, A.; Varela, M.; Sefrioui, Z.; Iborra, E.; Leon, C.; Pennycook, S. J.; Santamaria, J. Colossal Ionic Conductivity at Interfaces of Epitaxial ZrO_2: $Y_2O_3/SrTiO_3$ Heterostructures. *Science* **2008**, *321*, 676−680.

(192) Sagotra, A. K.; Cazorla, C. Stress-Mediated Enhancement of Ionic Conductivity in Fast-Ion Conductors. *ACS Appl. Mater. Interfaces* **2017**, *9*, 38773−38783.

(193) Wang, X.; Xiao, R.; Li, H.; Chen, L. DFT Investigations on Antiperovskite Li_3OX (X = F,Cl,Br) Superionic Conductors. *Energy Storage Sci. Technol.* **2016**, *5*, 725−729.

(194) Kim, K.; Siegel, D. J. Correlating Lattice Distortions, Ion Migration Barriers, and Stability in Solid Electrolytes. *J. Mater. Chem. A* **2019**, *7*, 3216−3227.

(195) Wu, M.; Xu, B.; Lei, X.; Huang, K.; Ouyang, C. Bulk Properties and Transport Mechanisms of a Solid State Antiperovskite Li-ion Conductor Li_3OCl: Insights from First Principles Calculations. *J. Mater. Chem. A* **2018**, *6*, 1150−1160.

(196) Schmidt, J.; Shi, J.; Borlido, P.; Chen, L.; Botti, S.; Marques, M. A. Predicting the Thermodynamic Stability of Solids Combining Density Functional Theory and Machine Learning. *Chem. Mater.* **2017**, *29*, 5090−5103.

(197) Liu, B.; Hu, Q.; Gao, T.; Liao, P.; Wen, Y.; Lu, Z.; Yang, J.; Shi, S.; Zhang, W.Computational Insights into the Ionic Transport Mechanism and Interfacial Stability of the Li_2OHCl Solid-State Electrolyte. *J. Materiomics***2021**, DOI: DOI: 10.1016/j.jmat.2021.05.006.

(198) Mo, Y.; Ong, S. P.; Ceder, G. First Principles Study of the $Li_{10}GeP_2S_{12}$ Lithium Super Ionic Conductor Material. *Chem. Mater.* **2012**, *24*, 15−17.

(199) Togo, A.; Chaput, L.; Tanaka, I.; Hug, G. First-Principles Phonon Calculations of Thermal Expansion in Ti_3SiC_2, Ti_3AlC_2, and Ti_3GeC_2. *Phys. Rev. B: Condens. Matter Mater. Phys.* **2010**, *81*, 174301.

(200) Thangadurai, V.; Weppner, W. $Li_6ALa_2Ta_2O_{12}$ (A= Sr, Ba): Novel Garnet-Like Oxides for Fast Lithium Ion Conduction. *Adv. Funct. Mater.* **2005**, *15*, 107−112.

(201) Zhu, Y.; He, X.; Mo, Y. Origin of Outstanding Stability in the Lithium Solid Electrolyte Materials: Insights from Thermodynamic Analyses Based on First-Principles Calculations. *ACS Appl. Mater. Interfaces* **2015**, *7*, 23685−23693.

(202) Ong, S. P.; Andreussi, O.; Wu, Y.; Marzari, N.; Ceder, G. Electrochemical Windows of Room-Temperature Ionic Liquids from Molecular Dynamics and Density Functional Theory Calculations. *Chem. Mater.* **2011**, *23*, 2979−2986.

(203) Heyd, J.; Scuseria, G. E.; Ernzerhof, M. Hybrid Functionals Based on a Screened Coulomb Potential. *J. Chem. Phys.* **2003**, *118*, 8207−8215.

(204) Ong, S. P.; Mo, Y.; Richards, W. D.; Miara, L.; Lee, H. S.; Ceder, G. Phase Stability, Electrochemical Stability and Ionic Conductivity of the $Li_{10\pm1}MP_2X_{12}$ (M = Ge, Si, Sn, Al or P, and X = O, S or Se) Family of Superionic Conductors. *Energy Environ. Sci.* **2013**, *6*, 148−156.

(205) Chu, I.-H.; Nguyen, H.; Hy, S.; Lin, Y.-C.; Wang, Z.; Xu, Z.; Deng, Z.; Meng, Y. S.; Ong, S. P. Insights into the Performance Limits of the $Li_7P_3S_{11}$ Superionic Conductor: A Combined First-Principles and Experimental Study. *ACS Appl. Mater. Interfaces* **2016**, *8*, 7843−7853.

(206) Thompson, T.; Yu, S.; Williams, L.; Schmidt, R. D.; Garcia-Mendez, R.; Wolfenstine, J.; Allen, J. L.; Kioupakis, E.; Siegel, D. J.; Sakamoto, J. Electrochemical Window of the Li-Ion Solid Electrolyte $Li_7La_3Zr_2O_{12}$. *ACS Energy Lett.* **2017**, *2*, 462−468.

(207) Peljo, P.; Girault, H. H. Electrochemical Potential Window of Battery Electrolytes: the HOMO−LUMO Misconception. *Energy Environ. Sci.* **2018**, *11*, 2306−2309.

(208) Deng, Z.; Wang, Z.; Chu, I.-H.; Luo, J.; Ong, S. P. Elastic Properties of Alkali Superionic Conductor Electrolytes from First Principles Calculations. *J. Electrochem. Soc.* **2016**, *163*, A67−A74.

(209) Herbert, E. G.; Tenhaeff, W. E.; Dudney, N. J.; Pharr, G. Mechanical Characterization of LiPON Films Using Nanoindentation. *Thin Solid Films* **2011**, *520*, 413−418.

(210) Wang, S.; Bai, Q.; Nolan, A. M.; Liu, Y.; Gong, S.; Sun, Q.; Mo, Y. Lithium Chlorides and Bromides as Promising Solid-State Chemistries for Fast Ion Conductors with Good Electrochemical Stability. *Angew. Chem., Int. Ed.* **2019**, *58*, 8039−8043.

(211) Jiang, M.; Mukherjee, S.; Chen, Z. W.; Chen, L. X.; Li, M. L.; Xiao, H. Y.; Gao, C.; Singh, C. V. Materials Perspective on New Lithium Chlorides and Bromides: Insights into Thermo-Physical Properties. *Phys. Chem. Chem. Phys.* **2020**, *22*, 22758−22767.

(212) Effat, M. B.; Liu, J.; Lu, Z.; Wan, T. H.; Curcio, A.; Ciucci, F. Stability, Elastic Properties, and the Li Transport Mechanism of the Protonated and Fluorinated Antiperovskite Lithium Conductors. *ACS Appl. Mater. Interfaces* **2020**, *12*, 55011−55022.

(213) Lacivita, V.; Wang, Y.; Bo, S.-H.; Ceder, G. Ab Initio Investigation of the Stability of Electrolyte/Electrode Interfaces in All-Solid-State Na Batteries. *J. Mater. Chem. A* **2019**, *7*, 8144−8155.

(214) de Jong, M.; Chen, W.; Angsten, T.; Jain, A.; Notestine, R.; Gamst, A.; Sluiter, M.; Krishna Ande, C.; van der Zwaag, S.; Plata, J. J.; et al. Charting the Complete Elastic Properties of Inorganic Crystalline Compounds. *Sci. Data* **2015**, *2*, 150009.

(215) Ohtomo, T.; Hayashi, A.; Tatsumisago, M.; Tsuchida, Y.; Hama, S.; Kawamoto, K. All-Solid-State Lithium Secondary Batteries Using the $75Li_2S{\cdot}25P_2S_5$ Glass and the $70Li_2S{\cdot}30P_2S_5$ Glass−Ceramic as Solid Electrolytes. *J. Power Sources* **2013**, *233*, 231−235.

(216) Muramatsu, H.; Hayashi, A.; Ohtomo, T.; Hama, S.; Tatsumisago, M. Structural Change of $Li_2S-P_2S_5$ Sulfide Solid Electrolytes in the Atmosphere. *Solid State Ionics* **2011**, *182*, 116−119.

(217) Hayashi, A.; Muramatsu, H.; Ohtomo, T.; Hama, S.; Tatsumisago, M. Improvement of Chemical Stability of Li_3PS_4 Glass Electrolytes by Adding M_xO_y (M= Fe, Zn, and Bi) Nanoparticles. *J. Mater. Chem. A* **2013**, *1*, 6320−6326.

(218) Shang, S.-L.; Yu, Z.; Wang, Y.; Wang, D.; Liu, Z.-K. Origin of Outstanding Phase and Moisture Stability in a $Na_3P_{1-x}As_xS_4$ Superionic Conductor. *ACS Appl. Mater. Interfaces* **2017**, *9*, 16261−16269.

(219) Nyman, M.; Alam, T. M.; McIntyre, S. K.; Bleier, G. C.; Ingersoll, D. Alternative Approach to Increasing Li Mobility in Li-La-Nb/Ta Garnet Electrolytes. *Chem. Mater.* **2010**, *22*, 5401−5410.

(220) Wang, Y.; Lai, W. Phase Transition in Lithium Garnet Oxide Ionic Conductors $Li_7La_3Zr_2O_{12}$: The Role of Ta Substitution and H_2O/CO_2 Exposure. *J. Power Sources* **2015**, *275*, 612−620.

(221) Cheng, L.; Wu, C. H.; Jarry, A.; Chen, W.; Ye, Y.; Zhu, J.; Kostecki, R.; Persson, K.; Guo, J.; Salmeron, M. Interrelationships among Grain Size, Surface Composition, Air Stability, and Interfacial Resistance of Al-Substituted $Li_7La_3Zr_2O_{12}$ Solid Electrolytes. *ACS Appl. Mater. Interfaces* **2015**, *7*, 17649−17655.

(222) Asano, T.; Sakai, A.; Ouchi, S.; Sakaida, M.; Miyazaki, A.; Hasegawa, S. Solid Halide Electrolytes with High Lithium-Ion Conductivity for Application in 4 V Class Bulk-Type All-Solid-State Batteries. *Adv. Mater.* **2018**, *30*, 1803075.

(223) Zhu, Y.; Mo, Y. Materials Design Principles for Air-Stable Lithium/Sodium Solid Electrolytes. *Angew. Chem., Int. Ed.* **2020**, *59*, 17472−17476.

(224) Li, X.; Liang, J.; Chen, N.; Luo, J.; Adair, K. R.; Wang, C.; Banis, M. N.; Sham, T.-K.; Zhang, L.; Zhao, S.; et al. Water-Mediated Synthesis of a Superionic Halide Solid Electrolyte. *Angew. Chem., Int. Ed.* **2019**, *58*, 16427−16432.

(225) Liang, J.; Li, X.; Adair, K. R.; Sun, X. Metal Halide Superionic Conductors for All-Solid-State Batteries. *Acc. Chem. Res.* **2021**, *54*, 1023−1033.

(226) Li, W.; Liang, J.; Li, M.; Adair, K. R.; Li, X.; Hu, Y.; Xiao, Q.; Feng, R.; Li, R.; Zhang, L.; et al. Unraveling the Origin of Moisture Stability of Halide Solid-State Electrolytes by In Situ and Operando Synchrotron X-ray Analytical Techniques. *Chem. Mater.* **2020**, *32*, 7019−7027.

(227) Li, X.; Liang, J.; Adair, K. R.; Li, J.; Li, W.; Zhao, F.; Hu, Y.; Sham, T.-K.; Zhang, L.; Zhao, S.; et al. Origin of Superionic $Li_3Y_{1-x}In_xCl_6$ Halide Solid Electrolytes with High Humidity Tolerance. *Nano Lett.* **2020**, *20*, 4384−4392.

(228) Hanghofer, I.; Redhammer, G. n. J.; Rohde, S.; Hanzu, I.; Senyshyn, A.; Wilkening, H. M. R.; Rettenwander, D. Untangling the Structure and Dynamics of Lithium-Rich Anti-Perovskites Envisaged as Solid Electrolytes for Batteries. *Chem. Mater.* **2018**, *30*, 8134−8144.

(229) Reckeweg, O.; Blaschkowski, B.; Schleid, T. Li_5OCl_3 and Li_3OCl: Two Remarkably Different Lithium Oxide Chlorides. *Z. Anorg. Allg. Chem.* **2012**, *638*, 2081−2086.

(230) Frost, J. M.; Butler, K. T.; Brivio, F.; Hendon, C. H.; Van Schilfgaarde, M.; Walsh, A. Atomistic Origins of High-Performance in Hybrid Halide Perovskite Solar Cells. *Nano Lett.* **2014**, *14*, 2584−2590.

(231) Tai, Q.; You, P.; Sang, H.; Liu, Z.; Hu, C.; Chan, H. L. W.; Yan, F. Efficient and Stable Perovskite Solar Cells Prepared in Ambient Air Irrespective of the Humidity. *Nat. Commun.* **2016**, *7*, 11105.

(232) Monroe, C.; Newman, J. The Impact of Elastic Deformation on Deposition Kinetics at Lithium/Polymer Interfaces. *J. Electrochem. Soc.* **2005**, *152*, A396−A404.

(233) Porz, L.; Swamy, T.; Sheldon, B. W.; Rettenwander, D.; Frömling, T.; Thaman, H. L.; Berendts, S.; Uecker, R.; Carter, W. C.; Chiang, Y. M. Mechanism of Lithium Metal Penetration through Inorganic Solid Electrolytes. *Adv. Energy Mater.* **2017**, *7*, 1701003.

(234) Raj, R.; Wolfenstine, J. Current Limit Diagrams for Dendrite Formation in Solid-State Electrolytes for Li-Ion Batteries. *J. Power Sources* **2017**, *343*, 119−126.

(235) Ashby, M. F.; Jones, D. R.*Engineering Materials 1: An Introduction to Properties, Applications and Design*, 4th ed.; Elsevier, 2012; pp 115−129.

(236) Nonemacher, J. F.; Arinicheva, Y.; Yan, G.; Finsterbusch, M.; Krüger, M.; Malzbender, J. Fracture Toughness of Single Grains and Polycrystalline $Li_7La_3Zr_2O_{12}$ Electrolyte Material Based on a Pillar Splitting Method. *J. Eur. Ceram. Soc.* **2020**, *40*, 3057−3064.

(237) Wang, A.-N.; Nonemacher, J. F.; Yan, G.; Finsterbusch, M.; Malzbender, J.; Krüger, M. Mechanical Properties of the Solid Electrolyte Al-Substituted $Li_7La_3Zr_2O_{12}$ (LLZO) by Utilizing Micro-Pillar Indentation Splitting Test. *J. Eur. Ceram. Soc.* **2018**, *38*, 3201−3209.

(238) Yan, G.; Yu, S.; Yang, W.; Li, X.; Tempel, H.; Kungl, H.; Eichel, R.-A.; Krueger, M.; Malzbender, J. Anisotropy of the Mechanical Properties of $Li_{1.3}Al_{0.3}Ti_{1.7}(PO_4)_3$ Solid Electrolyte Material. *J. Power Sources* **2019**, *437*, 226940.

(239) Jackman, S. D.; Cutler, R. A. Effect of Microcracking on Ionic Conductivity in LATP. *J. Power Sources* **2012**, *218*, 65−72.

(240) Chandler, H.*Hardness testing*, 2nd ed.; ASM International, 1999; pp 51−60.

(241) Cho, Y.-H.; Wolfenstine, J.; Rangasamy, E.; Kim, H.; Choe, H.; Sakamoto, J. Mechanical Properties of the Solid Li-Ion Conducting Electrolyte: $Li_{0.33}La_{0.57}TiO_3$. *J. Mater. Sci.* **2012**, *47*, 5970−5977.

(242) Yu, S.; Schmidt, R. D.; Garcia-Mendez, R.; Herbert, E.; Dudney, N. J.; Wolfenstine, J. B.; Sakamoto, J.; Siegel, D. J. Elastic Properties of the Solid Electrolyte $Li_7La_3Zr_2O_{12}$ (LLZO). *Chem. Mater.* **2016**, *28*, 197−206.

(243) Yang, X.; Adair, K. R.; Gao, X.; Sun, X. Recent Advances and Perspectives on Thin Electrolytes for High-Energy-Density Solid-State Lithium Batteries. *Energy Environ. Sci.* **2021**, *14*, 643−671.

(244) Sakuda, A.; Hayashi, A.; Tatsumisago, M. Sulfide Solid Electrolyte with Favorable Mechanical Property for All-Solid-State Lithium Battery. *Sci. Rep.* **2013**, *3*, 2261.

(245) Sakuda, A.; Hayashi, A.; Takigawa, Y.; Higashi, K.; Tatsumisago, M. Evaluation of Elastic Modulus of $Li_2S-P_2S_5$ Glassy Solid Electrolyte by Ultrasonic Sound Velocity Measurement and Compression Test. *J. Ceram. Soc. Jpn.* **2013**, *121*, 946−949.

(246) McGrogan, F. P.; Swamy, T.; Bishop, S. R.; Eggleton, E.; Porz, L.; Chen, X.; Chiang, Y. M.; Van Vliet, K. J. Compliant Yet Brittle Mechanical Behavior of Li_2S-P_2S_5 Lithium-Ion-Conducting Solid Electrolyte. *Adv. Energy Mater.* **2017**, *7*, 1602011.

(247) Baranowski, L. L.; Heveran, C. M.; Ferguson, V. L.; Stoldt, C. R. Multi-Scale Mechanical Behavior of the Li_3PS_4 Solid-Phase Electrolyte. *ACS Appl. Mater. Interfaces* **2016**, *8*, 29573−29579.

(248) Born, M. On the Stability of Crystal Lattices. I. *Math. Proc. Cambridge Philos. Soc.* **1940**, *36*, 160−172.

(249) Ren, Y.; Shen, Y.; Lin, Y.; Nan, C.-W. Direct Observation of Lithium Dendrites inside Garnet-Type Lithium-Ion Solid Electrolyte. *Electrochem. Commun.* **2015**, *57*, 27−30.

(250) Cheng, E. J.; Sharafi, A.; Sakamoto, J. Intergranular Li Metal Propagation through Polycrystalline $Li_{6.25}Al_{0.25}La_3Zr_2O_{12}$ Ceramic Electrolyte. *Electrochim. Acta* **2017**, *223*, 85−91.

(251) Yu, S.; Siegel, D. J. Grain Boundary Softening: A Potential Mechanism for Lithium Metal Penetration through Stiff Solid Electrolytes. *ACS Appl. Mater. Interfaces* **2018**, *10*, 38151−38158.

(252) Wolfenstine, J.; Allen, J. L.; Sakamoto, J.; Siegel, D. J.; Choe, H. Mechanical Behavior of Li-Ion-Conducting Crystalline Oxide-Based Solid Electrolytes: A Brief Review. *Ionics* **2018**, *24*, 1271−1276.

(253) Pugh, S. F. XCII. Relations between the Elastic Moduli and the Plastic Properties of Polycrystalline Pure Metals. *Philos. Mag.* **1954**, *45*, 823−843.

(254) Yin, L.; Yuan, H.; Kong, L.; Lu, Z.; Zhao, Y. Engineering Frenkel Defects of Anti-Perovskite Solid-State Electrolytes and Their Applications in All-Solid-State Lithium-Ion Batteries. *Chem. Commun.* **2020**, *56*, 1251−1254.

(255) Dudney, N. J. Thin Film Micro-Batteries. *Electrochem. Soc. Interface* **2008**, *17*, 44−48.

(256) Moitzheim, S.; Put, B.; Vereecken, P. M. Advances in 3D Thin-Film Li-Ion Batteries. *Adv. Mater. Interfaces* **2019**, *6*, 1900805.

(257) Famprikis, T.; Canepa, P.; Dawson, J. A.; Islam, M. S.; Masquelier, C. Fundamentals of Inorganic Solid-State Electrolytes for Batteries. *Nat. Mater.* **2019**, *18*, 1278−1291.

(258) Steingart, D. A.; Viswanathan, V. Comment on "Alternative Strategy for a Safe Rechargeable Battery" by M. H. Braga, N. S. Grundish, A. J. Murchison and J. B. Goodenough, *Energy Environ. Sci.*,2017, 10, 331−336. *Energy Environ. Sci.* **2018**, *11*, 221−222.

(259) Richards, W. D.; Miara, L. J.; Wang, Y.; Kim, J. C.; Ceder, G. Interface Stability in Solid-State Batteries. *Chem. Mater.* **2016**, *28*, 266−273.

(260) Wu, M.; Xu, B.; Luo, W.; Sun, B.; Ouyang, C. Interfacial Properties and Li-Ion Dynamics between Li_3OCl Solid Electrolyte and Li Metal Anode for All Solid State Li Metal Batteries from First Principles Study. *Electrochim. Acta* **2020**, *334*, 135622.

(261) Tian, Y.; Ding, F.; Zhong, H.; Liu, C.; He, Y.-B.; Liu, J.; Liu, X.; Xu, Q. $Li_{6.75}La_3Zr_{1.75}Ta_{0.25}O_{12}$@Amorphous Li_3OCl Composite Electrolyte for Solid State Lithium-Metal Batteries. *Energy Storage Mater.* **2018**, *14*, 49−57.

(262) Feng, W.; Lai, Z.; Dong, X.; Li, P.; Wang, Y.; Xia, Y. Garnet-Based All-Ceramic Lithium Battery Enabled by $Li_{2.985}B_{0.005}OCl$ Solder. *iScience* **2020**, *23*, 101071.

(263) Jung, S.-Y.; Rajagopal, R.; Ryu, K.-S. Synthesis and Electrochemical Performance of $(100-x)Li_7P_3S_{11}$-xLi_2OHBr Composite Solid Electrolyte for All-Solid-State Lithium Batteries. *J. Energy Chem.* **2020**, *47*, 307−316.

(264) Xiao, Y.; Miara, L. J.; Wang, Y.; Ceder, G. Computational Screening of Cathode Coatings for Solid-State Batteries. *Joule* **2019**, *3*, 1252−1275.

(265) Culver, S. P.; Koerver, R.; Zeier, W. G.; Janek, J. On the Functionality of Coatings for Cathode Active Materials in Thiophosphate-Based All-Solid-State Batteries. *Adv. Energy Mater.* **2019**, *9*, 1900626.

(266) Kitaura, H.; Hayashi, A.; Tadanaga, K.; Tatsumisago, M. Improvement of Electrochemical Performance of All-Solid-State Lithium Secondary Batteries by Surface Modification of $LiMn_2O_4$ Positive Electrode. *Solid State Ionics* **2011**, *192*, 304−307.

(267) Noh, S.; Kim, J.; Eom, M.; Shin, D. Surface Modification of $LiCoO_2$ with $Li_{3x}La_{2/3-x}TiO_3$ for All-Solid-State Lithium Ion Batteries Using $Li_2S-P_2S_5$ Glass−Ceramic. *Ceram. Int.* **2013**, *39*, 8453−8458.

(268) Oh, G.; Hirayama, M.; Kwon, O.; Suzuki, K.; Kanno, R. Bulk-Type All Solid-State Batteries with 5 V Class $LiNi_{0.5}Mn_{1.5}O_4$ Cathode and $Li_{10}GeP_2S_{12}$ Solid Electrolyte. *Chem. Mater.* **2016**, *28*, 2634−2640.

(269) Sakuda, A.; Hayashi, A.; Tatsumisago, M. Electrochemical Performance of All-Solid-State Lithium Secondary Batteries Improved by the Coating of Li_2O-TiO_2 Films on $LiCoO_2$ Electrode. *J. Power Sources* **2010**, *195*, 599−603.

(270) Zhang, J.; Zhong, H.; Zheng, C.; Xia, Y.; Liang, C.; Huang, H.; Gan, Y.; Tao, X.; Zhang, W. All-Solid-State Batteries with Slurry Coated $LiNi_{0.8}Co_{0.1}Mn_{0.1}O_2$ Composite Cathode and Li_6PS_5Cl Electrolyte: Effect of Binder Content. *J. Power Sources* **2018**, *391*, 73−79.

(271) Zhang, W.; Weber, D. A.; Weigand, H.; Arlt, T.; Manke, I.; Schröder, D.; Koerver, R.; Leichtweiss, T.; Hartmann, P.; Zeier, W. G.; et al. Interfacial Processes and Influence of Composite Cathode Microstructure Controlling the Performance of All-Solid-State Lithium Batteries. *ACS Appl. Mater. Interfaces* **2017**, *9*, 17835−17845.

(272) Ito, Y.; Sakurai, Y.; Yubuchi, S.; Sakuda, A.; Hayashi, A.; Tatsumisago, M. Application of $LiCoO_2$ Particles Coated with Lithium

Ortho-Oxosalt Thin Films to Sulfide-Type All-Solid-State Lithium Batteries. *J. Electrochem. Soc.* **2015**, *162*, A1610−A1616.

(273) Sakurai, Y.; Sakuda, A.; Hayashi, A.; Tatsumisago, M. Preparation of Amorphous $Li_4SiO_4-Li_3PO_4$ Thin Films by Pulsed Laser Deposition for All-Solid-State Lithium Secondary Batteries. *Solid State Ionics* **2011**, *182*, 59−63.

(274) Yubuchi, S.; Ito, Y.; Matsuyama, T.; Hayashi, A.; Tatsumisago, M. 5 V Class $LiNi_{0.5}Mn_{1.5}O_4$ Positive Electrode Coated with Li_3PO_4 Thin Film for All-Solid-State Batteries Using Sulfide Solid Electrolyte. *Solid State Ionics* **2016**, *285*, 79−82.

(275) George, S. M. Atomic Layer Deposition: An Overview. *Chem. Rev.* **2010**, *110*, 111−131.

(276) Liu, J.; Sun, X. Elegant Design of Electrode and Electrode/Electrolyte Interface in Lithium-Ion Batteries by Atomic Layer Deposition. *Nanotechnology* **2015**, *26*, No. 024001.

(277) Meng, X.; Yang, X.-Q.; Sun, X. Emerging Applications of Atomic Layer Deposition for Lithium-Ion Battery Studies. *Adv. Mater.* **2012**, *24*, 3589−3615.

(278) Wang, X.; Yushin, G. Chemical Vapor Deposition and Atomic Layer Deposition for Advanced Lithium Ion Batteries and Supercapacitors. *Energy Environ. Sci.* **2015**, *8*, 1889−1904.

(279) Zhao, Y.; Sun, X. Molecular Layer Deposition for Energy Conversion and Storage. *ACS Energy Lett.* **2018**, *3*, 899−914.

(280) Zhao, Y.; Zheng, K.; Sun, X. Addressing Interfacial Issues in Liquid-Based and Solid-State Batteries by Atomic and Molecular Layer Deposition. *Joule* **2018**, *2*, 2583−2604.

(281) Kazyak, E.; Chen, K.-H.; Davis, A. L.; Yu, S.; Sanchez, A. J.; Lasso, J.; Bielinski, A. R.; Thompson, T.; Sakamoto, J.; Siegel, D. J.; et al. Atomic Layer Deposition and First Principles Modeling of Glassy $Li_3BO_3-Li_2CO_3$ Electrolytes for Solid-State Li Metal Batteries. *J. Mater. Chem. A* **2018**, *6*, 19425−19437.

(282) Kazyak, E.; Chen, K.-H.; Wood, K. N.; Davis, A. L.; Thompson, T.; Bielinski, A. R.; Sanchez, A. J.; Wang, X.; Wang, C.; Sakamoto, J.; et al. Atomic Layer Deposition of the Solid Electrolyte Garnet $Li_7La_3Zr_2O_{12}$. *Chem. Mater.* **2017**, *29*, 3785−3792.

(283) Kozen, A. C.; Pearse, A. J.; Lin, C.-F.; Noked, M.; Rubloff, G. W. Atomic Layer Deposition of the Solid Electrolyte LiPON. *Chem. Mater.* **2015**, *27*, 5324−5331.

(284) Liu, J.; Banis, M. N.; Li, X.; Lushington, A.; Cai, M.; Li, R.; Sham, T.-K.; Sun, X. Atomic Layer Deposition of Lithium Tantalate Solid-State Electrolytes. *J. Phys. Chem. C* **2013**, *117*, 20260−20267.

(285) Nisula, M.; Shindo, Y.; Koga, H.; Karppinen, M. Atomic Layer Deposition of Lithium Phosphorus Oxynitride. *Chem. Mater.* **2015**, *27*, 6987−6993.

(286) Wang, B.; Liu, J.; Norouzi Banis, M.; Sun, Q.; Zhao, Y.; Li, R.; Sham, T.-K.; Sun, X. Atomic Layer Deposited Lithium Silicates as Solid-State Electrolytes for All-Solid-State Batteries. *ACS Appl. Mater. Interfaces* **2017**, *9*, 31786−31793.

(287) Wang, B.; Liu, J.; Sun, Q.; Li, R.; Sham, T.-K.; Sun, X. Atomic Layer Deposition of Lithium Phosphates as Solid-State Electrolytes for All-Solid-State Microbatteries. *Nanotechnology* **2014**, *25*, 504007.

(288) Li, X.; Ren, Z.; Norouzi Banis, M.; Deng, S.; Zhao, Y.; Sun, Q.; Wang, C.; Yang, X.; Li, W.; Liang, J.; et al. Unravelling the Chemistry and Microstructure Evolution of a Cathodic Interface in Sulfide-Based All-Solid-State Li-Ion Batteries. *ACS Energy Lett.* **2019**, *4*, 2480−2488.

(289) Deng, S.; Li, X.; Ren, Z.; Li, W.; Luo, J.; Liang, J.; Liang, J.; Banis, M. N.; Li, M.; Zhao, Y.; et al. Dual-Functional Interfaces for Highly Stable Ni-Rich Layered Cathodes in Sulfide All-Solid-State Batteries. *Energy Storage Mater.* **2020**, *27*, 117−123.

(290) Adhikari, S.; Selvaraj, S.; Kim, D.-H. Progress in Powder Coating Technology Using Atomic Layer Deposition. *Adv. Mater. Interfaces* **2018**, *5*, 1800581.

(291) McCormick, J. A.; Rice, K. P.; Paul, D. F.; Weimer, A. W.; George, S. M. Analysis of Al_2O_3 Atomic Layer Deposition on ZrO_2 Nanoparticles in a Rotary Reactor. *Chem. Vap. Deposition* **2007**, *13*, 491−498.

(292) King, D. M.; Liang, X.; Weimer, A. W. Functionalization of Fine Particles Using Atomic and Molecular Layer Deposition. *Powder Technol.* **2012**, *221*, 13−25.

(293) Muñoz-Rojas, D.; MacManus-Driscoll, J. Spatial Atmospheric Atomic Layer Deposition: A New Laboratory and Industrial Tool for Low-Cost Photovoltaics. *Mater. Horiz.* **2014**, *1*, 314−320.

(294) Musselman, K. P.; Uzoma, C. F.; Miller, M. S. Nanomanufacturing: High-Throughput, Cost-Effective Deposition of Atomic Scale Thin Films via Atmospheric Pressure Spatial Atomic Layer Deposition. *Chem. Mater.* **2016**, *28*, 8443−8452.

(295) Muñoz-Rojas, D.; Maindron, T.; Esteve, A.; Piallat, F.; Kools, J. C. S.; Decams, J. M. Speeding Up the Unique Assets of Atomic Layer Deposition. *Mater. Today Chem.* **2019**, *12*, 96−120.

(296) Gao, Y.; Nolan, A. M.; Du, P.; Wu, Y.; Yang, C.; Chen, Q.; Mo, Y.; Bo, S.-H. Classical and Emerging Characterization Techniques for Investigation of Ion Transport Mechanisms in Crystalline Fast Ionic Conductors. *Chem. Rev.* **2020**, *120*, 5954−6008.

(297) Xiang, Y.; Li, X.; Cheng, Y.; Sun, X.; Yang, Y. Advanced Characterization Techniques for Solid State Lithium Battery Research. *Mater. Today* **2020**, *36*, 139−157.

(298) Lin, F.; Liu, Y.; Yu, X.; Cheng, L.; Singer, A.; Shpyrko, O. G.; Xin, H. L.; Tamura, N.; Tian, C.; Weng, T.-C.; et al. Synchrotron X-ray Analytical Techniques for Studying Materials Electrochemistry in Rechargeable Batteries. *Chem. Rev.* **2017**, *117*, 13123−13186.

(299) Li, W.; Li, M.; Hu, Y.; Lu, J.; Lushington, A.; Li, R.; Wu, T.; Sham, T.-K.; Sun, X. Synchrotron-Based X-ray Absorption Fine Structures, X-ray Diffraction, and X-ray Microscopy Techniques Applied in the Study of Lithium Secondary Batteries. *Small Methods* **2018**, *2*, 1700341.

(300) Wang, L.; Wang, J.; Zuo, P. Probing Battery Electrochemistry with In Operando Synchrotron X-Ray Imaging Techniques. *Small Methods* **2018**, *2*, 1700293.

(301) Gu, Q.; Kimpton, J. A.; Brand, H. E. A.; Wang, Z.; Chou, S. Solving Key Challenges in Battery Research Using In Situ Synchrotron and Neutron Techniques. *Adv. Energy Mater.* **2017**, *7*, 1602831.

(302) Gong, Z.; Yang, Y. The Application of Synchrotron X-Ray Techniques to the Study of Rechargeable Batteries. *J. Energy Chem.* **2018**, *27*, 1566−1583.

(303) Koedtruad, A.; Amano Patino, M.; Chuang, Y.-C.; Chen, W.-t.; Kan, D.; Shimakawa, Y. Ruddlesden−Popper Phases of Lithium-Hydroxide-Halide Antiperovskites: Two Dimensional Li-Ion Conductors. *RSC Adv.* **2020**, *10*, 41816−41820.

(304) Wang, F.; Evans, H. A.; Kim, K.; Yin, L.; Li, Y.; Tsai, P.-C.; Liu, J.; Lapidus, S. H.; Brown, C. M.; Siegel, D. J.; et al. Dynamics of Hydroxyl Anions Promotes Lithium Ion Conduction in Antiperovskite Li_2OHCl. *Chem. Mater.* **2020**, *32*, 8481−8491.

(305) Koedtruad, A.; Patino, M. A.; Ichikawa, N.; Kan, D.; Shimakawa, Y. Crystal Structures and Ionic Conductivity in Li_2OHX (X = Cl, Br) Antiperovskites. *J. Solid State Chem.* **2020**, *286*, 121263.

(306) Wang, Y.; Wen, T.; Park, C.; Kenney-Benson, C.; Pravica, M.; Yang, W.; Zhao, Y. Robust High Pressure Stability and Negative Thermal Expansion in Sodium-Rich Antiperovskites Na_3OBr and Na_4OI_2. *J. Appl. Phys.* **2016**, *119*, No. 025901.

(307) Liu, Y.; Sun, Q.; Zhao, Y.; Wang, B.; Kaghazchi, P.; Adair, K. R.; Li, R.; Zhang, C.; Liu, J.; Kuo, L.-Y.; et al. Stabilizing the Interface of NASICON Solid Electrolyte against Li Metal with Atomic Layer Deposition. *ACS Appl. Mater. Interfaces* **2018**, *10*, 31240−31248.

(308) Liu, X.; Wang, D.; Liu, G.; Srinivasan, V.; Liu, Z.; Hussain, Z.; Yang, W. Distinct Charge Dynamics in Battery Electrodes Revealed by In Situ and Operando Soft X-Ray Spectroscopy. *Nat. Commun.* **2013**, *4*, 2568.

(309) Liang, J.; Li, X.; Wang, S.; Adair, K. R.; Li, W.; Zhao, Y.; Wang, C.; Hu, Y.; Zhang, L.; Zhao, S.; et al. Site-Occupation-Tuned Superionic Li_xScCl_{3+x} Halide Solid Electrolytes for All-Solid-State Batteries. *J. Am. Chem. Soc.* **2020**, *142*, 7012−7022.

(310) Ren, Y.; Zuo, X. Synchrotron X-Ray and Neutron Diffraction, Total Scattering, and Small-Angle Scattering Techniques for Rechargeable Battery Research. *Small Methods* **2018**, *2*, 1800064.

(311) Balagurov, A. M.; Bobrikov, I. A.; Samoylova, N. Y.; Drozhzhin, O. A.; Antipov, E. V. Neutron Scattering for Analysis of Processes in Lithium-Ion Batteries. *Russ. Chem. Rev.* **2014**, *83*, 1120−1134.

(312) Sears, V. F. Neutron Scattering Lengths and Cross Sections. *Neutron News* **1992**, *3*, 26−37.

(313) Lang, P. F.; Smith, B. C. Ionic Radii for Group 1 and Group 2 Halide, Hydride, Fluoride, Oxide, Sulfide, Selenide and Telluride Crystals. *Dalton Trans.* **2010**, *39*, 7786−7791.

(314) Sakata, M.; Uno, T.; Takata, M.; Howard, C. J. Maximum-Entropy-Method Analysis of Neutron Diffraction Data. *J. Appl. Crystallogr.* **1993**, *26*, 159−165.

(315) Izumi, F.; Kumazawa, S.; Ikeda, T.; Hu, W. Z.; Yamamoto, A.; Oikawa, K. MEM-Based Structure-Refinement System REMEDY and its Applications. *Mater. Sci. Forum* **2001**, *378−381*, 59−64.

(316) Yashima, M.; Itoh, M.; Inaguma, Y.; Morii, Y. Crystal Structure and Diffusion Path in the Fast Lithium-Ion Conductor $La_{0.62}Li_{0.16}TiO_3$. *J. Am. Chem. Soc.* **2005**, *127*, 3491−3495.

(317) Han, J.; Zhu, J.; Li, Y.; Yu, X.; Wang, S.; Wu, G.; Xie, H.; Vogel, S. C.; Izumi, F.; Momma, K.; et al. Experimental Visualization of Lithium Conduction Pathways in Garnet-Type $Li_7La_3Zr_2O_{12}$. *Chem. Commun.* **2012**, *48*, 9840−9842.

(318) Nishimura, S.-i.; Kobayashi, G.; Ohoyama, K.; Kanno, R.; Yashima, M.; Yamada, A. Experimental Visualization of Lithium Diffusion in Li_xFePO_4. *Nat. Mater.* **2008**, *7*, 707−711.

(319) Barde, F.; Palacin, M.; Chabre, Y.; Isnard, O.; Tarascon, J.-M. In Situ Neutron Powder Diffraction of a Nickel Hydroxide Electrode. *Chem. Mater.* **2004**, *16*, 3936−3948.

(320) Rosciano, F.; Holzapfel, M.; Scheifele, W.; Novák, P. A Novel Electrochemical Cell for In Situ Neutron Diffraction Studies of Electrode Materials for Lithium-Ion Batteries. *J. Appl. Crystallogr.* **2008**, *41*, 690−694.

(321) Sharma, N.; Du, G.; Studer, A. J.; Guo, Z.; Peterson, V. K. In-Situ Neutron Diffraction Study of the MoS_2 Anode Using a Custom-Built Li-Ion Battery. *Solid State Ionics* **2011**, *199−200*, 37−43.

(322) Bianchini, M.; Leriche, J.-B.; Laborier, J.-L.; Gendrin, L.; Suard, E.; Croguennec, L.; Masquelier, C. A New Null Matrix Electrochemical Cell for Rietveld Refinements of In-Situ or Operando Neutron Powder Diffraction Data. *J. Electrochem. Soc.* **2013**, *160*, A2176−A2183.

(323) Biendicho, J. J.; Roberts, M.; Offer, C.; Noréus, D.; Widenkvist, E.; Smith, R. I.; Svensson, G.; Edström, K.; Norberg, S. T.; Eriksson, S. G.; et al. New In-Situ Neutron Diffraction Cell for Electrode Materials. *J. Power Sources* **2014**, *248*, 900−904.

(324) Taminato, S.; Yonemura, M.; Shiotani, S.; Kamiyama, T.; Torii, S.; Nagao, M.; Ishikawa, Y.; Mori, K.; Fukunaga, T.; Onodera, Y.; et al. Real-Time Observations of Lithium Battery Reactions—Operando Neutron Diffraction Analysis during Practical Operation. *Sci. Rep.* **2016**, *6*, 28843.

(325) Wang, X.-L.; An, K.; Cai, L.; Feng, Z.; Nagler, S. E.; Daniel, C.; Rhodes, K. J.; Stoica, A. D.; Skorpenske, H. D.; Liang, C.; et al. Visualizing the Chemistry and Structure Dynamics in Lithium-Ion Batteries by In-Situ Neutron Diffraction. *Sci. Rep.* **2012**, *2*, 747.

(326) Sharma, N.; Guo, X.; Du, G.; Guo, Z.; Wang, J.; Wang, Z.; Peterson, V. K. Direct Evidence of Concurrent Solid-Solution and Two-Phase Reactions and the Nonequilibrium Structural Evolution of $LiFePO_4$. *J. Am. Chem. Soc.* **2012**, *134*, 7867−7873.